BioMed Research International

CT Perfusion: Technical Developments and Current and Future Applications

Guest Editors: Maria Antonietta Mazzei, Lorenzo Preda, Alessandro Cianfoni, and Luca Volterrani

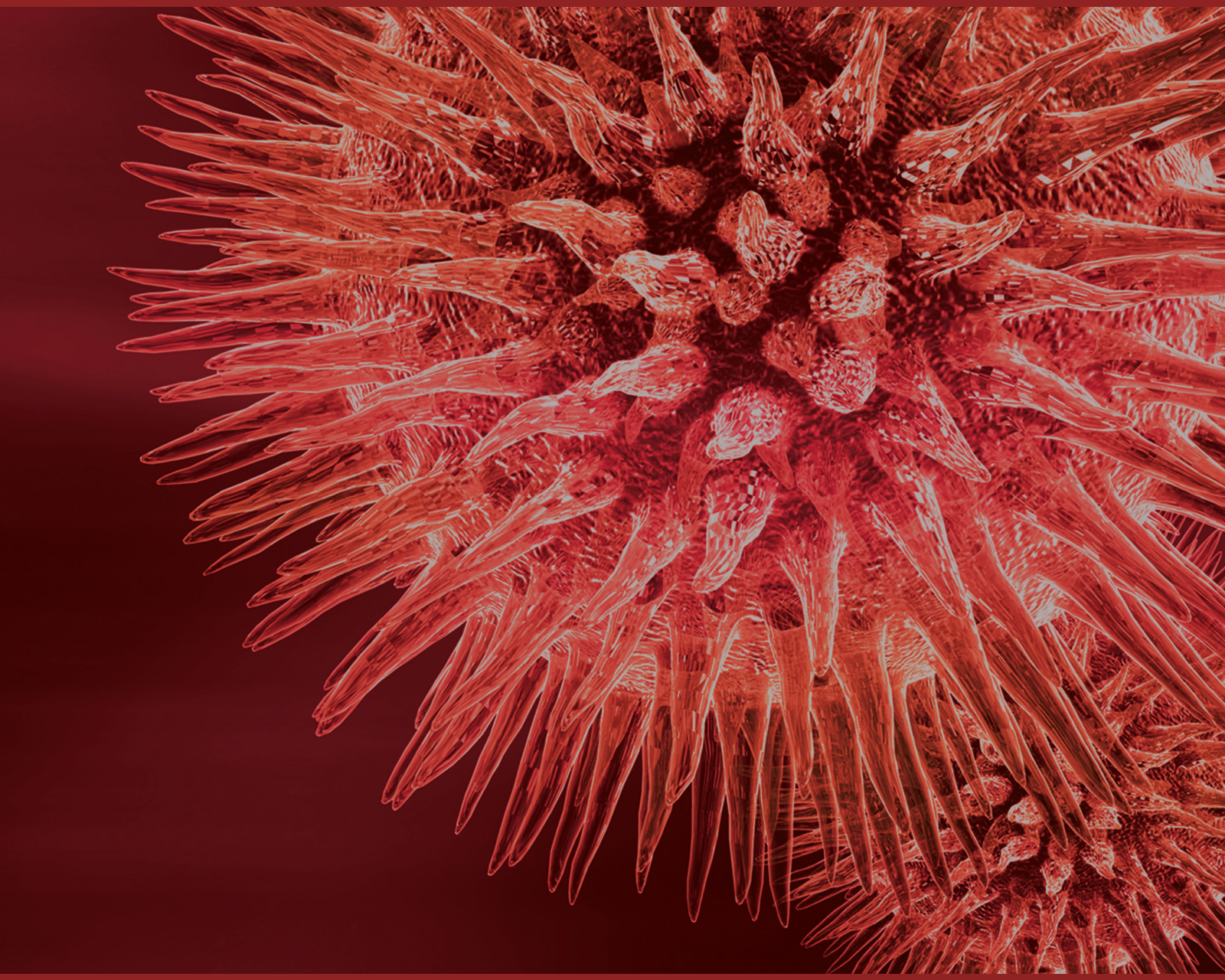

CT Perfusion: Technical Developments and Current and Future Applications

BioMed Research International

CT Perfusion: Technical Developments and Current and Future Applications

Guest Editors: Maria Antonietta Mazzei, Lorenzo Preda, Alessandro Cianfoni, and Luca Volterrani

Contents

Hindawi Publishing Corporation
BioMed Research International
Volume 2015, Article ID 397521, 2 pages
http://dx.doi.org/10.1155/2015/397521

Editorial

CT Perfusion: Technical Developments and Current and Future Applications

Maria Antonietta Mazzei,[1] Lorenzo Preda,[2] Alessandro Cianfoni,[3,4] and Luca Volterrani[1]

[1]*Department of Medical, Surgical and Neuro Sciences, Diagnostic Imaging, University of Siena, Viale Bracci 10, 53100 Siena, Italy*
[2]*Division of Radiology, European Institute of Oncology, University of Milan, Via Ripamonti 435, 20141 Milan, Italy*
[3]*Department of Neuroradiology, Medical University of South Carolina, Charleston, SC 29425, USA*
[4]*Department of Neuroradiology, Neurocenter of Italian Switzerland, 6903 Lugano, Switzerland*

Correspondence should be addressed to Maria Antonietta Mazzei; mariaantonietta.mazzei@unisi.it

Received 14 December 2014; Accepted 14 December 2014

The official history of Computed Tomography perfusion (CTp) began in 1979 when Heinz and his colleagues published their paper [1].

From that date, a limited number of experiences have been carried out to achieve the technique that is now becoming more familiar thanks to the availability of commercial CTp software platforms that are integrated into today's clinical reporting workstations, allowing a rapid analysis and processing of dynamic data sets. From a technical point of view, CTp requires a rapid intravenous injection of an iodinated contrast medium (CM) bolus and sequential imaging to simultaneously monitor changes in the CM concentration as a function of time, both in the tissue of interest and in the vessel that is used as an input function. CTp is thus able to determine, through mathematical models and dedicated software, the perfusion parameters of a given tissue, such as the blood flow (BF), the blood volume (BV), the mean transit time (MTT), and the capillary permeability surface (PS). In particular, PS is considered a functional CT surrogate marker of neoplastic angiogenesis, focusing on the interest of the use of CTp in oncologic imaging [2]. Today, CTp could routinely offer functional imaging information, as an adjunct to a conventional or morphologic CT examination. In particular, it is a widely applied technique in the evaluation of acute ischemic stroke patients and to investigate other brain diseases, including tumours. It can also be used as an aid to distinguish benign and malignant lesions in body imaging and above all to monitor the treatment response in oncologic patients. This has subsequently lead to some authors affirming that CTp is a more sensitive image biomarker than RECIST and tumour density for monitoring early antiangiogenic treatment effects as well as in predicting prognosis and progression-free survival at the end of treatment. However, despite these possibilities, CTp is still considered a niche technique because of some issues. Firstly, the lack of awareness between radiologists, in fact despite the diffusion of commercial CTp software platforms, CTp has not been routinely utilised in clinical practice yet. It also suffers from some limitations due to the high radiation dose delivered to patients, the need for CM injection, and the lack of reproducibility of CTp data obtained from different software packages used and also between the different upgrades of the same commercial software [3]. The dose exposure to the patient is strictly related to the acquisition time required for the dynamic scanning of the volume being analysed. However, a lot of possibilities for reducing the dose exposure to the patient are available today, for example, the axial acquisition opposed to the cine acquisition technique, the combination between CTp and iterative reconstruction techniques, and the possibility to obtain reproducible CTp measurements using a short time acquisition protocol with the CTp deconvolution method. Therefore, if the dose exposure question can be overtaken today, the main problem remains the lack of a standardised

method for CTp analysis. Several algorithms have been developed, applying different kinetic models. The algorithms of these software packages were categorised into two groups on the basis of the applied model and the effect of the delay of the bolus tracer: delay-sensitive and delay-insensitive. In particular, the two main models used by different software packages for CTp analysis derive the Time-Density Curves (TDC) and consequently the CTp parameters of a given tissue by using a graphic analysis of a two-compartment model, the so-called Patlak plot, or a deconvolution technique based on the time invariant linear compartmental model, that uses arterial and tissue TDCs to calculate the residual impulse response function (IRF), a theoretic curve obtained assuming that the CM is not diffusible. Recent studies showed that intervendor differences constituted the primary cause for the variability in CTp analysis; moreover, there is also a lack of reproducibility of CTp values obtained from different upgrades of the same commercial software. In fact, even if upgrades of the same commercial software frequently improve reliability and performance, such upgrades may significantly alter the derived CTp parameter values with a potential clinical impact, in particular, in oncologic imaging. Because of this variability, CTp summary maps should be interpreted with care and future studies on this topic should be focused on the standardisation of CTp analysis algorithms in order to obtain reproducible and comparable results across different institutions and different software packages. In this special issue, we collected articles focusing on some interesting topics in CTp imaging. In particular, new aspects of investigation of CTp in oncologic imaging are discussed in three articles: "Perfusion in the Tissue Surrounding Pancreatic Cancer and the Patient's Prognosis," "CT Perfusion in the Characterisation of Renal Lesions: An Added Value to Multiphasic CT," and "Role of CT Perfusion in Monitoring and Prediction of Response to Therapy of Head and Neck Squamous Cell Carcinoma," whereas technical aspects regarding the possibilities of reducing the dose exposure to the patient and protocol optimisation are discussed in the "Reduced Time CT Perfusion Acquisitions Are Sufficient to Measure the Permeability Surface Area Product with a Deconvolution Method" and "Total Bolus Extraction Method Improves Arterial Image Quality in Dynamic CTAs Derived from Whole-Brain CTP Data," respectively. The contributions of this special issue could stimulate the spread of CTp imaging in daily practice, pinpoint new or extended applications of this technique, and share some strategies to optimise CTp protocol also in reducing the radiation dose to the patient.

Maria Antonietta Mazzei
Lorenzo Preda
Alessandro Cianfoni
Luca Volterrani

References

[1] E. R. Heinz, P. Dubois, D. Osborne, B. Drayer, and W. Barrett, "Dynamic computed tomography study of the brain," *Journal of Computer Assisted Tomography*, vol. 3, no. 5, pp. 641–649, 1979.

[2] R. García-Figueiras, V. J. Goh, A. R. Padhani et al., "CT perfusion in oncologic imaging: a useful tool?" *American Journal of Roentgenology*, vol. 200, no. 1, pp. 8–19, 2013.

[3] M. A. Mazzei, N. C. Squitieri, E. Sani et al., "Differences in perfusion CT parameter values with commercial software upgrades: a preliminary report about algorithm consistency and stability," *Acta Radiologica*, vol. 54, no. 7, pp. 805–811, 2013.

Hindawi Publishing Corporation
BioMed Research International
Volume 2015, Article ID 297696, 14 pages
http://dx.doi.org/10.1155/2015/297696

Review Article

Functional Relevance of Coronary Artery Disease by Cardiac Magnetic Resonance and Cardiac Computed Tomography: Myocardial Perfusion and Fractional Flow Reserve

Gianluca Pontone,[1] Daniele Andreini,[1,2] Andrea Baggiano,[1] Erika Bertella,[1] Saima Mushtaq,[1] Edoardo Conte,[1] Virginia Beltrama,[1] Andrea Igoren Guaricci,[3] and Mauro Pepi[1]

[1]*Centro Cardiologico Monzino, IRCCS, Via C. Parea 4, 20138 Milan, Italy*
[2]*Department of Cardiovascular Sciences and Community Health, University of Milan, Italy*
[3]*Ospedali Riuniti, Department of Cardiology, University of Foggia, Italy*

Correspondence should be addressed to Gianluca Pontone; gianluca.pontone@ccfm.it

Received 23 June 2014; Accepted 31 August 2014

Academic Editor: Maria Antonietta Mazzei

Coronary artery disease (CAD) is one of the leading causes of morbidity and mortality and it is responsible for an increasing resource burden. The identification of patients at high risk for adverse events is crucial to select those who will receive the greatest benefit from revascularization. To this aim, several non-invasive functional imaging modalities are usually used as gatekeeper to invasive coronary angiography, but the diagnostic yield of elective invasive coronary angiography remains unfortunately low. Stress myocardial perfusion imaging by cardiac magnetic resonance (stress-CMR) has emerged as an accurate technique for diagnosis and prognostic stratification of the patients with known or suspected CAD thanks to high spatial and temporal resolution, absence of ionizing radiation, and the multiparametric value including the assessment of cardiac anatomy, function, and viability. On the other side, cardiac computed tomography (CCT) has emerged as unique technique providing coronary arteries anatomy and more recently, due to the introduction of stress-CCT and noninvasive fractional flow reserve (FFR-CT), functional relevance of CAD in a single shot scan. The current review evaluates the technical aspects and clinical experience of stress-CMR and CCT in the evaluation of functional relevance of CAD discussing the strength and weakness of each approach.

1. Introduction

Coronary artery disease (CAD) is a major cause of mortality and morbidity in the western countries and its increasing prevalence is responsible for advances in percutaneous and surgical revascularization [1]. The related cost of revascularization procedures has resulted in a great interest of healthcare community regarding appropriateness of this technique and how to select the patients with known or suspected CAD who will receive the greatest benefits from these invasive treatments. Indeed, inappropriate revascularization may generate costs to the healthcare system while appropriate revascularization improves patients' outcome [1]. For this reason, guidelines recommend different diagnostic strategy based on the pretest likelihood of CAD and suggest a conservative observational approach in the case of patients with a very low risk, non-invasive stress testing to detect ischemic burden as gatekeeper to invasive coronary angiography (ICA) in intermediate risk patients, and direct referral for ICA in high-risk patients for CAD. The intermediate risk patients are the most representative population referred to clinical evaluation for suspected or known CAD and the use of imaging tests in this setting has doubled from 2000 to 2006 with $ 14.1 billion in Medicare budget in 2006. Several non-invasive imaging modalities such as exercise electrocardiogram (ECG), stress echocardiography, or nuclear stress tests are suggested as

gatekeeper to ICA [1]. However, the diagnostic yield of elective ICA remains low. Patel et al. [2] have showed in a US national register that the prevalence of obstructive coronary artery stenoses in 398978 consecutive patients referred to ICA for suspected CAD was only 38%. The low diagnostic yield of elective ICA occurs despite the fact that 84% of study population undergoing ICA had performed a previous non-invasive diagnostic test. It has also emerged that although non-invasive test was independently related to the presence of obstructive CAD, the additional value of a positive non-invasive stress test to predict obstructive CAD beyond the Framingham risk category and symptom characteristics was limited [2]. However, the evaluation of functional relevance of CAD with noninvasive tests as gatekeeper to ICA remains mandatory. Indeed, the Clinical Outcome Utilizing Revascularization and Aggressive Drug Evaluation trial (COURAGE) [3] and the COURAGE trial nuclear substudy [4] have demonstrated that the event-free survival with coronary revascularization was greater than optimal medical therapy in patients with ≥10% ischemic myocardium at baseline and with a reduction of ischemic myocardium ≥5% after treatment. Stress myocardial perfusion imaging by cardiac magnetic resonance (stress-CMR) has emerged during the past decade as accurate technique for diagnosing and prognostic stratification of the patients with known or suspected CAD thanks to high spatial and temporal resolution, absence of ionizing radiation, and the multiparametric value including the assessment of cardiac anatomy, function, and viability [5]. On the other side, cardiac computed tomography (CCT) has emerged as unique non-invasive technique providing coronary arteries anatomy and more recently as competitive technique able to evaluate the functional relevance of coronary artery stenoses in a single shot scan by using both stress-CCT and fractional flow reserve (FFR-CT) [6]. The current review evaluates the technical aspects and clinical experience of stress-CMR and CCT in the assessment of functional relevance of CAD discussing the strength and weakness of each approach.

2. How to Evaluate Functional Relevance of CAD

There are two different approaches to evaluate functional relevance of CAD: the assessment of myocardial perfusion under stress and the measurement of FFR. The rationale for stress myocardial perfusion imaging is based on the concept of coronary flow reserve [7] that is briefly described in Figure 1. The cardiac metabolism is mainly aerobic and it is sustained by a coronary blood flow of about 0.8–1 mL/gr/min that occurs in diastolic phase and it is driven by gradient between the diastolic blood pressure and the end-diastolic left ventricle pressure [7]. At rest condition, the autoregulation mechanism by adjusting coronary microvascular resistance maintains coronary blood flow constant in a wide range of coronary perfusion gradient pressure and the heart utilizes the maximum oxygen extraction corresponding to 80% of the oxygen available in the blood pool. Therefore, in the conditions in which the oxygen demand is increased, a maximal coronary artery vasodilatation occurs to reach a direct relationship between coronary artery gradient pressure and coronary artery blood flow. The coronary artery flow reserve (CFR) is the ratio between the coronary artery flow at maximum vasodilatation and the coronary blood flow at rest. Usually, in the absence of epicardial coronary artery disease, CRF increases by factor 5 or more while in presence of 50% epicardial coronary artery lumen reduction CRF decreases up to be abnormal at rest in the presence of high degree of stenoses (>85%) [8, 9]. The maximal vasodilatation can be brought with pharmacologic stress by using three different drug stressors such as adenosine, dipyridamole, or regadenoson that are briefly described in Table 1. Both adenosine and dipyridamole are direct and indirect not-selective adenosine receptor agonists, respectively, providing up to fourfold increase of coronary flow. In the presence of epicardial coronary stenoses both drug stressors act on normal vessels but have no effects on stenotic vessels producing ischemia based on "steal phenomenon" [10]. More recently, regadenoson, a selective A_{2A} receptor agonist, has been approved for pharmacological stress test with the great advantage of having minor side effects as compared to adenosine and dipyridamole [11]. Of note, the myocardial perfusion can be evaluated by dobutamine as well. However, dobutamine induces ischemia by improving heart rate rather than "steal phenomen". Therefore, the perfusion defect detected by dobutamine is an indirect effect of mismatch between the mycoradial perfusion and myocardial oxygen consumption due to increase of heart rate. The myocardial ischemia induced by "steal phenomenon" is the base of perfusion and wall motion abnormalities detection during stress-CMR and stress-CCT. Unfortunately, the CFR is an expression of a pressure gradient between epicardial coronary artery and microcirculation and therefore it is reduced in case of collaterals or microcirculation disease even in the absence of epicardial stenosis [12]. For this reason, these stress perfusion tests are not able to distinguish between the two entities. To this regard, the invasive FFR has been introduced

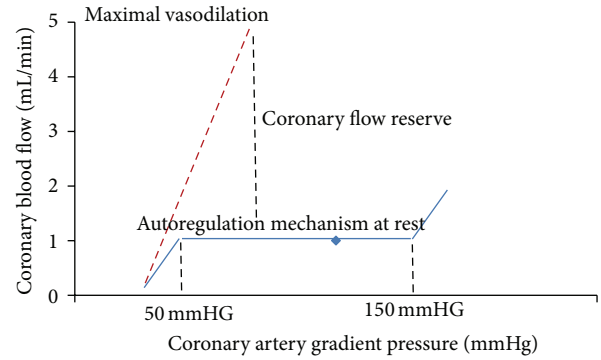

Figure 1: Coronary flow reserve. Relationship between the coronary artery gradient pressure (difference between the epicardial coronary artery and microcirculation pressure) and coronary blood flow at rest condition (blue line) and at maximal vasodilatation (red line). The coronary flow reserve (CRF) is defined as the ratio between the coronary blood flow at maximum vasodilatation and the coronary blood flow at rest condition.

Table 1: Summary of the most common drug stressors used for the evaluation of myocardial perfusion.

Drug stressors	Action	Half-life	Side effects	Cost
Adenosine	Coronary vasodilatation induced by not-selective A1 adenosine-receptors stimulation (increasing cellular cAMP levels)	10 seconds	Facial flushing Diaphoresis nausea asthma Bradyarrhythmias	↑↑↑
Dipyridamole	Coronary vasodilatation induced by inhibition of the phosphodiesterase enzymes that normally break down cAMP (increasing cellular cAMP levels)	25 minutes	Facial flushing Diaphoresis nausea asthma Bradyarrhythmias	↑
Regadenoson	Coronary vasodilatation induced by selective A2A adenosine-receptors stimulation	2-3 minutes	Headache, dizziness, nausea, stomach discomfort, decreased sense of taste, mild chest discomfort, or warmth, redness, or tingly feeling under your skin	↑↑

to overcome these limitations. FFR is performed by dedicated solid-state sensor mounted on a floppy-tipped guidewire. It measures the intracoronary pressure before and after a specific coronary lesion in the presence of hyperaemic stimuli by adenosine reaching a direct relationship between pressure and flow. Therefore, FFR can be expressed as the ratio of maximum blood flow after coronary artery stenoses to maximum blood flow. Coronary artery lesions with FFR $\leq$ 0.80 have been proved to receive benefits from revascularization while, in a setting of a stenosis with a FFR > 0.80, the patient can be safely deferred to optimal medical treatment [13, 14]. More important, unlike the ischemia stressors induced, FFR is not influenced by systemic hemodynamic [15, 16], it takes into account the contribution of collaterals [17, 18], it specifically relates to the severity of the stenoses and to the mass of tissue to be perfused [19], and it reaches a per-lesion accuracy rather than per-myocardial territory with a very high spatial resolution [12]. The main principles of FFR are described in Figure 2. In conclusion, it is of paramount importance to determine if a coronary stenosis is associated with reversible ischemia for decision making of treatment, and myocardial perfusion under stress or FFR are two sides of same coin.

2.1. Functional Relevance of CAD by CMR

2.1.1. Principles of Stress Cardiac Magnetic Resonance Protocol. Despite the fact that the technical aspects of stress-CMR are beyond the aim of this paper, a summary of the most common protocols used is described below and illustrated in Figure 3 according to the recommendations of the Society of Cardiovascular Magnetic Resonance [20]. After steady-state free precession cine acquisitions have been acquired at rest during held expiration in multiple short and long axes, coronary vasodilatation can be induced with drug infusion and then first-pass perfusion technique using saturation-prepared T1-weighted fast gradient-echo sequence with simultaneous gadolinium contrast agent injection. In case of use of dipyridamole as stressor, due to the longer half-life as compared to adenosine, left ventricle kinesis under stress can be evaluated by further steady-state free precession cine acquisitions with the same geometry used at rest. Theophylline is intravenously injected to null the effect of dipyridamole at the end of stress test. Ten minutes after contrast injection, breath-hold contrast-enhanced segmented T1-weighted inversion-recovery gradient-echo sequences are acquired with the same prescriptions for cine images to detect late gadolinium enhancement (LGE). At the end of exam, a further first-pass perfusion technique is performed to provide myocardial perfusion at rest.

2.1.2. Principles of Evaluation of Reversible Ischemia. The clinically predominant mode of reading and interpreting myocardial perfusion studies is based on visual approach. Beyond the usual parameters estimated by CMR such as end diastolic and end systolic left and right ventricle volume, left ventricle mass, and left and right ejection fraction, a reversible perfusion defect is defined as persistent delay of enhancement during first pass of contrast agent for >3 heartbeats after maximum signal intensity in the cavity of the left ventricle that does not correspond to perfusion defect at rest. Similarly, each myocardial segment is classified as normal, hypokinetic, akinetic, or dyskinetic. Accordingly, each stress-CMR can be classifiedas normal for reversible ischemia (no evidence of ischemia due to the absence of stress perfusion defect in at least 1 myocardial segment free from LGE), positive for reversible myocardial perfusion defect alone (evidence of stress perfusion defect in at least 1 myocardial segment without corresponding LGE), or positive for both perfusion and wall motion abnormalities (WMA) (evidence of stress perfusion defect in at least 1 myocardial segment without corresponding LGE plus stress WMA as compared to rest condition). A quantitative analysis of the myocardial perfusion is feasible as well. The epicardial and endocardial borders of the left ventricle wall have to be detected for each image frame of perfusion study to derive parameters value of time course of contrast agent as showed in Figure 4. For each curve, a time to arrival of contrast agent, a time to peak of signal intensity, or the slope of curve can be calculated and compared between stress and rest. Despite the fact that the quantitative approach has been proved more robust to discriminate between 1-vessel and 3-vessel disease, it is extremely time consuming and therefore not generally used in clinical practice [21]. Several artifacts can occur during stress-CMR. Dark subendocardial rim artifacts are the most common and may be confused with myocardial perfusion defects. They typically appear as dark lines at the border of

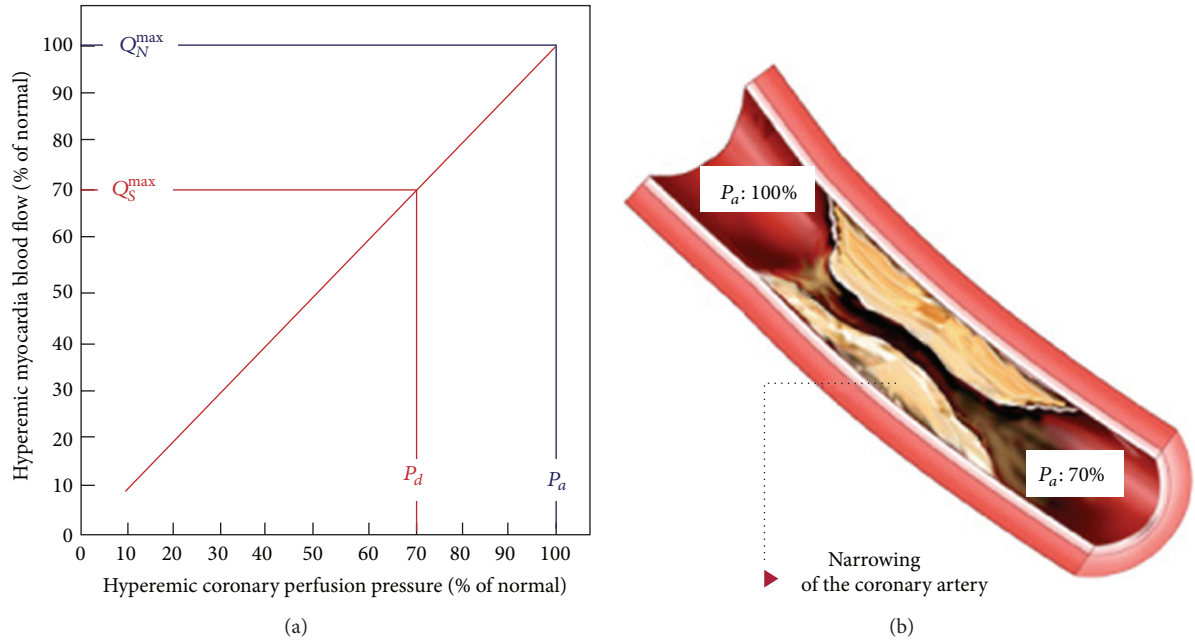

Figure 2: Fractional flow reserve. Left panel shows the relationship between coronary perfusion pressure and myocardial blood flow at maximum hyperemic stimulation. In the absence of coronary artery stenoses, the myocardial blood flow determinated by driving pressure at maximum vasodilatation is 100% (blue line). In case of coronary artery stenoses (right panel) determinating a hyperemic pressure gradient of 30 mmhg (red line) the driving pressure after the stenosis and the consequential myocardial blood flow will be reduced up to 70% corresponding to a FFR value of 0.7. Modified by Pijls et al. [18].

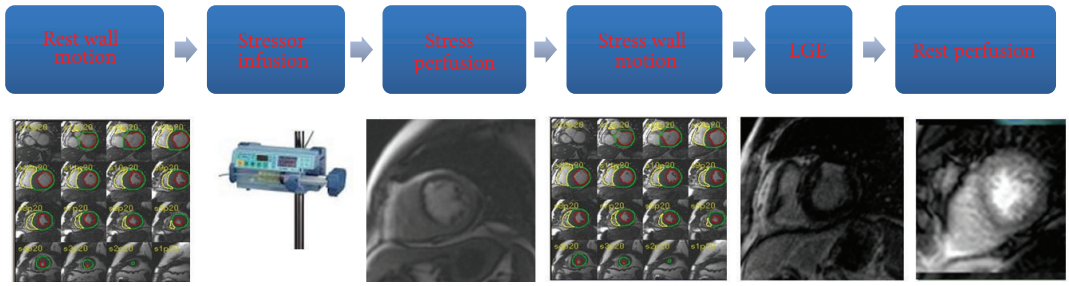

Figure 3: Stress cardiac magnetic resonance protocol. A typical stress cardiac magnetic resonance protocol is described here. For the description see throughout the paper. LGE: late gadolinium enhancement.

blood flow and myocardium. Factors that may contribute to the production of dark rim artifacts include partial-volume averaging, gadolinium-induced magnetic susceptibility, myocardial motion, and undersampling from low spatial resolution, either alone or in combination. Regardless of their cause, the artifacts are mitigated by using parallel acquisition schemes, by reaching greater SNR with 3.0-T magnets, or by using lower concentrations of gadolinium leading to less severe magnetic susceptibility effects. Aliasing artifacts are common as well in first-pass perfusion imaging especially when parallel imaging techniques are used and they could be mitigated by selection of a sufficiently large field of view.

2.1.3. Stress-CMR for Diagnosis of CAD. A high number of single and multicenter studies have proved the excellent sensitivity and specificity of stress-CMR for diagnosis of CAD [22–25] and are briefly described in Table 2. In a meta-analysis by Nandalur et al. [22] involving 1183 patients, perfusion CMR had a sensitivity of 91% and a specificity of 81% and a stress-induced WMA demonstrated a sensitivity of 83% and specificity of 86% for diagnosis of CAD in a per-patient analysis, respectively. Moreover, several papers have compared stress-CMR versus single photon emission computed tomography (SPECT) in terms of diagnostic accuracy. Schwitter et al. [23] compared stress-CMR versus SPECT in 234 patients by using ICA as reference showing a better

Table 2: Characteristics of a selected list of studies of the diagnostic performance of stress myocardial perfusion cardiac magnetic resonance.

Author	Reference	N	Sensitivity	Specificity
Nandalur et al. [22]	Stress-CMR versus QCA (meta-analysis)	1183	91%	81%
Schwitter et al. [23]	Stress-CMR and SPECT versus QCA	234	67%	85%
Greenwood et al. [24]	Stress-CMR and SPECT versus QCA	752	86%	83%
Schwitter et al. [25]	Stress-CMR and SPECT versus QCA	533	75%	59%
Greenwood et al. [26]	Stress-CMR and SPECT versus QCA	235	88%	83%

CMR: cardiac magnetic resonance; QCA: quantitative coronary angiography; SPECT: single photon emission computed tomography.

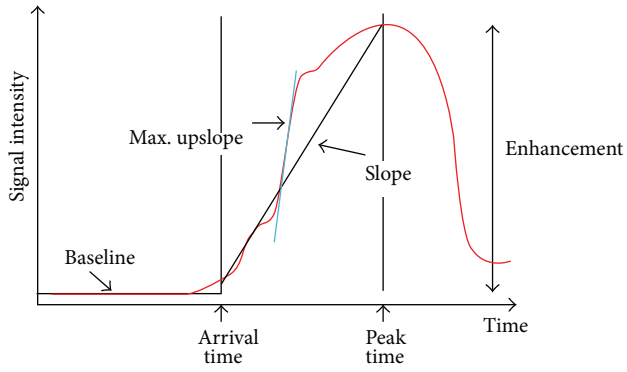

Figure 4: Time course of gadolinium myocardium enhancement. The time attenuation curve within a region of interest is obtained by fitting several sampling of myocardial signal intensity over time during the first pass imaging. For each curve arrival time, peak time and slope can be measured and compared between stress and rest condition. Modified by Patel et al. [21].

performance of stress-CMR versus SPECT with an area under the curve (AUC) of 0.86 ± 0.06 versus 0.67 ± 0.05 (P: 0.013), respectively. It is important to note that in this study, gated-SPECT, that is considered now the standard technique for stress nuclear tests, was available in approximately half of patients. Moreover, the population evaluated in MR-IMPACT I was at high risk for CAD that is not the typical population referred to noninvasive stress tests in clinical practice. In MR-IMPACT II trial [25] 533 patients were enrolled in 33 centres and evaluated by stress-CMR and gated-SPECT before ICA. The study population was at intermediate risk of CAD as proved by prevalence of obstructive coronary stenoses. No differences were found between the stress-CMR and SPECT in terms of percentage of not-evaluable tests (5.6% versus 3.7%, resp.; P: 0.21) while stress-CMR showed a higher sensitivity score (0.67 versus 0.59, resp.; P: 0.024) but a lower specificity score (0.61 versus 0.72, resp.; P: 0.038). In the larger multicenter trial CE-MARC [24], stress-CMR and SPECT showed sensitivity, specificity, positive predictive value, and negative predictive value of 86%, 83%, 77%, and 90% and 66%, 82%, 71%, and 79%, respectively. The sensitivity and negative predictive value of stress-CMR and SPECT differed significantly ($P < 0.0001$ for both) but specificity and positive predictive value did not. Moreover, stress-CMR showed a higher AUC as compared to SPECT (0.89 versus 0.79; $P < 0.0001$) regardless of the threshold used to define the presence of obstructive CAD (50% or 70% of coronary artery stenoses) and regardless of the presence of one or multiple vessels disease. Importantly, in CE-MARC trial a multiparametric protocol has been used including wall motion at rest by balanced steady-state free precession cine imaging, stress and rest perfusion by T1-weighted saturation recovery, evaluation of coronary artery stenoses by 3D coronary magnetic resonance angiography, and LGE by T1-weighted segmented inversion-recovery gradient-echo pulse sequence. A positive stress-CMR was defined as any evidence of regional wall motion abnormality and/or perfusion defect at stress and/or the presence of obstructive coronary artery stenoses and/or any scar. Of note in a gender-based subanalysis of CE-MARC trial [26] stress-CMR has greater sensitivity than SPECT in both genders and, unlike SPECT, there are no significant gender differences in the diagnostic performance. In Figure 5, a clinical case of a 62-year-old man referred to dipyridamole stress-CMR for exertional chest pain is reported.

2.1.4. Stress-CMR for Prognostic Stratification of CAD. Over the past several years, multiple studies have been published regarding stress-CMR assessment of prognosis. In a recent meta-analysis, Lipinski et al. [27] showed in 11636 patients that the combined outcome annualized event rates were 0.8% for negative study and 4.9% for positive study with the evidence of LGE significantly associated with worse prognosis as well. Macwar et al. [28] found an annual event rate for hard events of 0.6%, 1.7%, and 1.5% in normal, positive for LGE, and positive for reversible perfusion defect adenosine stress-CMR, respectively, in 564 patients symptomatic for chest pain without previous history of revascularization. Similarly, Buckert et al. [29] showed a hazard ratio of 3.2 associated with reversible perfusion defect in a larger population (1152 patients) in a long-term follow-up (4.2 years). These data support consistent and robust prognostic stratification by adenosine stress-CMR and it seems that this robustness is preserved regardless of patient's gender [30]. Regarding dobutamine studies, Kelle et al. [31] showed that, in a large cohort (1369 patients) evaluated with dobutamine stress-CMR, the annual cardiac event rate of a negative stress test was 1.1%, while the hazard ratio associated with a positive dobutamine stress test was 3.3. Similarly, Wallace et al. [32] found that the presence of inducible AWM is associated with a hazard ratio of 2.7 for future hard cardiac events in 221 consecutive women. Only few studies have tested the usefulness of dipyridamole stress-CMR for predicting spontaneous clinical events [33, 34]. Bodi et al. [33] found that the prognostic value of perfusion deficit was weaker

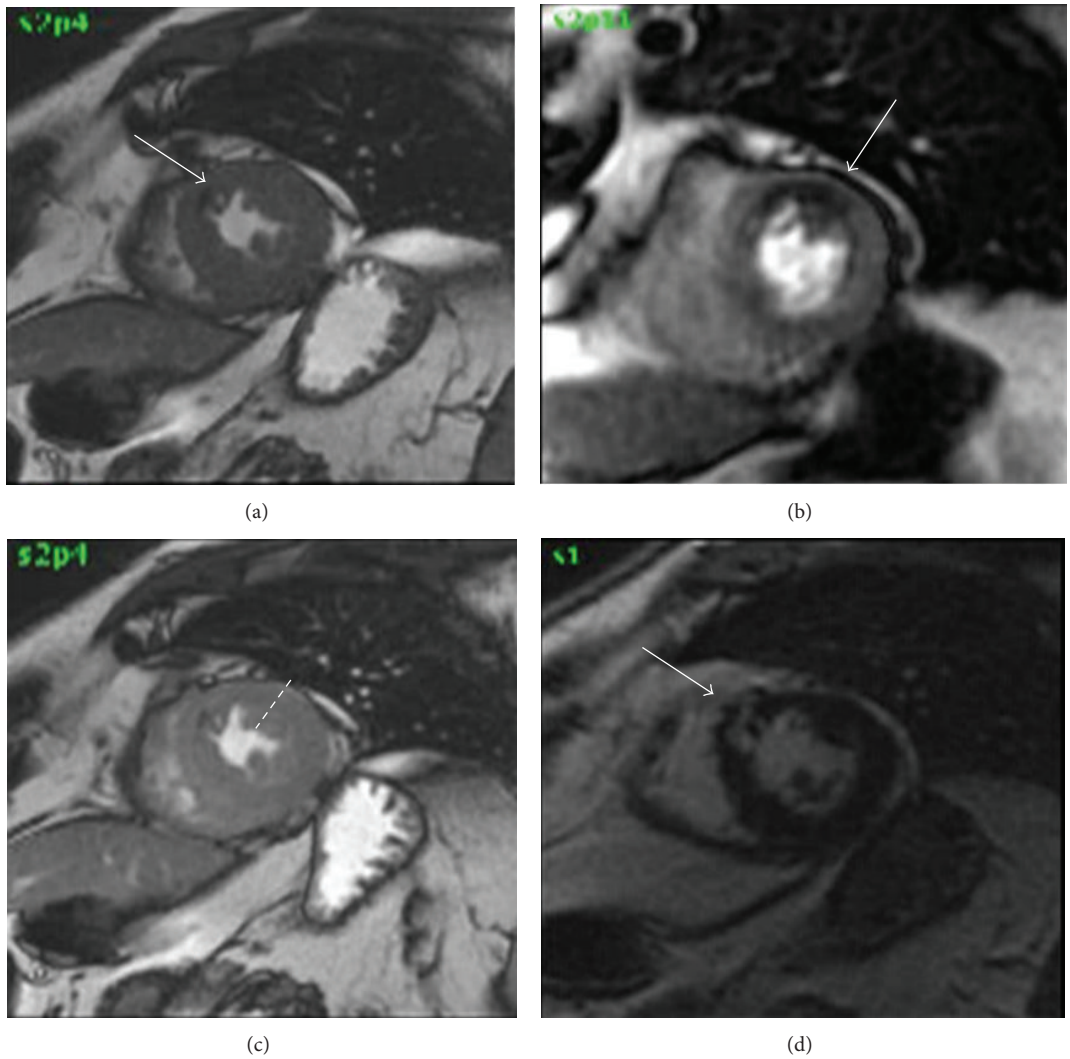

Figure 5: Clinical case. Dipyridamole stress-CMR in a 62-year-old man with familiar history of CAD and hypertension, referred to chest pain. Cine images at rest (Panel (a)) showed akinesis of anterior interventricular septum (arrow). Under stress, first pass perfusion images showed a large perfusion defect in anterior wall of left ventricle (Panel (b), arrow) without matched wall motion abnormalities (Panel (c), arrow). Late gadolinium enhancement images show an unknown transmural myocardial infarction of anterior interventricular septum (Panel (d), arrow).

than AWM under stress suggesting that kinesis evaluation is desirable beyond the perfusion. The latter point was evaluated in a following paper from the same authors [34] in 601 consecutive patients with a mean follow-up of 640 days with an annual hard event rate of 2.9%, 11.7%, and 14.1% in the three categories described above, respectively. This progressive increase of hard event rate in these three categories finds an explanation in the evidence that the extent of the perfusion defect is larger in patients with concomitant AWM [34, 35].

2.1.5. Future Perspectives. Three main fields of investigation are developing in the detection of CAD by CMR. First, whole heart stress-CMR perfusion techniques have been developed in order to permit quantification of ischemic tissue volume [36]. This approach proved to be highly diagnostic for the detection of CAD based on invasive FFR, showing similar sensitivity but improved specificity (90 versus 92% and 82 versus 74%, resp.) as compared to previously published data. Jogiya et al. [37] demonstrated that whole heart myocardial perfusion CMR accurately detects functionally significant coronary artery disease highlighting the concept that diagnostic accuracy was equally high in patients with single-vessel and multivessel coronary artery disease and that the amount of myocardial ischemic burden gradually increased with more proximal anatomical localization of coronary lesions. This method may be considered a noninvasive approach to stratify patients before coronary angiography to identify that

cut-off of 10% of myocardial ischemic burden that is actually accepted as threshold for indication of interventional revascularization. Second, the "blood oxygen level-dependent" (BOLD) stress-CMR [38] has become a promising investigative method. The rationale of this promising method is that oxyhemoglobin is slightly diamagnetic and deoxyhemoglobin paramagnetic resulting in the loss of $T2^*$ and T2 signal. Therefore, BOLD CMR uses an endogenous contrast without additional use of an exogenous contrast. Using a T2-prepared steady-state free precession, BOLD stress-CMR sequences can be used to image changes of myocardial oxygenation induced by drug stressors as an indicator of myocardial ischemia. Myocardial perfusion assessed by the change in myocardial oxygenation with those new sequences has been correlated with quantitative coronary angiography and later with fractional flow reserve to better characterize the clinical significance of coronary stenosis [38]. Third future perspective is to visualize the atherosclerotic plaque of coronary arteries. Early reports demonstrated the principal feasibility of the contrast enhancement magnetic resonance coronary angiography (CEMRA) to visualize the coronary artery stenoses noninvasively showing some limitations both in sensitivity and in specificity as compared to ICA [39, 40]. A new family of contrast agents that may play an important role in investigating molecular and cellular targets associated with atherosclerotic plaque development has been recently shown [41, 42]. A prospective multicenter trial [43] evaluated the diagnostic ability of navigator-corrected SSFP whole-heart MRCA sequences to detect significant coronary artery stenosis (≥50% reduction in diameter) with ultrasmall superparamagnetic iron oxide nanoparticles showing a sensitivity and a specificity of 88% and 72% with a negative predictive value of 88% in a patient-based analysis as compared to ICA.

2.2. Functional Relevance of CAD by CCT. The advancement of CCT has enabled the noninvasive evaluation of coronary artery stenosis in several clinical scenarios [44–48] with a low radiation exposure [49–51]. Despite high negative predictive value, factors such as high heart rate, arrhythmia, obesity, and high coronary calcium burden continue to limit the overall evaluability and positive predictive value of CCT [52, 53]. Moreover, obstructive CAD identified by CCT is not a robust predictor of functional relevance of stenoses [54]. So, the combination of overestimation of CAD and the absence of functional information could be responsible for a false positive rate up to 35% of patients that is common event in experienced centers [55]. Thus, a combined anatomic and functional assessment of CAD is desirable to improve the yield of ICA [56]. This aim can be reached by stress-CCT and FFR-CT. In this section, we will briefly summarize the technical bases and preliminary clinical findings of these emerging novel techniques.

2.2.1. Perfusion Stress Cardiac Computed Tomography. Investigation in the field of stress-CCT started 2 decades ago [57, 58]. Unfortunately, the clinical use of this technique has remained restricted due to several technical limitations such as the limited temporal resolution, spatial and contrast resolution, and the z-axis coverage. Indeed, during a stress-CCT, the contrast agent arrives to myocardial wall and it attenuates X-ray based on its concentration. Thus, area with perfusion defect is simply detectable as region with hypoattenuation. However, the highest concentration of iodine in the myocardium is reached in 1 minute after injection with a very fast washout [59]. To imagine this very rapid phenomenon, a high temporal resolution is mandatory. Some strategies have been used to improve temporal resolution of CCT [60]. The first strategy is to increase gantry rotation time. Indeed, in order to accurately reconstruct an image, the projection data are acquired within an angular range of 180° plus a 60° fan angle with a minimal data acquisition angular range of 240°. This fact determines that the typical temporal resolution of CCT is about 50–60% of the gantry rotation time [61]. Accordingly, the highest maximum temporal resolution achievable for single source scanner is 135 msec that is far from the desirable temporal resolution reached by ICA that is around 20–30 msec. The introduction of dual source CT (DSCT) has partially overcome this limitation. This system combines 2 arrays consisting of 1 tube and 1 detector each, arranged within the same gantry at a 90° offset, so that one-quarter rotation is sufficient to sample X-ray transmission data over 180° of projections. With a gantry rotation time of 330 ms, the system could achieve a temporal resolution of 83 ms that is significantly higher than single source CCT [62]. More recently, intracycle motion correction algorithm that allows a compensation of coronary motion by using multiphasic analysis of coronary arteries within a single cardiac cycle has been developed for single source scanner reaching a temporal resolution of 25 msec [63, 64]. However, a high temporal resolution needs to be matched with a very fast scan time. There are two strategies to improve the scan time: a higher craniocaudal coverage by increasing the number of slices or a higher pitch or the combination of the two strategies. Craniocaudal coverage of 64-slice CCT coronary angiography is typically less than 40 mm, giving limited coverage width. The development of wide area detector CCT [65] enabled greater coverage per gantry rotation and the extension from 64-slice MDCT to 256-detector row or 320-detector row system has enabled whole heart coverage. The 256-CCT has 912 (transverse) × 256 (craniocaudal) elements, each approximately 0.5 × 0.5 mm at the center of rotation with craniocaudal coverage of 128 mm per rotation. The 320-CCT system uses a detector element consisting of 320 × 0.5 mm detector and provides 160 mm of coverage in the z-direction [66]. The scan time can be reduced by increasing the pitch, as well. In 2008, a high pitch scanner has been introduced. It rotates with a gantry rotation time of 280 milliseconds, a wider detector with a pitch up to 3.2 that allows an overall scan time of about 0.27 seconds to cover the entire heart. This scan mode, known as "Flash CT," enables complete image acquisition within one cardiac cycle so that the X-ray tube and detector rotate around the patient without overlap and with very short scan time [67]. After temporal resolution, a second challenge in stress-CCT is to improve the spatial and contrast resolution in the myocardial wall. Indeed, the difference in terms of contrast attenuation between normal and hypoperfused myocardial

Table 3: Characteristics of a selected list of studies of the diagnostic performance of stress myocardial perfusion cardiac computed tomography imaging.

Author	Reference	*N*	Effective radiation dose (mSv)	Sensitivity	Specificity
George et al. [73]	Stress-CCT versus QCA + SPECT	27	16.8	86%	92%
Blankstein et al. [74]	Stress-CCT and SPECT versus QCA	33	12.7	92%	67%
Rocha-Filho et al. [75]	Stress-CCT versus QCA	34	11.8	96%	100%
Cury et al. [77]	Stress-CCT and SPECT versus QCA	36	14.7	94%	75%
Ho et al. [78]	Stress-CCT versus QCA + SPECT	35	18.2	95%	65%
Bamberg et al. [81]	Stress-CCT versus invasive FFR	33	13.1	95%	64%
Feutchtner et al. [82]	Stress-CCT versus stress-CMR	30	2.5	96%	88%

CCT: cardiac computed tomography; CMR: cardiac magnetic resonance; FFR: fractional flow reserve; QCA: quantitative coronary angiography; SPECT: single photon emission computed tomography.

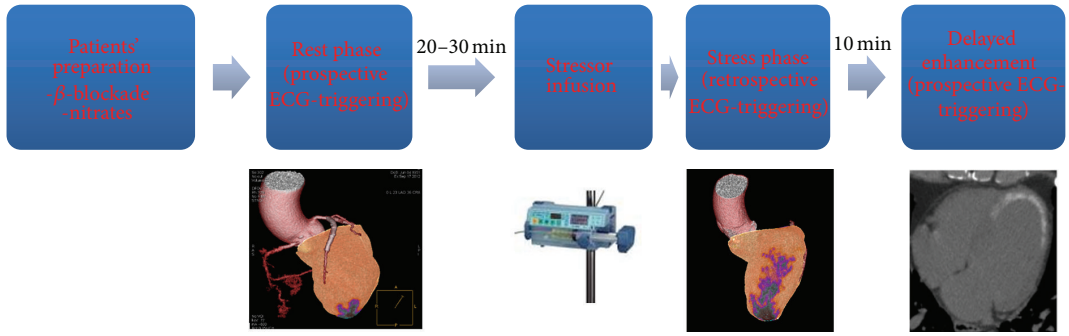

Figure 6: Scan protocol of stress cardiac computed tomography.

regions ranges in the order of 50 HU [68]. To highlight the small differences in contrast attenuation between normal and hypoperfused myocardium, it is suggested to use low tube voltage (100 KVp) to increase the photoelectric effect and to decrease the Compton scattering associated with low tube voltage [69]. However, the low tube voltage increases the image noise and the use of adaptive iterative reconstruction algorithm rather than the filtered back projection algorithm is recommended to limit the image noise increase when low tube voltage is employed [50]. Despite the use of low tube voltage and iterative reconstruction algorithm, the beam hardening artefacts continue to be an issue of concern during a stress-CCT because they can mimic a false perfusion defect. These artifacts are due to the polychromatic nature of X-rays and the energy dependency of X-ray attenuation phenomenon [6]. Indeed, X-ray photons with lower energies are preferentially attenuated and this inconsistency of X-ray between different views results in misregistration of X-ray attenuation producing false perfusion defect [6]. Recently the dual energy computed tomography (DECT) has been introduced to overcome this limitation [70]. This technique simultaneously acquires 2 sets of projections using 2 different X-ray energy spectra. In this way, DECT seems to be more effective for correcting beam hardening artifacts due to the ability to reconstruct monochromatic CCT images [71]. So far, based on technology available, two main kinds of stress-CT can be performed. Static stress-CCT imaging is usually preferred for scanner with low temporal resolution and long scan time in which the myocardial perfusion is reached from a single data sample acquired in arterial phase timing. On the other side, the dynamic stress-CCT imaging, usually performed with scanner with high temporal resolution and low scan time, is obtained from multiple samples of myocardial attenuation at sequential time points after contrast injection with a method similarly to the stress-CMR previously described. For both approaches, the adenosine infusion is usually used as stressor with the same protocol described for stress-CMR. In Figure 6, the most common protocol used in clinical practice is briefly described. Up to now, a few single-centre studies [72–83] are available regarding the diagnostic accuracy of stress-CCT and they are summarized in Table 3 with a mean effective radiation dose of rest plus stress scan of about 11 mSv that is comparable with the mean radiation exposure usually associated with SPECT [51]. More recently, a multicenter trial CORE 320 [84] has evaluated the diagnostic accuracy of stress-CCT as compared to the combination of SPECT plus ICA. The results of this trial showed in a patient-based model AUC of 0.87 for integrated CCT and perfusion as compared to the algorithm SPECT plus ICA. Figure 7 showed one case of stress-CCT with single source dual energy technique.

2.2.2. Fractional Flow Reserve by Cardiac Computed Tomography (FFR-CT). In the "era" of FAME trial an emerging

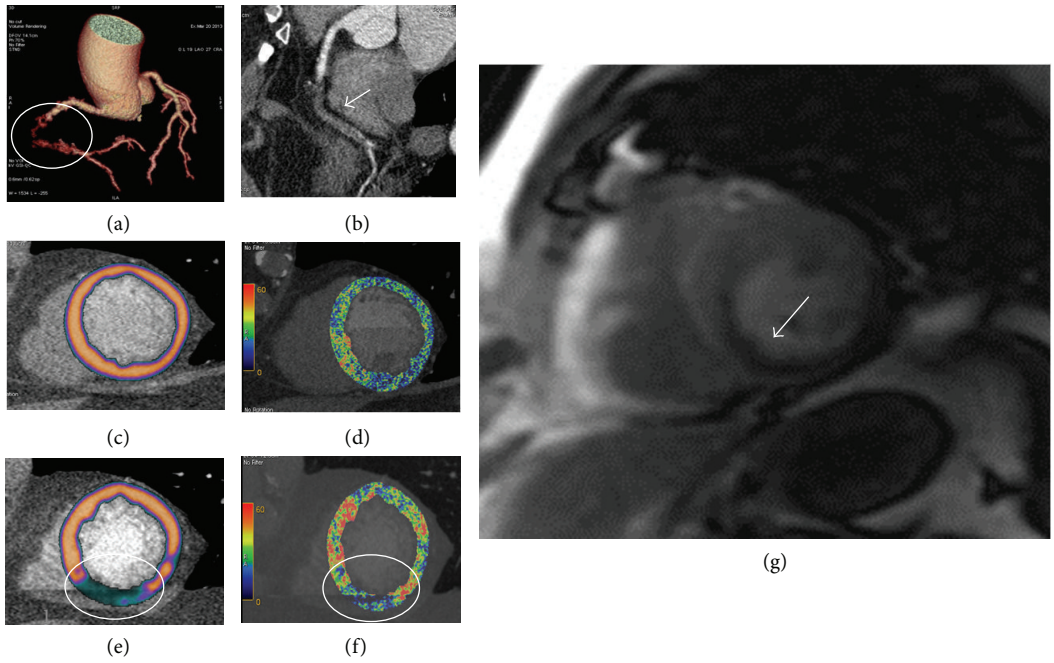

Figure 7: Clinical case of a 61-year-old man referred for suspected coronary artery disease. To rule out the presence of significant coronary artery disease and ischemia, a rest-stress dual energy CCT has been performed. The exam showed a chronic total occlusion of the right coronary artery (Panel (a) circle, Panel (b) arrow) due to a noncalcified plaque. The myocardial perfusion (Panel (c)) and iodine map (Panel (d)) at rest do not show significant perfusion defect. Under stress condition (i.v. adenosine injection), dual energy computed tomography showed a large perfusion defect in inferior wall of left ventricle (Panel (e) and (f), circle) with good matching as compared to stress cardiac magnetic resonance (Panel (g), arrow). CCT: cardiac computed tomography.

interest has been increased on the possibility to measure in a noninvasive setting the FFR. To this regard, software to determine FFR which computes the hemodynamic significance of CAD from CCT dataset (FFR-CT) using computational fluid dynamics under rest and simulated maximal coronary hyperemic conditions has been recently developed [85]. Although the description of technical aspects of this method is beyond the aim of this paper, the computation of FFR-CT can be summarized as an integration of anatomic model of coronary arteries derived by CCT plus a mathematical model of coronary physiology including numerical solution of the laws of physics governing fluid dynamics [85]. In other words, the combination of high-resolution anatomic definition of CAD via CCT with FFR-CT in a single test without the use of stressors provides a noninvasive anatomic and functional assessment of CAD in one-shot scan without the need of additional functional test in case of obstructive CAD at CCT. Results from 3 prospective multicenter trials have validated the accuracy of FFR-CT as compared to invasive FFR [86–88]. Koo et al. compared in DISCOVER-FLOW trial the FFR-CT versus invasive FFR in 103 consecutive patients in a vessel-based model showing diagnostic accuracy, sensitivity, specificity, positive predictive value, and negative predictive value of 84%, 88%, 82%, 74%, and 92%, respectively. The FFR-CT increased the AUC from 0.75 for CCT alone up to 0.91 (P: 0.001) and showed a good correlation with invasive FFR (0.71, $P < 0.001$). The main limitation of DISCOVER-FLOW is that it was powered to evaluate the diagnostic accuracy in a per-vessel model rather than per-patient model. The latter point was evaluated in DE-FACTO trial [87] where, in larger sample size of 252 patients, the FFR-CT showed diagnostic accuracy, sensitivity, specificity, positive predictive value, and negative predictive value of 73%, 90%, 54%, 67%, and 84%, respectively, improving the AUC from 0.68 to 0.81 when compared with CCT alone without functional evaluation. More recently, the NXT trial [88] has demonstrated per-patient sensitivity and specificity of 86% and 79%, respectively, with AUC of 0.9 as compared to invasive FFR. Of note, in patents with intermediate stenoses (the most common setting of patients evaluated with noninvasive stress test) the diagnostic performance of FFR-CT remained unchanged. Differently for the two previous studies, the last generation of FFR-CT software has been used, nitrates was employed in 99% of study population against only 75% of DEFACTO study population, and, last but not least, an intermediate risk population was included rather than high-risk patients such as the two previous studies. The main limitation of FFR-CT remains still the not-negligible rate of not-evaluable patients that reaches the 13% in the NXT-trial due to the poor image quality. So far, the clinical validation of FFR-CT opens the issue if the use of this software integrated to CCT dataset is reasonable in terms of cost-effectiveness in intermediate risk patients by "one-stop shop" offering coronary anatomy and functional relevance of CAD. The final answer to this

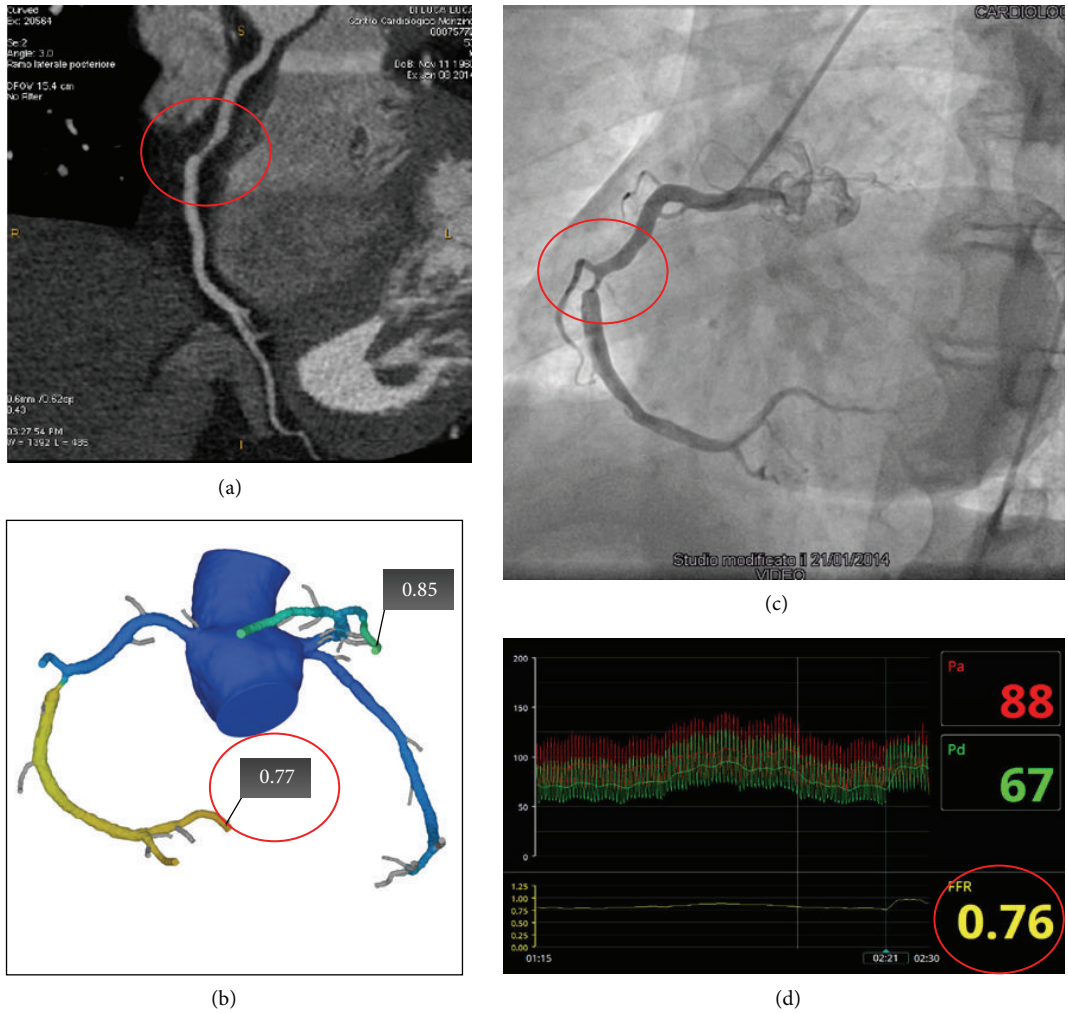

Figure 8: Clinical case of an intermediate risk patient symptomatic for chest pain. Panel (a) showed a multiplanar reconstruction of CCT showing an obstructive stenosis of the middle right coronary artery (red circle) and computed fractional flow reserve (FFR-CT) value of 0.77, indicating vessel ischemia (Panel (b)). Invasive coronary angiography confirmed the obstructive stenosis of the middle portion of the right coronary artery (Panel (c), red circle) and measured fractional flow reserve (FFR) values of 0.76 (Panel (d), red circle). CCT: cardiac computed tomography.

crucial question will arrive with the ongoing PLATFORM trial (Prospective LongitudinAl Trial of FFRct: Outcome and Resource IMpacts) that has the aim to compare the rate of ICA documenting nonobstructive CAD, clinical outcomes, quality of life, and resource utilization following standard practice versus incorporating FFR-CT as the preferred test to guide further noninvasive or invasive management and medical treatment of patients. Figure 8 shows a clinical case of patient in which FFR-CT has been performed and compared to invasive FFR.

3. Conclusions

The world of cardiac imaging in the field of CAD is proposing an increasing number of techniques with the aim to rule out the presence of CAD and to identify the high-risk patients who will benefit from expensive invasive procedures. There is robust evidence that, to reach this aim, both coronary anatomy and function need to be evaluated. How to obtain combined anatomic and functional noninvasive imaging by using one or multiple imaging modalities still has not been demonstrated and it will be issue of debate for the next years ensuring that "exciting times are ahead of cardiac imagers."

Disclosure

Gianluca Pontone has been on Speakers' Bureau for GE Healthcare, Heartflow, Medtronic, Bayer, and consultant for GE Healthcare, Heartflow. Daniele Andreini has been on Speakers' Bureau and consultant for GE Healthcare.

Conflict of Interests

The authors, except for Gianluca Pontone and Daniele Andreini, declare that there is no conflict of interests regarding the publication of this paper.

References

[1] M. R. Patel, G. J. Dehmer, J. W. Hirshfeld, P. K. Smith, and J. A. Spertus, "ACCF/SCAI/STS/AATS/AHA/ASNC/HFSA/SCCT 2012 Appropriate use criteria for coronary revascularization focused update: a report of the American College of Cardiology Foundation Appropriate Use Criteria Task Force, Society for Cardiovascular Angiography and Interventions, Society of Thoracic Surgeons, American Association for Thoracic Surgery, American Heart Association, American Society of Nuclear Cardiology, and the Society of Cardiovascular Computed Tomography," *Journal of the American College of Cardiology*, vol. 59, pp. 857–881, 2012.

[2] M. R. Patel, E. D. Peterson, D. Dai et al., "Low diagnostic yield of elective coronary angiography," *The New England Journal of Medicine*, vol. 362, no. 10, pp. 886–895, 2010.

[3] W. E. Boden, R. A. O'Rourke, K. K. Teo et al., "Optimal medical therapy with or without PCI for stable coronary disease," *The New England Journal of Medicine*, vol. 356, no. 15, pp. 1503–1516, 2007.

[4] L. J. Shaw, D. S. Berman, D. J. Maron et al., "Optimal medical therapy with or without percutaneous coronary intervention to reduce ischemic burden: results from the Clinical Outcomes Utilizing Revascularization and Aggressive Drug Evaluation (COURAGE) trial nuclear substudy," *Circulation*, vol. 117, no. 10, pp. 1283–1291, 2008.

[5] O. R. Coelho-Filho, C. Rickers, R. Y. Kwong, and M. Jerosch-Herold, "MR myocardial perfusion imaging," *Radiology*, vol. 266, no. 3, pp. 701–715, 2013.

[6] A. So and T.-Y. Lee, "Quantitative myocardial CT perfusion: a pictorial review and the current state of technology development," *Journal of Cardiovascular Computed Tomography*, vol. 5, no. 6, pp. 467–481, 2011.

[7] F. J. Klocke, "Measurements of coronary flow reserve: defining pathophysiology versus making decisions about patient care," *Circulation*, vol. 76, no. 6, pp. 1183–1189, 1987.

[8] K. L. Gould, K. Lipscomb, and G. W. Hamilton, "Physiologic basis for assessing critical coronary stenosis. Instantaneous flow response and regional distribution during coronary hyperemia as measures of coronary flow reserve," *The American Journal of Cardiology*, vol. 33, no. 1, pp. 87–94, 1974.

[9] K. L. Gould, R. L. Kirkeeide, and M. Buchi, "Coronary flow reserve as a physiologic measure of stenosis severity," *Journal of the American College of Cardiology*, vol. 15, no. 2, pp. 459–474, 1990.

[10] L. Belardinelli, J. C. Shryock, S. Snowdy et al., "The A2A adenosine receptor mediates coronary vasodilation," *Journal of Pharmacology and Experimental Therapeutics*, vol. 284, no. 3, pp. 1066–1073, 1998.

[11] R. C. Cury, T. M. Kitt, K. Feaheny, J. Akin, and R. T. George, "Regadenoson-stress myocardial CT perfusion and single-photon emission CT: rationale, design, and acquisition methods of a prospective, multicenter, multivendor comparison," *Journal of Cardiovascular Computed Tomography*, vol. 8, no. 1, pp. 2–12, 2014.

[12] N. H. J. Pijls and J.-W. E. M. Sels, "Functional measurement of coronary stenosis," *Journal of the American College of Cardiology*, vol. 59, no. 12, pp. 1045–1057, 2012.

[13] P. A. L. Tonino, B. de Bruyne, N. H. J. Pijls et al., "Fractional flow reserve versus angiography for guiding percutaneous coronary intervention," *The New England Journal of Medicine*, vol. 360, no. 3, pp. 213–224, 2009.

[14] B. de Bruyne, N. H. J. Pijls, B. Kalesan et al., "Fractional flow reserve-guided PCI versus medical therapy in stable coronary disease," *The New England Journal of Medicine*, vol. 367, no. 11, pp. 991–1001, 2012.

[15] B. De Bruyne, J. Bartunek, S. U. Sys, N. H. J. Pijls, G. R. Heyndrickx, and W. Wijns, "Simultaneous coronary pressure and flow velocity measurements in humans: feasibility, reproducibility, and hemodynamic dependence of coronary flow velocity reserve, hyperemic flow versus pressure slope index, and fractional flow reserve," *Circulation*, vol. 94, no. 8, pp. 1842–1849, 1996.

[16] G. J. W. Bech, B. de Bruyne, N. H. J. Pijls et al., "Fractional flow reserve to determine the appropriateness of angioplasty in moderate coronary stenosis: a randomized trial," *Circulation*, vol. 103, no. 24, pp. 2928–2934, 2001.

[17] N. H. J. Pijls, P. van Schaardenburgh, G. Manoharan et al., "Percutaneous coronary intervention of functionally non significant stenosis: 5-year follow-up of the DEFER Study," *Journal of the American College of Cardiology*, vol. 49, no. 21, pp. 2105–2111, 2007.

[18] N. H. J. Pijls, B. Van Gelder, P. Van der Voort et al., "Fractional flow reserve: a useful index to evaluate the influence of an epicardial coronary stenosis on myocardial blood flow," *Circulation*, vol. 92, no. 11, pp. 3183–3193, 1995.

[19] M. B. Iqbal, N. Shah, M. Khan, and W. Wallis, "Reduction in myocardial perfusion territory and its effect on the physiological severity of a coronary stenosis," *Circulation: Cardiovascular Interventions*, vol. 3, no. 1, pp. 89–90, 2010.

[20] C. M. Kramer, J. Barkhausen, S. D. Flamm, R. J. Kim, and E. Nagel, "Standardized cardiovascular magnetic resonance imaging (CMR) protocols, society for cardiovascular magnetic resonance: board of trustees task force on standardized protocols," *Journal of Cardiovascular Magnetic Resonance*, vol. 10, no. 1, article 35, 2008.

[21] A. R. Patel, P. F. Antkowiak, K. R. Nandalur et al., "Assessment of advanced coronary artery disease: advantages of quantitative cardiac magnetic resonance perfusion analysis," *Journal of the American College of Cardiology*, vol. 56, no. 7, pp. 561–569, 2010.

[22] K. R. Nandalur, B. A. Dwamena, A. F. Choudhri, M. R. Nandalur, and R. C. Carlos, "Diagnostic performance of stress cardiac magnetic resonance imaging in the detection of coronary artery disease: a meta-analysis," *Journal of the American College of Cardiology*, vol. 50, no. 14, pp. 1343–1353, 2007.

[23] J. Schwitter, C. M. Wacker, A. C. Van Rossum et al., "MR-IMPACT: comparison of perfusion-cardiac magnetic resonance with single-photon emission computed tomography for the detection of coronary artery disease in a multicentre, multivendor, randomized trial," *European Heart Journal*, vol. 29, no. 4, pp. 480–489, 2008.

[24] J. P. Greenwood, N. Maredia, J. F. Younger et al., "Cardiovascular magnetic resonance and single-photon emission computed tomography for diagnosis of coronary heart disease (CE-MARC): a prospective trial," *The Lancet*, vol. 379, no. 9814, pp. 453–460, 2012.

[25] J. Schwitter, C. M. Wacker, N. Wilke et al., "MR-IMPACT Investigators. MR-IMPACT II: magnetic Resonance Imaging for Myocardial Perfusion Assessment in Coronary artery disease trial: perfusion-cardiac magnetic resonance vs. single-photon emission computed tomography for the detection of coronary artery disease: a comparative multicentre, multivendor trial," *European Heart Journal*, vol. 34, pp. 775–781, 2013.

[26] J. P. Greenwood, M. Motwani, N. Maredia et al., "Comparison of cardiovascular magnetic resonance and single-photon emission computed tomography in women with suspected coronary artery disease from the clinical evaluation of magnetic resonance imaging in coronary heart disease (CE-MARC) trial," *Circulation*, vol. 129, no. 10, pp. 1129–1138, 2014.

[27] M. J. Lipinski, C. M. McVey, J. S. Berger, C. M. Kramer, and M. Salerno, "Prognostic value of stress cardiac magnetic resonance imaging in patients with known or suspected coronary artery disease: a systematic review and meta-analysis," *Journal of the American College of Cardiology*, vol. 62, no. 9, pp. 826–838, 2013.

[28] R. R. Macwar, B. A. Williams, and J. Shirani, "Prognostic value of adenosine cardiac magnetic resonance imaging in patients presenting with chest pain," *American Journal of Cardiology*, vol. 112, no. 1, pp. 46–50, 2013.

[29] D. Buckert, P. Dewes, T. Walcher, W. Rottbauer, and P. Bernhardt, "Intermediate-term prognostic value of reversible perfusion deficit diagnosed by adenosine CMR: a prospective follow-up study in a consecutive patient population," *JACC: Cardiovascular Imaging*, vol. 6, no. 1, pp. 56–63, 2013.

[30] O. R. Coelho-Filho, L. F. Seabra, F.-P. Mongeon et al., "Stress myocardial perfusion imaging by CMR provides strong prognostic value to cardiac events regardless of patient's sex," *JACC: Cardiovascular Imaging*, vol. 4, no. 8, pp. 850–861, 2011.

[31] S. Kelle, A. Chiribiri, J. Vierecke et al., "Long-term prognostic value of dobutamine stress CMR," *JACC: Cardiovascular Imaging*, vol. 4, no. 2, pp. 161–172, 2011.

[32] E. L. Wallace, T. M. Morgan, T. F. Walsh et al., "Dobutamine cardiac magnetic resonance results predict cardiac prognosis in women with known or suspected ischemic heart disease," *JACC: Cardiovascular Imaging*, vol. 2, no. 3, pp. 299–307, 2009.

[33] V. Bodi, J. Sanchis, M. P. Lopez-Lereu et al., "Prognostic value of dipyridamole stress cardiovascular magnetic resonance imaging in patients with known or suspected coronary artery disease," *Journal of the American College of Cardiology*, vol. 50, no. 12, pp. 1174–1179, 2007.

[34] V. Bodi, J. Sanchis, M. P. Lopez-Lereu et al., "Prognostic and therapeutic implications of dipyridamole stress cardiovascular magnetic resonance on the basis of the ischaemic cascade," *Heart*, vol. 95, no. 1, pp. 49–55, 2009.

[35] I. Paetsch, C. Jahnke, A. Wahl et al., "Comparison of dobutamine stress magnetic resonance, adenosine stress magnetic resonance, and adenosine stress magnetic resonance perfusion," *Circulation*, vol. 110, no. 7, pp. 835–842, 2004.

[36] R. Manka, I. Paetsch, S. Kozerke et al., "Whole-heart dynamic three-dimensional magnetic resonance perfusion imaging for the detection of coronary artery disease defined by fractional flow reserve: determination of volumetric myocardial ischaemic burden and coronary lesion location," *European Heart Journal*, vol. 33, no. 16, pp. 2016–2024, 2012.

[37] R. Jogiya, S. Kozerke, G. Morton et al., "Validation of dynamic 3-dimensional whole heart magnetic resonance myocardial perfusion imaging against fractional flow reserve for the detection of significant coronary artery disease," *Journal of the American College of Cardiology*, vol. 60, no. 8, pp. 756–765, 2012.

[38] S. A. Tsaftaris, X. Zhou, R. Tang, D. Li, and R. Dharmakumar, "Detecting myocardial ischemia at rest with cardiac phase-resolved blood oxygen level-dependent cardiovascular magnetic resonance," *Circulation: Cardiovascular Imaging*, vol. 6, no. 2, pp. 311–319, 2013.

[39] W. J. Manning, W. Li, and R. R. Edelman, "A preliminary report comparing magnetic resonance coronary angiography with conventional angiography," *The New England Journal of Medicine*, vol. 328, no. 12, pp. 828–832, 1993.

[40] L. Cheng, Y. Gao, A. I. Guaricci et al., "Breath-hold 3D steady-state free precession coronary MRA compared with conventional X-ray coronary angiography," *Journal of Magnetic Resonance Imaging*, vol. 23, no. 5, pp. 669–673, 2006.

[41] J. R. Kanwar, X. Sun, V. Punj et al., "Nanoparticles in the treatment and diagnosis of neurological disorders: Untamed dragon with fire power to heal," *Nanomedicine*, vol. 8, no. 4, pp. 399–414, 2012.

[42] F. Perez-Balderas, B. G. Davis, S. I. van Kasteren et al., "New biodegradable multimeric MR contrast agent shows rapid in vitro and in vivo degradation and high sensitivity contrast," *Proceedings of the International Society for Magnetic Resonance in Medicine*, vol. 19, p. 1689, 2011.

[43] S. Kato, K. Kitagawa, N. Ishida et al., "Assessment of coronary artery disease using magnetic resonance coronary angiography: a national multicenter trial," *Journal of the American College of Cardiology*, vol. 56, no. 12, pp. 983–991, 2010.

[44] W. B. Meijboom, C. A. G. van Mieghem, N. R. Mollet et al., "64-slice computed tomography coronary angiography in patients with high, intermediate, or low pretest probability of significant coronary artery disease," *Journal of the American College of Cardiology*, vol. 50, no. 15, pp. 1469–1475, 2007.

[45] R. Blankstein, W. Ahmed, F. Bamberg et al., "Comparison of exercise treadmill testing with cardiac computed tomography angiography among patients presenting to the emergency room with chest pain: the rule out myocardial infarction using computer-assisted tomography (ROMICAT) study," *Circulation: Cardiovascular Imaging*, vol. 5, no. 2, pp. 233–242, 2012.

[46] D. Andreini, G. Pontone, M. Pepi et al., "Diagnostic accuracy of multidetector computed tomography coronary angiography in patients with dilated cardiomyopathy," *Journal of the American College of Cardiology*, vol. 49, no. 20, pp. 2044–2050, 2007.

[47] G. Pontone, D. Andreini, A. L. Bartorelli et al., "Feasibility and accuracy of a comprehensive multidetector computed tomography acquisition for patients referred for balloon-expandable transcatheter aortic valve implantation," *American Heart Journal*, vol. 161, no. 6, pp. 1106–1113, 2011.

[48] P. Nardi, A. Pellegrino, A. Romagnoli et al., "Multidetector computed tomographic coronary angiography as an alternative to conventional coronary angiography in non-coronary surgical patients," *Journal of Cardiovascular Surgery*, vol. 52, no. 3, pp. 429–435, 2011.

[49] G. Pontone, D. Andreini, A. L. Bartorelli et al., "Diagnostic accuracy of coronary CT angiography: comparison between prospective and retrospective ECG triggering," *Journal of the American College of Cardiology*, vol. 54, no. 4, pp. 346–355, 2009.

[50] J. Leipsic, T. M. LaBounty, B. Heilbron et al., "Estimated radiation dose reduction using adaptive statistical iterative reconstruction in coronary CT angiography: the ERASIR study," *American Journal of Roentgenology*, vol. 195, no. 3, pp. 655–660, 2010.

[51] G. Pontone, D. Andreini, A. L. Bartorelli et al., "Comparison between low-dose multidetector computed coronary angiography and myocardial perfusion imaging test in patients with intermediate pre-test likelihood of coronary artery disease," *International Journal of Cardiology*, vol. 147, no. 3, pp. 454–457, 2011.

[52] G. L. Raff, M. J. Gallagher, W. W. O'Neill, and J. A. Goldstein, "Diagnostic accuracy of noninvasive coronary angiography using 64-slice spiral computed tomography," *Journal of the American College of Cardiology*, vol. 46, no. 3, pp. 552–557, 2005.

[53] M. Dewey, A. L. Vavere, A. Arbab-Zadeh et al., "Patient characteristics as predictors of image quality and diagnostic accuracy of MDCT compared with conventional coronary angiography for detecting coronary artery stenoses: CORE-64 multicenter international trial," *The American Journal of Roentgenology*, vol. 194, no. 1, pp. 93–102, 2010.

[54] J. M. van Werkhoven, J. D. Schuijf, O. Gaemperli et al., "Prognostic value of multislice computed tomography and gated single-photon emission computed tomography in patients with suspected coronary artery disease," *Journal of the American College of Cardiology*, vol. 53, no. 7, pp. 623–632, 2009.

[55] G. Mowatt, J. A. Cook, G. S. Hillis et al., "64-Slice computed tomography angiography in the diagnosis and assessment of coronary artery disease: systematic review and meta-analysis," *Heart*, vol. 94, no. 11, pp. 1386–1393, 2008.

[56] W. B. Meijboom, C. A. G. van Mieghem, N. van Pelt et al., "Comprehensive assessment of coronary artery stenoses : computed tomography coronary angiography versus conventional coronary angiography and correlation with fractional flow reserve in patients with stable angina," *Journal of the American College of Cardiology*, vol. 52, no. 8, pp. 636–643, 2008.

[57] C. J. Wolfkiel, J. L. Ferguson, E. V. Chomka et al., "Measurement of myocardial blood flow by ultrafast computed tomography," *Circulation*, vol. 76, no. 6, pp. 1262–1273, 1987.

[58] J. A. Rumberger, A. J. Feiring, M. J. Lipton, C. B. Higgins, S. R. Ell, and M. L. Marcus, "Use of ultrafast computed tomography to quantitate regional myocardial perfusion: a preliminary report," *Journal of the American College of Cardiology*, vol. 9, no. 1, pp. 59–69, 1987.

[59] J. H. Newhouse and R. X. Murphy Jr., "Tissue distribution of soluble contrast: effect of dose variation and changes with time," *The American Journal of Roentgenology*, vol. 136, no. 3, pp. 463–467, 1981.

[60] T. G. Flohr, R. Raupach, and H. Bruder, "Cardiac CT: how much can temporal resolution, spatial resolution, and volume coverage be improved?" *Journal of Cardiovascular Computed Tomography*, vol. 3, no. 3, pp. 143–152, 2009.

[61] J. Tang, J. Hsieh, and G.-H. Chen, "Temporal resolution improvement in cardiac CT using PICCS (TRI-PICCS): performance studies," *Medical Physics*, vol. 37, no. 8, pp. 4377–4388, 2010.

[62] S. Achenbach, U. Ropers, A. Kuettner et al., "Randomized comparison of 64-slice single- and dual-source computed tomography coronary angiography for the detection of coronary artery disease," *JACC: Cardiovascular Imaging*, vol. 1, no. 2, pp. 177–186, 2008.

[63] J. Leipsic, T. M. Labounty, C. J. Hague et al., "Effect of a novel vendor-specific motion-correction algorithm on image quality and diagnostic accuracy in persons undergoing coronary CT angiography without rate-control medications," *Journal of Cardiovascular Computed Tomography*, vol. 6, no. 3, pp. 164–171, 2012.

[64] T. A. Fuchs, J. Stehli, S. Dougoud et al., "Impact of a new motion-correction algorithm on image quality of low-dose coronary CT angiography in patients with insufficient heart rate control," *Academic Radiology*, vol. 21, no. 3, pp. 312–317, 2014.

[65] F. J. Rybicki, H. J. Otero, M. L. Steigner et al., "Initial evaluation of coronary images from 320-detector row computed tomography," *International Journal of Cardiovascular Imaging*, vol. 24, no. 5, pp. 535–546, 2008.

[66] S. Mori, K. Nishizawa, C. Kondo, M. Ohno, K. Akahane, and M. Endo, "Effective doses in subjects undergoing computed tomography cardiac imaging with the 256-multislice CT scanner," *European Journal of Radiology*, vol. 65, no. 3, pp. 442–448, 2008.

[67] S. Achenbach, M. Marwan, T. Schepis et al., "High-pitch spiral acquisition: a new scan mode for coronary CT angiography," *Journal of Cardiovascular Computed Tomography*, vol. 3, no. 2, pp. 117–121, 2009.

[68] R. T. George, A. Arbab-Zadeh, R. J. Cerci et al., "Diagnostic performance of combined noninvasive coronary angiography and myocardial perfusion imaging using 320-MDCT: the CT angiography and perfusion methods of the CORE320 multicenter multinational diagnostic study," *American Journal of Roentgenology*, vol. 197, no. 4, pp. 829–837, 2011.

[69] B. B. Ertl-Wagner, R.-T. Hoffmann, R. Bruning et al., "Multidetector row CT angiography of the brain at various kilovoltage settings," *Radiology*, vol. 231, no. 2, pp. 528–535, 2004.

[70] A. So, J. Hsieh, Y. Imai et al., "Prospectively ECG-triggered rapid kV-switching dual-energy CT for quantitative imaging of myocardial perfusion," *JACC: Cardiovascular Imaging*, vol. 5, no. 8, pp. 829–836, 2012.

[71] A. So, J. Hsieh, J.-Y. Li, J. Hadway, H.-F. Kong, and T.-Y. Lee, "Quantitative myocardial perfusion measurement using CT perfusion: a validation study in a porcine model of reperfused acute myocardial infarction," *International Journal of Cardiovascular Imaging*, vol. 28, no. 5, pp. 1237–1248, 2012.

[72] G. Pontone, L. Grancini, D. Andreini, M. Pepi, and A. L. Bartorelli, "Myocardial perfusion imaging using dual-energy computed tomography: a clinical case.," *European heart journal cardiovascular Imaging*, vol. 14, no. 8, p. 835, 2013.

[73] R. T. George, A. Arbab-Zadeh, J. M. Miller et al., "Adenosine stress 64-and 256-row detector computed tomography angiography and perfusion imaging a pilot study evaluating the transmural extent of perfusion abnormalities to predict atherosclerosis causing myocardial ischemia," *Circulation: Cardiovascular Imaging*, vol. 2, no. 3, pp. 174–182, 2009.

[74] R. Blankstein, L. D. Shturman, I. S. Rogers et al., "Adenosine-induced stress myocardial perfusion imaging using dual-source cardiac computed tomography," *Journal of the American College of Cardiology*, vol. 54, no. 12, pp. 1072–1084, 2009.

[75] J. A. Rocha-Filho, R. Blankstein, L. D. Shturman et al., "Incremental value of adenosine-induced stress myocardial perfusion imaging with dual-source CT at cardiac CT angiography," *Radiology*, vol. 254, no. 2, pp. 410–419, 2010.

[76] D. R. Okada, B. B. Ghoshhajra, R. Blankstein et al., "Direct comparison of rest and adenosine stress myocardial perfusion CT with rest and stress SPECT," *Journal of Nuclear Cardiology*, vol. 17, no. 1, pp. 27–37, 2010.

[77] R. C. Cury, T. A. Magalhães, A. C. Borges et al., "Dipyridamole stress and rest myocardial perfusion by 64-detector row computed tomography in patients with suspected coronary artery disease," *The American Journal of Cardiology*, vol. 106, no. 3, pp. 310–315, 2010.

[78] K.-T. Ho, K.-C. Chua, E. Klotz, and C. Panknin, "Stress and rest dynamic myocardial perfusion imaging by evaluation of complete time-attenuation curves with dual-source CT," *JACC: Cardiovascular Imaging*, vol. 3, no. 8, pp. 811–820, 2010.

[79] S. M. Ko, J. W. Choi, M. G. Song et al., "Myocardial perfusion imaging using adenosine-induced stress dual-energy computed tomography of the heart: comparison with cardiac magnetic resonance imaging and conventional coronary angiography," *European Radiology*, vol. 21, no. 1, pp. 26–35, 2011.

[80] B. K. Tamarappoo, D. Dey, R. Nakazato et al., "Comparison of the extent and severity of myocardial perfusion defects measured by CT coronary angiography and SPECT myocardial perfusion imaging," *JACC: Cardiovascular Imaging*, vol. 3, no. 10, pp. 1010–1019, 2010.

[81] F. Bamberg, A. Becker, F. Schwarz et al., "Detection of hemodynamically significant coronary artery stenosis: incremental diagnostic value of dynamic CT-based myocardial perfusion imaging," *Radiology*, vol. 260, no. 3, pp. 689–698, 2011.

[82] G. Feuchtner, R. Goetti, A. Plass et al., "Adenosine stress high-pitch 128-slice dual-source myocardial computed tomography perfusion for imaging of reversible myocardial ischemia comparison with magnetic resonance imaging," *Circulation: Cardiovascular Imaging*, vol. 4, no. 5, pp. 540–549, 2011.

[83] B. S. Ko, J. D. Cameron, I. T. Meredith et al., "Computed tomography stress myocardial perfusion imaging in patients considered for revascularization: a comparison with fractional flow reserve," *European Heart Journal*, vol. 33, no. 1, pp. 67–77, 2012.

[84] C. E. Rochitte, R. T. George, M. Y. Chen et al., "Computed tomography angiography and perfusion to assess coronary artery stenosis causing perfusion defects by single photon emission computed tomography: the CORE320 study," *European Heart Journal*, vol. 35, no. 17, pp. 1120–1130, 2014.

[85] C. A. Taylor, T. A. Fonte, and J. K. Min, "Computational fluid dynamics applied to cardiac computed tomography for noninvasive quantification of fractional flow reserve: scientific basis," *Journal of the American College of Cardiology*, vol. 61, no. 22, pp. 2233–2241, 2013.

[86] B.-K. Koo, A. Erglis, J.-H. Doh et al., "Diagnosis of ischemia-causing coronary stenoses by noninvasive fractional flow reserve computed from coronary computed tomographic angiograms. Results from the prospective multicenter DISCOVER-FLOW (Diagnosis of Ischemia-Causing Stenoses Obtained Via Noninvasive Fractional Flow Reserve) study," *Journal of the American College of Cardiology*, vol. 58, no. 19, pp. 1989–1997, 2011.

[87] J. K. Min, J. Leipsic, M. J. Pencina et al., "Diagnostic accuracy of fractional flow reserve from anatomic CT angiography," *Journal of the American Medical Association*, vol. 308, no. 12, pp. 1237–1245, 2012.

[88] B. L. Nørgaard, J. Leipsic, S. Gaur et al., "Diagnostic performance of noninvasive fractional flow reserve derived from coronary computed tomography angiography in suspected coronary artery disease: the NXT trial (Analysis of Coronary Blood Flow Using CT Angiography: Next Steps)," *Journal of the American College of Cardiology*, vol. 63, no. 12, pp. 1145–1155, 2014.

Hindawi Publishing Corporation
BioMed Research International
Volume 2014, Article ID 648021, 6 pages
http://dx.doi.org/10.1155/2014/648021

Clinical Study

Perfusion in the Tissue Surrounding Pancreatic Cancer and the Patient's Prognosis

Yoshihiro Nishikawa,[1] Yoshihisa Tsuji,[1] Hiroyoshi Isoda,[2] Yuzo Kodama,[1] and Tsutomu Chiba[1]

[1] *Department of Gastroenterology and Hepatology, Kyoto University Graduate School of Medicine, 54 Kawara-cho, Shogoin, Sakyo-ku, Kyoto 606-8507, Japan*
[2] *Department of Radiology, Kyoto University Graduate School of Medicine, 54 Kawara-cho, Shogoin, Sakyo-ku, Kyoto 606-8507, Japan*

Correspondence should be addressed to Yoshihisa Tsuji; ytsuji@kuhp.kyoto-u.ac.jp

Received 9 April 2014; Revised 15 July 2014; Accepted 31 August 2014; Published 11 September 2014

Academic Editor: Luca Volterrani

Objective. The objective was to investigate the relationship between prognosis in case of pancreatic cancer and perfusion in tissue surrounding pancreatic cancer using perfusion CT. *Methods*. We enrolled 17 patients diagnosed with inoperable pancreatic adenocarcinoma. All patients were examined by perfusion CT and then underwent chemotherapy using gemcitabine. The time density curve (TDC) of each CT pixel was analyzed to calculate area under the curve (AUC) and blood flow (BF) using a mathematical algorithm based on the single-compartment model. To measure the AUC and BF of tumor (AUC_T and BF_T) and peritumoral tissue (AUC_{PTT} and BF_{PTT}), regions of interest were manually placed on the cancer and in pancreatic tissue within 10 mm of proximal pancreatic parenchyma. Survival days from the date of perfusion CT were recorded. Correlation between AUC or BF and survival days was assessed. *Results*. We found a significant correlation between AUC_{PTT} or BF_{PTT} and survival days ($P = 0.04$ or 0.0005). Higher AUC_{PTT} or BF_{PTT} values were associated with shorter survival. We found no significant correlation between AUC_T or BF_T and survival. *Conclusions*. Our results suggest that assessments of perfusion in pancreatic tissue within 10 mm of proximal pancreatic parenchyma may be useful in predicting prognosis.

1. Introduction

Pancreatic ductal adenocarcinoma (PDA) is the fourth leading cause of cancer-related death in the United States [1]. PDA is nearly universally lethal, with 5-year survival rates of less than 5% [1–3]. This poor prognosis is related to early diagnostic difficulties; the disease in more than 80% of patients at the diagnostic stage is already metastatic or locally advanced [2]. Inoperable patients typically undergo gemcitabine-based chemotherapies but with limited effectiveness [4].

Desmoplastic stroma is a histopathological characteristic of PDA [5]. The lack of adequate vasculature due to the presence of desmoplastic stroma is believed to be among the factors leading to resistance to conventional chemotherapies. The low density of vasculature causes poor perfusion, limiting the transport of the anticancer drug from vessel to tissue [6]. Tumor-associated stroma has been reported to increase chemoresistance in PDA [7]. Stromal accumulation of hyaluronan in a mouse model of PDA impaired both vascular function and drug delivery [8]. Accumulating evidence suggests the importance of tumor-associated stroma and vasculature in PDA.

As reported in previous studies, patients with pancreatic cancer may have a history of chronic pancreatitis [9]. Additionally, patients with PDA often have cancer-related pancreatitis [5]. The microstructure of the pancreas in PDA patients tends to be highly desmoplastic, resulting in reduced tissue perfusion. However, recent reports based on mouse PDA model indicate increased perfusion in the tissue surrounding PDA [10]. In human, Radu et al. report that cancer surrounding vasculature was changed due to development of cancer [11]. These studies suggest that perfusion in the tissue surrounding cancer sites may be related to cancer activity. This possibility suggests a need to investigate the relationship

between prognosis and perfusion in the tissue surrounding cancer. However, tissue vasculature can be ascertained only through intensive examination (e.g., of pathological specimens), a process that presents major difficulties. For these reasons, how or whether perfusion in the tissue surrounding a cancer relates to cancer activity remains poorly understood.

Recent reports indicate perfusion CT can be used to evaluate tissue vasculature, thereby allowing noninvasive perfusion measurements. Perfusion CT is a type of dynamic CT capable of measuring tissue perfusion based on analyses of time-density curve (TDC) derived from a bolus injection of contrast material. Perfusion CT is reported to be able to obtain nonmorphological information and is valuable for diagnosis in some organs [12]. In the study described here, we applied perfusion CT to investigate the relationship between patient prognosis and perfusion in the tissue surrounding a pancreatic cancer using perfusion CT.

2. Materials and Methods

2.1. Patients. Between December 2008 and February 2011, our pilot study enrolled 17 patients with inoperable pancreatic adenocarcinoma (PDA). We obtained written informed consent from all patients, and the research protocol was approved by the corresponding institutional review boards. Patients with histologically diagnosed pancreatic adenocarcinoma judged to be inoperable metastatic or locally advanced cancer were enrolled in this study. Diagnoses of locally advanced cancer and/or metastasis were made by a single board-certificated radiologist based on CT and/or MRI findings. All patients were treated using gemcitabine. Patients demonstrating intolerance for the contrast material for dynamic CT were excluded from the study. Our medical chart recorded age, gender, survival days from the date on which perfusion CT was performed, TNM [13], and stage of cancer [14].

2.2. Perfusion CT Protocol and Analysis. All patients were examined by perfusion CT and then underwent chemotherapy using gemcitabine. We used multidetector CT (Aquilion 64, Toshiba Medical Systems, Tochigi, Japan) to perform pancreatic perfusion CT [15]. The scanning tube voltage and current were 80 kVp and 40 mA, respectively, resulting in radiation exposures of 60–100 mGy (CTDIvol) [16]. For initial localization of the tumor, a CT study of the abdomen was obtained without contrast material enhancement during a breath hold at the end of expiration; then the CT perfusion examination of the selected area was performed in a single breath hold at end expiration. A supervising radiologist identified the tumor and then placed the predefined scan volume in the z-axis to cover the lesion for the CT perfusion study. We referred to other image data sets (e.g., US and MRI) for patients for whom such data sets existed to help identify cancer sites. To reduce respiratory artifacts, a belt over the abdomen was used and patients were instructed to breathe gently during the scan acquisition.

Stationary CT scans of four slices were acquired every 0.5 seconds over a period of 54 seconds following intravenous bolus injections of 40 mL of contrast material (Iomeprol 350 mg/mL (molecular weight, 777 kDa)) at 4 mL/second. Perfusion CT scan began 3 seconds after the start of injection. We injected iodinate contrast material through a 20-gauge intravenous cannula, followed by injection of 50 mL of saline solution, in a right cubital vein. The TDC of each CT pixel was analyzed to calculate the area under the curve (AUC) and blood flow (BF) using a mathematical algorithm based on a single-compartment model [17, 18] on workstation (ziostation2, Ziosoft, Tokyo, Japan) (Figures 1(a)–1(c)) [19].

After all of the images were loaded on a dedicated work station, the tumor was defined. TDC of the arterial input was measured by placing a circular region of interest (ROI) within the aorta on a selected image. The arterial TDC was derived automatically by the software. The AUC and BF of tumor (AUC_T and BF_T) and peritumoral tissue (AUC_{PTT} and BF_{PTT}) were obtained within a freehand ROI drawn both over the tumor itself and over pancreatic tissue within 10 mm of the juxtaposed proximal pancreatic parenchyma. We drew the largest possible single ROI that could be drawn around each tumor and peripancreatic tissue while still excluding necrosis, calcifications, and cystic or any hemorrhagic areas. The perfusion values were obtained from the parametric maps generated with the software package. Image analysis was performed in consensus by single radiologist (with 11-year experience in abdominal perfusion CT).

2.3. Statistical Analysis. We recorded survival days from the date of perfusion CT by chart review and assessed the correlation between AUC or BF and survival days by Spearman's rank correlation test. Data is presented as median (range); P values of less than 0.05 were deemed significant. The software used for statistical analysis was JMP (version 9.01, SAS Institute, NC).

3. Results

3.1. Patients. Between December 2008 and February 2011, our pilot study enrolled 17 patients with inoperable pancreatic adenocarcinoma (PDA). Of these patients, 12 (70.6%) were male and 5 (29.4%) were female. The median age was 63 (36–78). Median survival days from the date on which perfusion CT was performed were 298 days (57–914) (Table 1). According to TNM classification, patients with T4 (tumor involves celiac axis or superior mesenteric artery) and T3 (tumor extends beyond pancreas but no celiac or superior mesenteric artery involvement) [13] numbered 14 (82.4%) and 3 (17.6%), respectively. According to the Japanese classification, 8 patients were stage IVa (locally advanced cancer) and 9 patients were stage IVb (metastatic cancer) [14]. All patients were treated with gemcitabine.

3.2. Perfusion Data and Survival Days. We investigated area size, BF, and AUC of TDC in tumors and peritumoral tissue (Table 2). Area size was measured using the ROI on a workstation. We also used this ROI to measure BF and AUC. The area size of pancreatic tumor area and peritumoral area (average ± SD), respectively, were 17.7 ± 24.1 (cm^2) and 1.9 ± 1.1 (cm^2). BF_{PTT}, AUC_{PTT}, BF_T, and AUC_T, respectively, were

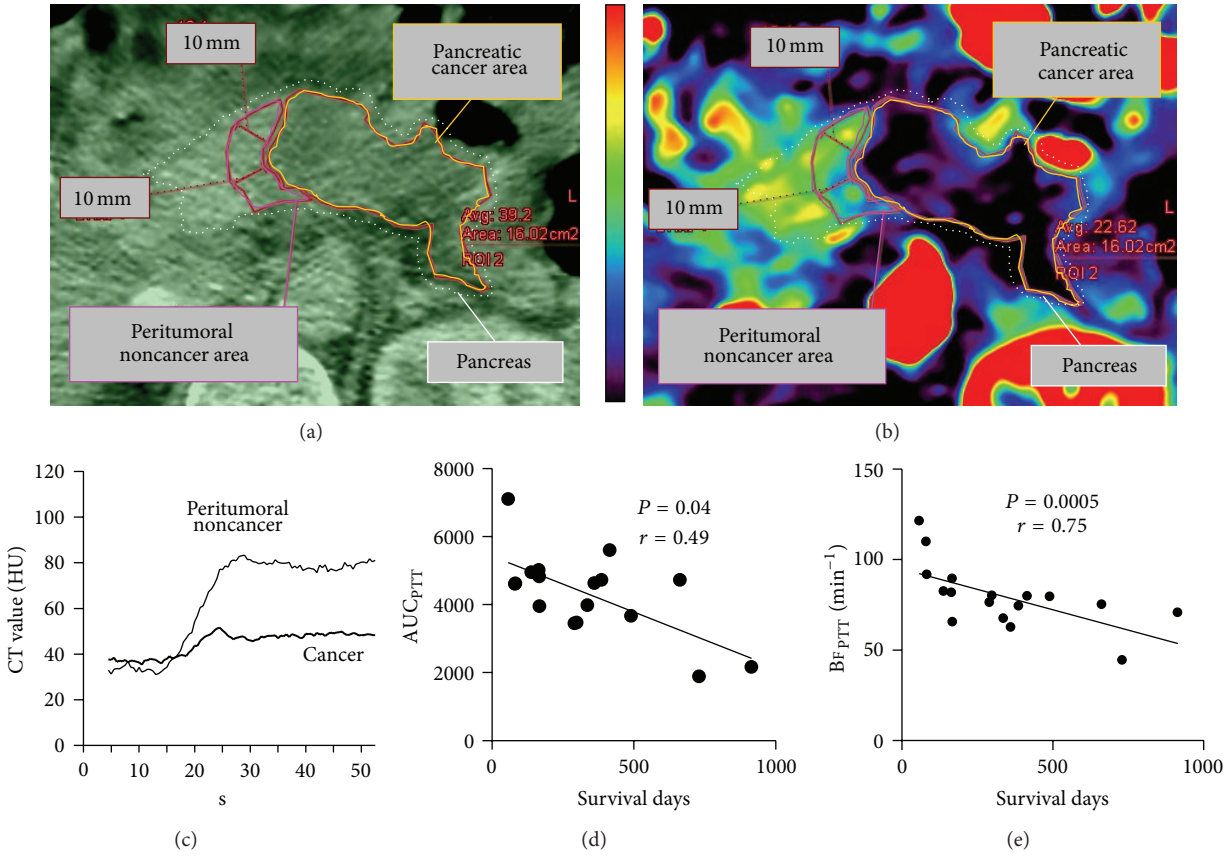

Figure 1: Analysis of pancreatic perfusion image. We analyzed the CT image dataset (of which Panel (a) is an excerpt) to obtain Panel (b). Panels (a) and (b) are magnified by the same factor. Panel (b) is a perfusion image of pancreatic blood flow (BF). Pancreatic BF is indicated by the scale on the left. Colors shift from black to red with increasing BF. The pancreatic regions of interest (ROIs) in Panels (a) and (b) have the same size and location. Panel (c) shows time-density curves for peritumoral noncancer (PTT) and cancer (T) sites for Panels (a) and (b). Panels (d) and (e) show the relationship between pancreatic AUC_{PTT} or BF_{PTT} and survival days, respectively.

Table 1: Background information for patients enrolled.

Number	Sex (M/F)	Age (age)	Survival days from date PCT performed	TNM	Stage
1	M	78	57	T4N2M1	IVb
2	M	61	298	T4N0M0	IVa
3	M	59	360	T4N3M1	IVb
4	F	78	80	T3N1M1	IVb
5	M	36	167	T3N0M1	IVb
6	F	63	138	T4N2M0	IVb
7	F	65	662	T4N1M0	IVa
8	M	61	82	T4N0M1	IVb
9	M	49	290	T4N0M0	IVa
10	M	55	166	T4N0M1	IVb
11	F	67	386	T4N0M0	IVa
12	M	64	914	T4N1M0	IVa
13	M	66	415	T4N0M0	IVa
14	M	65	730	T4N0M1	IVb
15	M	46	164	T4N0M0	IVa
16	F	66	490	T3N0M1	IVb
17	M	46	336	T4N0M0	IVa
	12/5	63.0 ± 11.1	298 ± 246		

Figures (median ± SD) for age and survival days from date perfusion CT (PCT) performed appear at the bottom of each column.

Table 2: Area, blood flow, and area under curve with injection of contrast material in pancreatic tumor and peritumoral tissue.

Number	Area of pancreatic tumor (cm^2)	Area of peritumoral tissue (cm^2)	BF_{PTT} (min^{-1})	AUC_{PTT}	BF_T (min^{-1})	AUC_T
1	28.8	25.2	121.4	3511	999	1618
2	98.6	36.9	80.15	2946	4004	3337
3	7.4	12.63	62.65	2173	1376	2529
4	3.8	44.9	109.9	3706	2321	2689
5	4.0	19.15	65.6	1786	1879	2604
6	27.8	24.16	82.48	2593	2108	2256
7	3.0	36.22	75.2	3277	1682	2344
8	22.2	20.9	91.7	3791	645	3791
9	2.9	27.4	76.4	2800	1750	2988
10	19.1	18.6	89.52	3340	966	1204
11	1.6	34.47	74.35	3527	3012	2622
12	7.5	11.6	70.8	2778	386	1796
13	2.7	39.1	79.9	2763	1638	2779
14	3.7	26.3	44.4	1413	844	1258
15	16.0	23.9	81.78	3312	1959	1909
16	44.4	49.6	79.5	1931	3430	1741
17	7.3	26.9	67.5	3717	289	2537
	17.7 ± 24.1	1.9 ± 1.1	79.6 ± 17.5	2904 ± 726	28.1 ± 10.7	2353 ± 701

BF_{PTT} and BF_T, respectively, represent blood flow (BF) of peritumoral tissue (PTT) and pancreatic tumor (T) as determined by perfusion CT. AUC_{PTT} and AUC_T, respectively, represent area under curve (AUC) with bolus injection of contrast media for PTT and T. Measurement results (average ± SD) appear at bottom of each column.

79.6 ± 17.5 (min^{-1}), 2904 ± 726, 28.1 ± 10.7 (min^{-1}), and 2353 ± 701. We observed significant correlation between AUC_{PTT} or BF_{PTT} and survival days from the date on which perfusion CT was performed ($P = 0.04$ or 0.0005). Higher AUC_{PTT} or BF_{PTT} values were associated with shorter survival (Figures 1(d) and 1(e)). We found no significant correlation between BF_T or AUC_T and survival (Figures 2(a) and 2(b)).

4. Discussion

In this study, we investigated the relationship between patient prognosis and perfusion in pancreatic cancer and tissue surrounding cancer using perfusion CT. In startling finding, survival days correlated significantly with peritumoral blood flow but not with tumor blood flow.

The results suggest that prognosis is related to increased perfusion in tissue surrounding cancer. Using MR perfusion technique in animal model, Olive et al. have shown that blood flow of peripheral tissue of pancreatic cancer increased [10]. Radu et al. have reported that follicle-stimulating hormone receptor (FSHR) was selectively expressed on the surface of peritumoral vessels [11]; in their report, the authors speculate that FSHR expression may induce VEGF and VEGF receptor 2 signaling in tumor endothelial cells and thereby promote increased vascularization. Pancreatic cancer may alter peritumoral microstructures before invading normal tissue. Thus, increased peritumoral perfusion may be related to cancer activity, as we showed.

As mentioned above, higher perfusion suggests the lower presence of stroma. Reports indicate that poor tumor perfusion is among the factors leading to PDA chemoresistance [4, 10]. As previous study using perfusion MRI reported pathologically [6], the presence of a prominent stromal matrix reduces blood vessel density in PDA tissue. A previous study [10] showed that depletion of tumor associated stromal matrix, using the inhibitor of hedgehog signaling pathway through effect on Smo, increased vasculature and concentration of drug in the tumor tissue and approved prognosis. Beatty et al. also showed that depleting the tumor stroma via activated macrophages using an agonist CD40 antibody improved prognosis in a genetically engineered mouse model of PDA [20]. However, our present study found tumor blood flow unrelated to prognosis. Our evaluation accounted for only one perfusion parameter: tumor blood flow. In fact, there are several perfusion parameters, including tissue blood flow, blood volume, and permeability [21]. Park et al. report that decreased tumor permeability measured by perfusion CT is related to chemosensitivity [22]. Thus, our study leaves open the possibility that another tumoral perfusion parameter may be related to prognosis.

Our investigation presents the following potential limitations. First, while we used the patient survival days as an index of prognosis, prognosis is not necessarily equivalent to chemosensitivity; we did not assess the relationship between perfusion in the tissue surrounding cancer and response rate to gemcitabine. Second, we defined the tissue surrounding cancer as pancreatic tissue within 10 mm of the juxtaposed proximal pancreatic parenchyma. While we assumed this tissue was composed of normal pancreatic tissue, it is certainly possible that it contained a marginal zone of cancerous tissue. Third, we used the software developed by Ziosoft, but differences of perfusion parameters between software programs or their upgrades have been reported, recently [23]. Therefore,

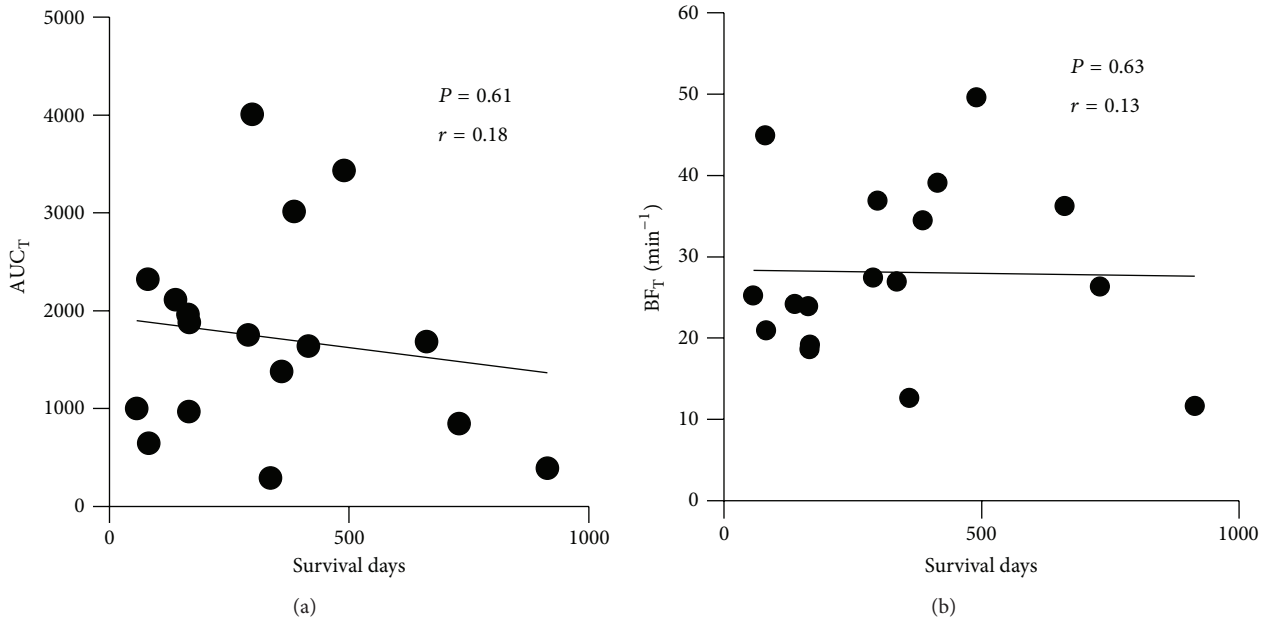

Figure 2: Relationship between AUC_T or BF_T and survival days. Panels (a) and (b) show the relationship between survival days and pancreatic AUC_T or BF_T, respectively.

our results could change by analyzing other software. Lastly, our study was a pilot study enrolling a limited number of patients.

5. Conclusion

Patient prognosis may be related to perfusion in tissue surrounding pancreatic cancer observed with perfusion CT.

Conflict of Interests

The authors declare that there is no conflict of interests regarding the publication of this paper.

References

[1] A. Jemal, R. Siegel, J. Xu, and E. Ward, "Cancer statistics, 2010," *CA Cancer Journal for Clinicians*, vol. 60, no. 5, pp. 277–300, 2010.

[2] N. Bardeesy and R. A. DePinho, "Pancreatic cancer biology and genetics," *Nature Reviews Cancer*, vol. 2, no. 12, pp. 897–909, 2002.

[3] M. Malvezzi, A. Arfé, P. Bertuccio, F. Levi, C. La Vecchia, and E. Negri, "European cancer mortality predictions for the year 2011," *Annals of Oncology*, vol. 22, no. 4, pp. 947–956, 2011.

[4] H. A. Burris III, M. J. Moore, J. Andersen et al., "Improvements in survival and clinical benefit with gemcitabine as first-line therapy for patients with advanced pancreas cancer: a randomized trial," *Journal of Clinical Oncology*, vol. 15, no. 6, pp. 2403–2413, 1997.

[5] M. Hidalgo, "Pancreatic cancer," *The New England Journal of Medicine*, vol. 362, pp. 1605–1617, 2010.

[6] M. A. Bali, T. Metens, V. Denolin et al., "Tumoral and non-tumoral pancreas: correlation between quantitative dynamic contrast-enhanced MR imaging and histopathologic parameters," *Radiology*, vol. 261, no. 2, pp. 456–466, 2011.

[7] M. Erkan, J. Kleeff, A. Gorbachevski et al., "Periostin creates a tumor-supportive microenvironment in the pancreas by sustaining fibrogenic stellate cell activity," *Gastroenterology*, vol. 132, no. 4, pp. 1447–1464, 2007.

[8] M. A. Jacobetz, D. S. Chan, A. Neesse et al., "Hyaluronan impairs vascular function and drug delivery in a mouse model of pancreatic cancer," *Gut*, vol. 62, no. 1, pp. 112–120, 2013.

[9] A. B. Lowenfels, P. Maisonneuvi, G. Cavallini et al., "Pancreatitis and the risk of pancreatic cancer," *New England Journal of Medicine*, vol. 328, no. 20, pp. 1433–1437, 1993.

[10] K. P. Olive, M. A. Jacobetz, C. J. Davidson et al., "Inhibition of Hedgehog signaling enhances delivery of chemotherapy in a mouse model of pancreatic cancer," *Science*, vol. 324, no. 5933, pp. 1457–1461, 2009.

[11] A. Radu, C. Pichon, P. Camparo et al., "Expression of follicle-stimulating hormone receptor in tumor blood vessels," *The New England Journal of Medicine*, vol. 363, no. 17, pp. 1621–1630, 2010.

[12] M. A. Mazzei, N. C. Squitieri, S. Guerrini et al., "Quantitative CT perfusion measurements in characterization of solitary pulmonary nodules: new insights and limitations," *Recenti Progressi in Medicina*, vol. 104, no. 7, pp. 430–437, 2013.

[13] F. T. Bosman, F. Carneiro, R. H. Hruban et al., *WHO Classification of Tumours of the Digestive System, Fourth Edition*, IARC Press, Lyon, France, 2010.

[14] The Japan Pancreas Society, *Classification of Pancreatic Carcinoma*, Kanehara, 3rd English edition, 2011.

[15] Y. Tsuji, H. Yamamoto, S. Yazumi, Y. Watanabe, K. Matsueda, and T. Chiba, "Perfusion computerized tomography can predict pancreatic necrosis in early stages of severe acute pancreatitis," *Clinical Gastroenterology and Hepatology*, vol. 5, no. 12, pp. 1484–1492, 2007.

[16] Y. Tsuji, K. Koizumi, H. Isoda et al., "The radiological exposure of pancreatic perfusion computed tomography," *Pancreas*, vol. 39, no. 4, pp. 541–543, 2010.

[17] R. G. Sheiman and A. Sitek, "Feasibility of measurement of pancreatic perfusion parameters with single-compartment kinetic model applied to dynamic contrast-enhanced CT images," *Radiology*, vol. 249, no. 3, pp. 878–882, 2008.

[18] K. A. Miles and M. R. Griffiths, "Perfusion CT: a worthwhile enhancement?" *The British Journal of Radiology*, vol. 76, no. 904, pp. 220–231, 2003.

[19] G. A. Zamboni, L. Bernardin, and R. Pozzi Mucelli, "Dynamic MDCT of the pancreas: is time-density curve morphology useful for the differential diagnosis of solid lesions? A preliminary report," *European Journal of Radiology*, vol. 81, no. 3, pp. e381–e385, 2012.

[20] G. L. Beatty, E. G. Chiorean, M. P. Fishman et al., "CD40 agonists alter tumor stroma and show efficacy against pancreatic carcinoma in mice and humans," *Science*, vol. 331, no. 6024, pp. 1612–1616, 2011.

[21] K. A. Miles, "Perfusion CT for the assessment of tumour vascularity: which protocol?" *British Journal of Radiology*, vol. 76, no. 1, pp. S36–S42, 2003.

[22] M.-S. Park, E. Klotz, M.-J. Kim et al., "Perfusion CT: Noninvasive surrogate marker for stratification of pancreatic cancer response to concurrent chemo—and radiation therapy," *Radiology*, vol. 250, no. 1, pp. 110–117, 2009.

[23] M. A. Mazzei, N. C. Squitieri, E. Sani et al., "Differences in perfusion ct parameter values with commercial software upgrades: a preliminary report about algorithm consistency and stability," *Acta Radiologica*, vol. 54, no. 7, pp. 805–811, 2013.

Hindawi Publishing Corporation
BioMed Research International
Volume 2014, Article ID 135013, 10 pages
http://dx.doi.org/10.1155/2014/135013

Clinical Study

CT Perfusion in the Characterisation of Renal Lesions: An Added Value to Multiphasic CT

Francesco Giuseppe Mazzei,[1] Maria Antonietta Mazzei,[2] Nevada Cioffi Squitieri,[2] Chiara Pozzessere,[2] Lorenzo Righi,[3] Alfredo Cirigliano,[2] Susanna Guerrini,[2] Domenico D'Elia,[2] Maria Raffaella Ambrosio,[4] Aurora Barone,[4] Maria Teresa del Vecchio,[5] and Luca Volterrani[2]

[1] *Department of Diagnostic Imaging, Azienda Ospedaliera Universitaria Senese, Viale Bracci 10, 53100 Siena, Italy*
[2] *Department of Medical, Surgical and Neuro Sciences, Diagnostic Imaging, University of Siena, Viale Bracci 10, 53100 Siena, Italy*
[3] *Department of Molecular and Developmental Medicine, University of Siena, Via Aldo Moro 2, 53100 Siena, Italy*
[4] *Department of Medical Biotechnologies, Section of Pathology, University of Siena, Viale Bracci 10, 53100 Siena, Italy*
[5] *Department of Medical, Surgical and Neuro Sciences, Section of Pathology, University of Siena, Viale Bracci 10, 53100 Siena, Italy*

Correspondence should be addressed to Nevada Cioffi Squitieri; nevadacioffi@gmail.com

Received 25 April 2014; Accepted 16 June 2014; Published 13 August 2014

Academic Editor: Lorenzo Preda

Objective. To prospectively evaluate if computed tomography perfusion (CTp) could be a useful tool in addition to multiphasic CT in renal lesion characterisation. *Materials and Methods.* Fifty-eight patients that were scheduled for surgical resection of a renal mass with a suspicion of renal cell carcinoma (RCC) were enrolled. Forty-one out of 58 patients underwent total or partial nephrectomy after CTp examination, and a pathological analysis was obtained for a total of 49 renal lesions. Perfusion parameters and attenuation values at multiphasic CT for both lesion and normal cortex were analysed. All the results were compared with the histological data obtained following surgery. *Results.* PS and MTT values were significantly lower in malignant lesions than in the normal cortex ($P < 0.001$ and $P = 0.011$, resp.); PS, MTT, and BF values were also statistically different between oncocytomas and malignant lesions. According to ROC analysis, the accuracy, sensitivity, and specificity to predict RCC were 95.92%, 100%, and 66.7%, respectively, for CTp whereas they were 89.80%, 93.35%, and 50%, respectively, for multiphasic CT. *Conclusion.* A significant difference between renal cortex and tumour CTp parameter values may suggest a malignant renal lesion. CTp could represent an added value to multiphasic CT in differentiating renal cells carcinoma from oncocytoma.

1. Introduction

Renal cell carcinoma (RCC) represents 3-4% of all malignancies worldwide [1]. It is classified into several types which have different features and clinical behaviours; however histologic type is one of the most important prognostic factors. Clear cell RCC, the most common type, accounting for 65–70%, has a high metastatic potential, whereas papillary RCC (10–15% of RCCs) and chromophobe RCC (5% of RCCs) have a low metastatic potential. The other malignant RCCs account for 5 to 6%. Approximately 20% of renal lesions are benign, and oncocytoma, which accounts for 5% of all renal tumours, is the most common type [2, 3]. RCC's incidence has risen over the last few years because the widespread use of cross-sectional imaging has increased the incidental detection of renal lesions, particularly those of a small size (<4 cm) [4, 5]. Although the great value of imaging for renal lesions detection has increased in recent years, the accuracy rate on preoperative characterisation of their nature remains low [6]; in particular the differential diagnosis of oncocytoma versus RCC represents a diagnostic challenge [7]. Percutaneous biopsy could be a useful tool in dubious cases, but it is an invasive approach [8, 9]. Recently, computed tomography perfusion (CTp), a functional tool which allows a quantitative

evaluation of tissue perfusion through consecutive scans acquired during contrast media injection, showed promising results in the oncologic field, even in renal lesion characterisation [10]. It is based on a time-density curve developed by software, but its reliability is still being evaluated. Furthermore the parameters used are not standardised yet, because of the availability of different software platforms and the different version upgrades of the same software, which show different perfusion measurements [11]. The identification of renal lesion type, firstly discriminating between malignant and benign, could represent an important diagnostic goal in order to choose the best management: diagnosis of RCC at an early stage means a less invasive therapeutic approach and a better prognosis, while identifying a benign lesion could avoid any unnecessary surgical intervention. By examining the previous consideration, the aim of our study was to prospectively evaluate if CTp could be a useful tool in addition to multiphasic CT in renal lesion characterisation.

2. Materials and Methods

2.1. Study Population. Our study had institutional review board approval and a written informed consent was obtained from all patients. Fifty-eight patients scheduled for surgical resection of a renal mass with a suspicion of RCC between April 2012 and December 2013 were considered for the study enrollment. All of these patients underwent renal CTp imaging and staging thoracic and abdominal CT scans. Seventeen patients were excluded as their CTp studies were not evaluable due to significant respiratory artifacts ($n = 8$), or the surgical procedure was performed in another hospital ($n = 9$). Among 58 patients included in this study, 41 (26 males, mean age of 60.76 years, range 39–86 years) underwent total or partial surgical nephrectomy at our hospital within 15.3 days (range: 1–25 days) after CTp examination, and a pathological analysis was obtained for a total of 49 renal lesions.

2.2. CT Examination. All patients were examined using a 64-detector row CT scanner (Discovery 750 HD, GE Healthcare, Milwaukee, WI, USA). To reduce respiratory artifacts, a belt over the abdomen was used and patients were instructed to breathe gently during the scan acquisition. An unenhanced CT scan of the upper abdomen covering the kidneys was performed initially to locate the renal lesion. A supervising radiologist (9 years of experience in CTp) identified the tumour and then placed the predefined scan volume (80 mm for shuttle axial technique and 40 mm for cine technique) in the z-axis to cover the lesion for the CTp study. Cine technique was used when the lesion was smaller than 20 mm. For the CTp study, 100 mL of Iomeprol (Iomeron 400; Bracco, Milan, Italy) was administered intravenously at a flow rate of 5 mL/s followed by 40 mL of saline solution at the same flow rate. The dynamic cine acquisition consisted of 8 contiguous sections, collimated to 5 mm, with temporal resolution of 1 second by using a cine-mode acquisition without table movement and with the following parameters: 100 Kv, 80 mAs, rotation time 0.5 s, and scan field of view of 50 cm, whereas it consisted of 8 contiguous sections, collimated to 5 mm, with temporal resolution of 2.8 seconds by using a shuttle-mode acquisition with table movement (21 passes) and with the following parameters: 100 Kv, 80 mAs, rotation time 0.4 s, and scan field of view of 50 cm. Total duration time was approximately 60 seconds in order to include both first-pass enhancement and delayed phase. Scanning commenced 6 seconds after the start of the contrast material injection in order to ensure the acquisition of a little nonenhanced baseline data both to allow the software to plot the enhancement change over time and to allow the radiologists to evaluate the lesion's density upon unenhanced CT at the multiphasic CT density evaluation. Immediately after completion of the CTp scans, a conventional diagnostic CT of the abdomen and thorax (CT nephrographic phase, delay of 60 to 80 s, slice thickness 2.5 mm, reconstruction interval 1 mm, collimation 40 mm, beam pitch 0.98, 140 kV, and 200–700 mA with automatic scan exposure) was performed with the intravenous administration of an additional amount of the same nonionic iodinated contrast medium mentioned previously at a rate of 4 mL/sec (up to a total amount of about 150–160 mL of iodinated contrast medium according to the patient body weight), followed by a 20 mL bolus of saline solution administered at the same rate. Finally an excretory phase CT urography was obtained after 5 to 10 minutes of the contrast media injection for 32 out of the 41 patients. All the CT scans were performed by using the adaptive statistical iterative reconstruction (ASIR, 30%) system in order to reduce the dose exposure to the patient.

2.3. Image Analysis. Image analysis was performed in consensus by a radiologist and a resident fellow in radiology (with 9 and 2 years of experience in CTp, resp.). All CTp studies were analysed by using a commercial perfusion software (Body Tumor CT Perfusion Software version 3; GE Healthcare). For the CTp analysis, a processing threshold (CT value range) between 0 and 120 Hounsfield units (HU) was utilised to optimise visualisation of the soft tissue. On transverse CT images, the slice showing the maximal transverse tumour diameter was chosen for further analysis. The arterial input was determined by placement of a circular region of interest (ROI) in the abdominal aorta, to measure the arterial input function. An arterial time-density curve (TDC) for the entire acquisition time of each study was generated automatically. In the same selected image, ROIs of the renal tumour and normal renal cortex were drawn manually (maximum 1 cm^2), lying within the structure of interest in each slice and excluding necrosis, calcifications, or cystic or any hemorrhagic areas. Mean values for four CTp parameters (permeability surface, PS; mean transit time, MTT; blood volume, BV; and blood flow, BF) were obtained and recorded for each patient. For the multiphasic evaluation, both the baseline noncontrast phase and the corticomedullary phase (CM) were evaluated on the CTp images: in particular CM phase imaging occurred 35 seconds after the threshold level of 150 HU was reached in the ROI placed in the aorta. The nephrographic phase (NG) imaging occurred 60 to 80 seconds after the threshold level of 150 HU was reached and the excretory phase imaging occurred 5 to 10 minutes

after the threshold level of 150 HU was reached. On the basis of the normal appearance of renal parenchyma, images from these protocols were classified as unenhanced if there was no contrast material administration, corticomedullary if the renal cortex but not the medulla enhanced in a ribbon-like pattern, nephrographic if the cortex and medulla enhanced uniformly, or excretory if the concentrated contrast material was excreted in the renal pelvis and ureters after the prior phases. Average tumour attenuation measurements were determined in each phase; average cortical and aorta attenuation measurements were taken in the same image in which the tumour attenuation was determined. *Absolute enhancement* was defined as the difference in mean HU between the noncontrast phase and any given contrast phase (CM, NG, or excretory); *percentage enhancement* was calculated as the mean HU in the tumour divided by the mean HU of the tumour in the noncontrast phase. *Relative enhancement to renal cortex* (or cortical-tumour relative enhancement) was defined as the difference between mean tumour enhancement and renal cortical enhancement during a given phase, whereas the cortical-tumour ratio was defined as mean tumour enhancement divided by renal cortical enhancement during any given phase; *relative enhancement to aorta* (or aorta-tumour relative enhancement) was also calculated as the difference between mean tumour enhancement and aorta enhancement during a given phase, whereas the aorta-tumour ratio was defined as mean tumour enhancement divided by aorta enhancement during any given phase. For each patient, aorta, cortical, and lesion ROIs were fixed in the same location and in the same axial slice level to subsequently enable an identical placement at the same lesion axial slice level for the multiphasic analysis by saving the ROIs within the software platform. The ROIs were reviewed by each reader for appropriate placement. The maximal diameter of each lesion was measured on axial images, and this measurement was reviewed by each reader; renal lesions were defined "hypervascular" if enhancement in the nephrographic phase was greater than or equal to that of renal cortex (in HU density) [12].

2.4. Histopathology. The surgical specimen consisted of radical nephrectomy in 31 out of 41 (75%) patients and partial nephrectomy in 10 out of 41 (25%) patients. In addition to routine samples for pathologic diagnosis, additional tissue blocks from each tumour as well as from normal renal tissue were acquired for additional histological examination and immunohistochemical staining by the pathologist. The pathologist took care to ensure sampling at a tumour level corresponding to the level at which CTp was performed. In particular on CT images the distance between the CT slice showing the maximal transverse tumour diameter and the lower or upper pole of the kidney or, in case of partial nephrectomy, the lower or upper margin of the tumour was measured. One pathologist and one radiologist (who supervised the CTp study) jointly performed the processing of all surgical specimens and reported the coordinates of the slice analysed on CTp images. All tissue specimens were fixed in a 10% buffered formalin and embedded in paraffin. The surgical specimens were sliced in the transverse plane at the level of the maximal tumour diameter, according to the distance measured on CT images. The macroscopic appearance of the transversally sliced surgical specimen was compared with the appearance of the corresponding tumour plane on transverse CT images to ensure that they were similar. From each block, 4-micron-thick sections were cut. The sections were stained with hematoxylin and eosin. All tumours were staged based on the last TNM classification system (TNM7) and the 4-tiered Fuhrman grading system was used to grade the tumours (MTdV). Quantification of microvessel density (MVD) was performed after immunostaining with a CD34 monoclonal antibody (clone QBEnd/10, ready to use) by light microscopy using the counting method introduced by Weidner et al. [13, 14] and stained with CD34 for quantification of MVD. The staining was performed on a Bond Max automated immunostainer (Leica Microsystem, Bannockburn, IL, USA) by a monoclonal antibody (predilute AP 125; ProgenBiotechnik GmbH, Maabstrasse, Heidelberg, Germany) with controls in parallel. No epitope retrieval was used. Ultravision Detection System using antipolyvalent HRP (LabVision, Fremont, CA, USA) and diaminobenzidine (DAB, Dako, Milan, Italy) as chromogen was used. Briefly, the whole slide was viewed at ×100 magnification and the area containing the maximum number of microvessels (the "hotspot" area) was identified. The precise topography of the angiogenic hotspots in carcinomas was assessed by measuring their distance from the tumour edge; hotspots within 0.5 mm were considered marginal. Then, under x400 magnification (where one field is equivalent to 0.19 mm^2) individual microvessels were counted. The number of vessels in six areas was counted and averaged as MVD. Both isolated immunoreactive endothelial cells and luminal microvascular structures were considered countable vessels. Distinct endothelial cell staining of the renal vasculature served as a positive control. Occasional immunoreactive macrophages and plasma cells were excluded, based on their morphological appearance. Assessment of MVD was completed without knowledge of any clinicopathological data and blinded to the results from CT perfusion imaging. Two pathologists (MRA and BJR) counted MVD, respectively, and mean values were calculated and recorded for each patient. Disagreements on what constituted a microvessel were resolved by consensus.

2.5. Statistical Analysis. Shapiro Wilk test was used to test the normality of variables. CTp parameters in tumour tissue and adjacent normal parenchyma were compared using Wilcoxon signed-rank test; differences in CTp parameters and multiphasic CT measurements between benign and malign tumours and between benign and malign hypervascular tumours were assessed by using the Wilcoxon-Mann-Whitney test; Kruskal-Wallis test was used to compare CTp parameters between the three malignant histologic subtypes; a P value less than 0.05 indicated a statistically significant difference. Spearman test was used to evaluate the correlation between MVD and selected CTp and multiphasic CT measurements. For this analysis, the Bonferroni correction was used and the significance level was set to 0.0071. Diagnostic accuracy of variables was measured by using receiver

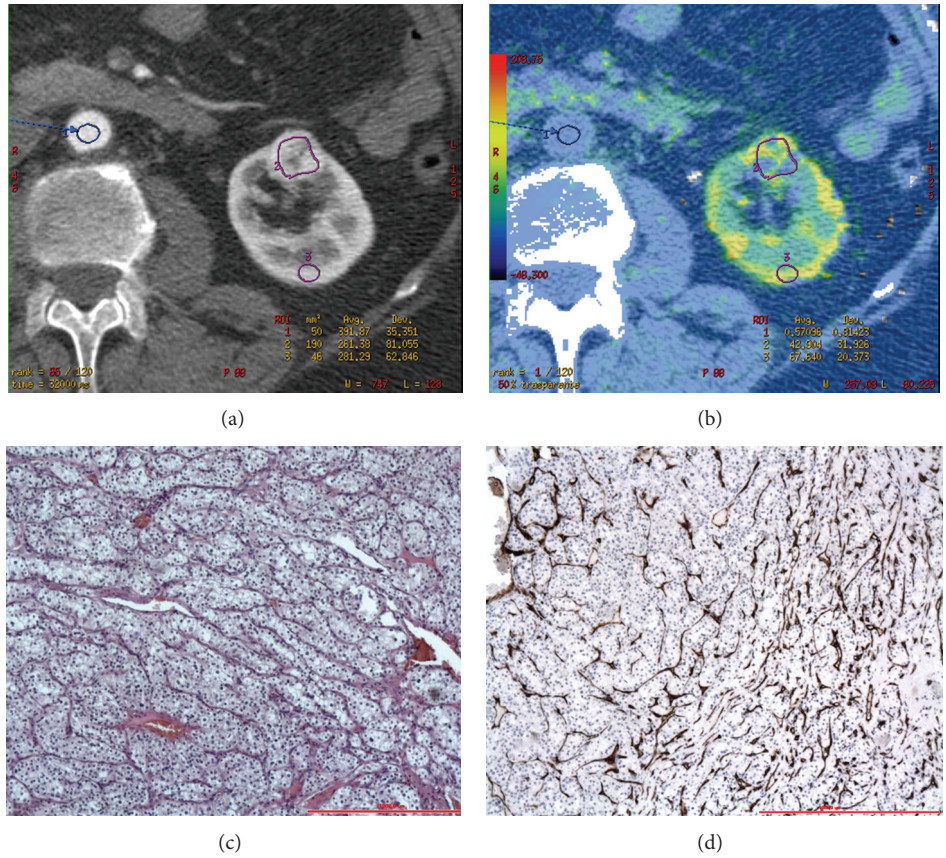

(a) (b)

(c) (d)

Figure 1: CTp of clear cell RCC: ROI 1, ROI 2, and ROI 3 were drawn in the aorta, tumour, and healthy ipsilateral renal cortex, respectively (a-b). The PS values of the tumour and normal cortex were 42.90 mL/100 g/min and 67.64 mL/100 g/min, respectively, whereas MTT values were 13.73 sec and 3.59 sec, respectively (b). Lesion size was 20 mm. Histopathology: morphology, haematoxylin, and eosin (c) and CD34 stain (d); original magnification: 50x.

operating characteristic (ROC) analysis. ROC curves were analysed to determine the cutoffs that maximise the number of correctly classified lesions. All analyses were carried out using STATA statistical software V.12.1 (StataCorp, Texas).

3. Results

All patients underwent CTp imaging without any adverse effects. Three out of 41 patients had multiple lesions; more specifically, of the 3 patients who had multiple lesions, 1 had six lesions, 1 had three lesions, and 1 had two lesions, for a total of 49 renal lesions. Of the 49 renal lesions included in this study, 27 (55%) were clear cell RCCs, 10 (21%) were chromophobe RCCs, 6 (12%) were papillary RCCs, and 6 (12%) were oncocytomas. Mean lesion diameters were 51.25 mm for clear cell RCCs, 44.2 mm for chromophobe RCCs, 26.6 mm for papillary RCCs, and 48.5 mm for oncocytomas. The pathologic tumour stage and baseline characteristics for each of the groups are presented in Table 1. Forty out of 49 lesions (82%) had been imaged also with an excretory CT scan after the CTp study (32 out of 41 patients). 25 out of 49 lesions (51%) were hypervascular at CT examination (17 clear cell RCCs, 2 chromophobe RCCs, 2 papillary RCCs, and 4 oncocytomas), 14 out of 49 lesions (29%) were hypervascular with a necrotic core (10 clear cell RCCs, 2 chromophobe RCCs, and 2 oncocytomas), and 10 (20%) were hypovascular (6 chromophobe RCCs and 4 papillary RCCs).

3.1. CTp Measurements. Mean perfusion CT parameter values (PS, MTT, BV, and BF) for the normal renal cortex and renal tumours (oncocytomas and malignant lesions) are summarised in Table 2. There were significant differences in PS ($P < 0.001$) and MTT ($P = 0.011$) between tumour and normal renal cortex in malignant lesions (clear cell carcinoma, chromophobe carcinoma, and papillary carcinoma) whereas there were no differences in any CTp parameters between lesion and normal renal cortex in oncocytomas (Figures 1 and 2). There were also significant differences in PS, MTT, and BF parameters between oncocytomas and all malignant renal lesions and in PS and MTT between oncocytomas and malignant hypervascular lesions, with or without necrosis (Table 3). Significant differences were also found in PS ($P = 0.0137$), BV ($P = 0.0106$), BF ($P = 0.0258$), and MTT ($P = 0.0084$) among the three different pathologic types of malignant lesions. The CTp parameter with the highest capacity for discriminating benign from malignant lesions, evaluated through ROC analysis, was PS (maximum accuracy

Table 1: Characteristics of patients, renal lesions, and CT examination.

Characteristics	All lesions (% or range)	Clear cell RCC (% or range)	Chromophobe RCC (% or range)	Papillary RCC (% or range)	Oncocytoma (% or range)
*N*patients	41	26*	5	5*	6
Sex					
Male	26 (63)	16 (62)	3 (60)	5 (100)	3 (50)
Female	15 (37)	10 (38)	2 (40)	0	3 (50)
Mean age	60.76 (39–86)	65.29 (39–86)	53.4 (39–60)	58.16 (42–63)	64.5 (44–80)
N lesions	49	27 (55)	10 (21)	6 (12)	6 (12)
Side					
Right	25 (51)	14 (52)	6 (60)	3 (50)	2 (33)
Left	24 (49)	13 (48)	4 (40)	3 (50)	4 (67)
Location					
UP	10 (20)	6 (22)	2 (20)	2 (33)	0
UP-MR	5 (10)	3 (11)	1 (10)	0	1 (17)
MR	15 (31)	7 (26)	4 (40)	3 (50)	1 (17)
LP-MR	7 (14)	6 (22)	0	0	1 (17)
LP	12 (25)	5 (19)	3 (30)	1 (17)	3 (49)
Mean lesion diameter (mm)	45.62 (10–128)	51.25 (20–128)	44.2 (10–110)	26.66 (17–40)	48.5 (20–116)
Pathologic tumour stage					
T1a	20 (46)	9 (33)	5 (50)	6 (100)	—
T1b	8 (19)	6 (22)	2 (20)	0	—
T2a	2 (5)	0	2 (20)	0	—
T2b	2 (5)	1 (4)	1 (10)	0	—
T3a	8 (19)	8 (30)	0	0	—
T3b	3 (6)	3 (11)	0	0	—
T3c	0	0	0	0	—
T4	0	0	0	0	—
Fuhrman grade					
1	4 (12)	3 (11)	—	1 (17)	—
2	21 (64)	17 (63)	—	4 (66)	—
3	6 (18)	5 (19)	—	1 (17)	—
4	2 (6)	2 (7)	—	0	—
MVD					
Lesion	439.20 (105–1230)	488.66 (238–1230)	412 (105–769)	256 (108–482)	444.3 (288–492)
Parenchyma	266.97 (71–537)	222.29 (80–238)	506.3 (80–537)	240.16 (71–458)	262.6 (162–322)
Perfusion1 CT study type					
Cine	13 (26)	8 (30)	1 (10)	2 (34)	2 (34)
Shuttle	36 (74)	19 (70)	9 (90)	4 (66)	4 (66)
Multiphase CT study type					
B-CM-NG-E	40 (82)	22 (81)	8 (80)	4 (66)	6 (100)
B-CM-NG	9 (18)	5 (19)	2 (20)	2 (34)	0
CT characteristics					
Hypervascular	25 (51)	17 (63)	2 (20)	2 (34)	4 (66)
H with necrosis	14 (29)	10 (37)	2 (20)	0	2 (34)
Hypovascular	10 (20)	0	6 (60)	4 (40)	0

There were 49 lesions in 41 patients; *one patient had two different histologic types of lesions: one clear cell RCC and one papillary RCC. Oncocytomas were not staged because the staging criteria only applied to RCCs. RCC: renal cell carcinoma; *N*: number; UP: upper pole; MR: mesorenal region; LP: lower pole; MVD: microvascular density; B: baseline phase; CM: corticomedullary phase; NG: nephrographic phase; E: excretory phase; H: hypervascular.

Table 2: Comparison among the CTp parameters: lesions versus normal cortex.

CTp parameters	MLs	NRC	*P* value	Oncocytomas	NRC	*P* value
PS	14.21	38.47	<0.001	35.98	37.74	0.6002
MTT	6.73	4.19	0.011	2.57	2.72	0.7532
BV	15.57	17.08	0.29	18.90	15.02	0.7532
BF	302.87	351.72	0.17	477.02	434.21	0.3454

MLs: malignant lesions; NRC: normal renal cortex; PS: permeability surface; MTT: mean transit time; BV: blood volume; BF: blood flow; a *P* value less than 0.05 indicated a statistically significant difference.

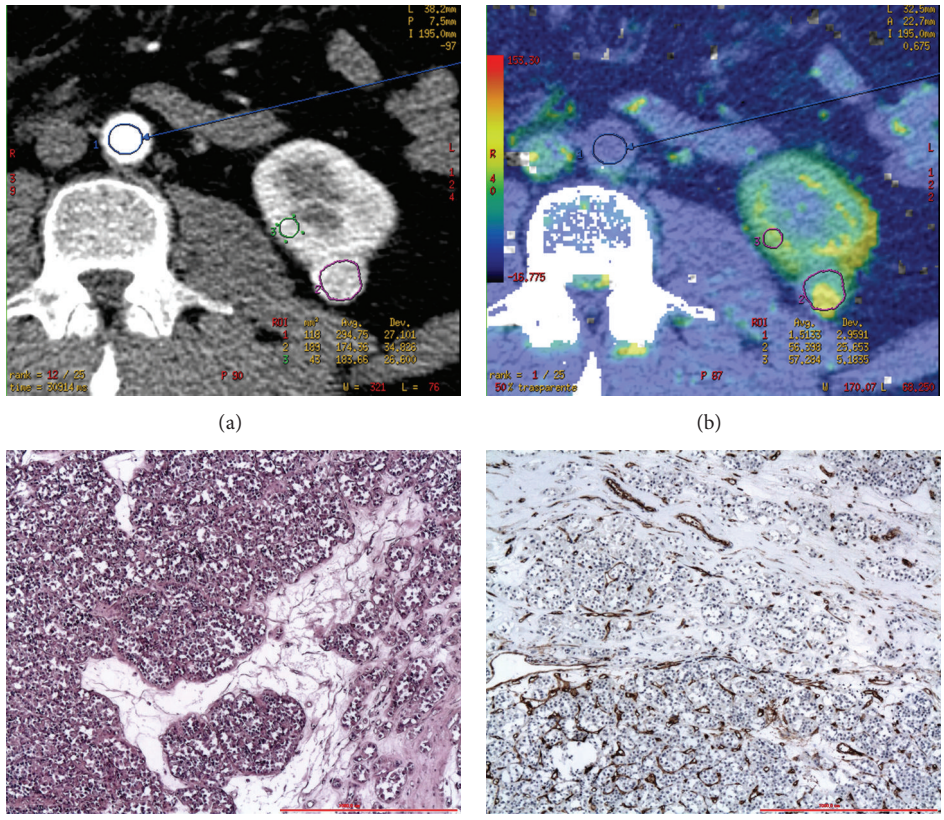

(a) (b) (c) (d)

Figure 2: CTp of oncocytoma: ROI 1, ROI 2, and ROI 3 were drawn in the aorta, tumour, and healthy ipsilateral renal cortex, respectively (a-b). The PS values of the tumour and normal cortex were 56.39 mL/100 g/min and 57.28 mL/100 g/min, respectively, whereas MTT values were 10.48 sec and 9.65 sec, respectively (b). Lesion size was 20 mm. Histopathology: morphology, haematoxylin, and eosin (c) and CD34 stain (d); original magnification: 50x.

Table 3: Comparison among the CTp parameters: malignant lesions versus oncocytomas.

CTp parameters	Oncocytomas	All MLs	*P* value	Oncocytomas	MHLs	*P* value
PS	35.98	14.21	<0.001	35.98	13.91	0.009
MTT	2.57	6.73	0.0109	2.57	6.08	0.0279
BV	18.90	15.57	0.2111	18.90	17.10	0.4596
BF	477.02	302.87	0.0240	477.02	344.55	0.0868

MLs: malignant lesions; MHLs: malignant hypervascular lesions; PS: permeability surface; MTT: mean transit time; BV: blood volume; BF: blood flow; a *P* value less than 0.05 indicated a statistically significant difference.

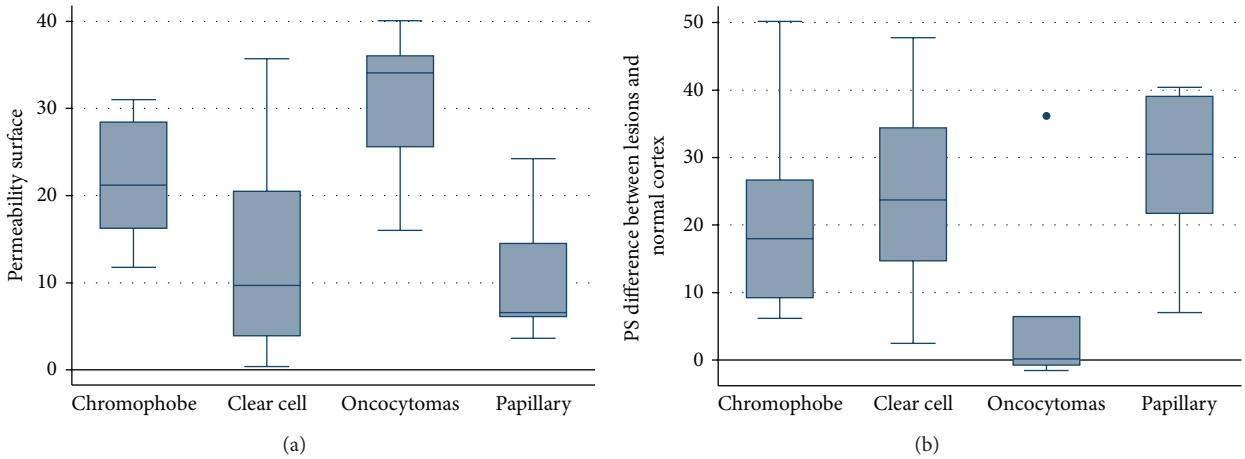

Figure 3: Box whiskers graphics: permeability surface values in different histological type of renal lesions (a); difference of permeability surface values between lesion and normal cortex in different histological type of renal lesions (b). The boxes display the interquartile range (the 25th and 75th percentile) and the median of CTp measurements for the four histologic subtypes. The whiskers display the upper and lower values within 1.5 times the interquartile range beyond the 25th and 75th percentile. Any outliers beyond those limits get their own markers (dot mark).

93.88%). The difference between the normal cortex and tumoural PS values yielded an even more accurate result; with 2.5 mL/100 g/min as a cutoff we achieved a sensitivity, specificity, and accuracy of 100%, 66.67%, and 95.92%, respectively, to predict RCCs. The results of the ROC analysis regarding the comparison between oncocytomas and all malignant lesions PS and between oncocytomas and malignant hypervascular lesions PS are illustrated in Table 4. The box and whisker plots regarding the absolute PS and the difference between normal cortex and tumoural PS values of different histologic types of tumour are presented in Figure 3.

3.2. Attenuation Measurements. Graphs and data depicting enhancement patterns are demonstrated in Figure 4. Significant differences between oncocytomas and malignant renal lesions were noted in absolute ($P = 0.0087$) and percentage ($P = 0.0061$) enhancement in the CM phase. Significant differences in absolute ($P = 0.0265$) and percentage ($P = 0.0158$) enhancement in CM phase were also noted, among hypervascular lesions and in particular among oncocytomas and malignant lesions. The multiphasic CT measure with the greatest accuracy for discriminating benign from malignant lesions was an absolute enhancement in CM phase. Using ROC analysis, the optimal cutoff value in this study was ≤160 HU enabling a sensitivity, specificity, and accuracy rate of 95.3%, 50%, and 89.8%, respectively, to predict RCCs.

3.3. MVD Analysis. The CTp parameters BF and BV measured in the tumour cross-section ROI showed a positive correlation with tumour cross-section MVD in malignant lesions ($P = 0.006$ and $P = 0.0026$, resp.) but not in oncocytomas. No significant correlations were found between other CTp or multiphasic parameters (absolute enhancement in CM, NG, or excretory phase) and the tumour cross-section MVD.

Table 4: ROC analysis.

(a) ROC analysis using difference between normal cortex and tumoural PS values

	Oncocytomas versus MHLs	Oncocytomas versus all MLs
Area under ROC curve	0.85 (C.I. 0.59–1)	0.85 (C.I. 0.60–1)
Threshold value(s)	NC PS-tumour PS >2.5	NC PS-tumour PS >2.5
Sensitivity	100%	100%
Specificity	66.67%	66.67%
Accuracy	94.87%	95.92%

(b) ROC analysis using absolute enhancement in corticomedullary phase

	Oncocytomas versus MHLs	Oncocytomas versus all MLs
Area under ROC curve	0.79 (C.I. 0.61–0.96)	0.83 (C.I. 0.69–0.97)
Threshold value(s)	<160	<160
Sensitivity	93.94%	95.35%
Specificity	50%	50%
Accuracy	87.18%	89.80%

Results of ROC curve analysis in predicting RCCs in relation to oncocytomas using difference in PS values and absolute enhancement in corticomedullary phase. PS: permeability surface; MHLs: malignant hypervascular lesions; MLs: malignant lesions; NC PS: normal cortex permeability surface.

4. Discussion

RCC represents a different spectrum of disease with different features and clinical behaviours, largely depending on the histologic type. The most aggressive type is clear cell RCC whereas papillary RCC and chromophobe RCC can both

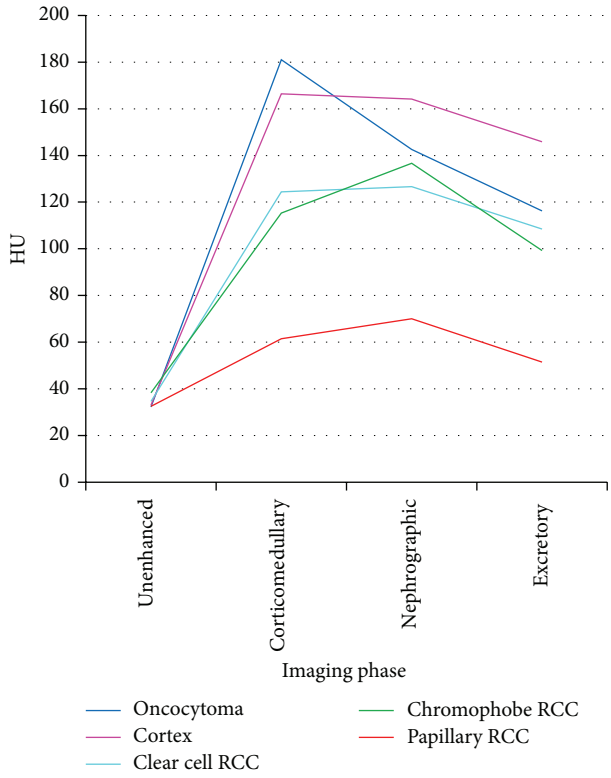

FIGURE 4: Patterns of enhancement on multiphasic imaging of 49 renal masses by tumour histology.

be considered indolent, because of their low metastatic potential. However differential diagnosis of renal masses also includes benign lesions (about 20%) and oncocytoma is the most common type [2, 3]. Over the last few years, the introduction of nephron-sparing nephrectomy has changed the approach to early stage renal cancer, allowing reduced complication rates with survival rates similar to total nephrectomy. In this sense, renal lesions characterisation should be mandatory in order to recognise a small RCC which could be treated through a partial nephrectomy rather than a wait and see approach. Moreover, differentiating benign lesions is important in order to avoid unnecessary surgery. Despite the widespread use of multimodality imaging, the characterisation of renal lesion still remains poor in some cases, particularly those of small size (<40 mm) [4–6]. In fact, while papillary RCC typically shows low contrast-enhancement at CT, oncocytoma and clear cell RCCs can have similar features and postcontrastographic behaviour, making a differential diagnosis difficult when it should be mandatory [7, 15, 16]. Several studies, using multiphase CT technique, identified differing degrees of enhancement in different postcontrast phases as the most reliable parameter to distinguish clear cell RCCs from other subtypes, including oncocytomas [16–18]. According to these studies, we also report differing degrees of contrast-enhancement between clear cell RCCs and other subtypes, including oncocytomas; however in contrast with them, in our study, as in the study of Gakis et al., oncocytoma presented a wash-in similar to renal cortex and clear cell RCCs had a lower enhancement than oncocytomas during any given phase, whereas they described a higher contrast-enhancement as a distinctive feature for discriminating clear cell RCCs in relation to oncocytomas [18–20]. Moreover, in our study, as previously reported by others, we identified that both clear cell RCCs and oncocytomas could show two different morphological features, being homogeneously hypervascular (17 and 4 cases, resp.) and hypervascular with a necrotic core (10 and 2 cases, resp.); in a few cases, even chromophobe RCCs and papillary RCCs had the same CT appearances [7, 16]. For this reason, we tested both multiphasic CT and CTp in discriminating malignant lesions in this subgroup. Furthermore still in this subgroup (hypervascular lesions), absolute percentage enhancement in CM phase was significantly higher in oncocytomas than in malignant lesions ($P = 0.02$ and $P = 0.01$, resp.), and ROC analysis showed an accuracy rate of 94% using <160HU in absolute enhancement as a cutoff for identification of malignant lesions. No significant differences in lesion-cortex ratio or in lesion-aorta ratio were identified in any given phase. To the best of our knowledge, this is the first study which has compared the same series of lesions by using both multiphasic CT and CTp. CTp allows the quantitative evaluation of a tissue perfusion whilst also optimising the acquisition protocol and has shown promising results in the oncologic field, even in RCC characterisation [10, 21, 22]. Like the recent studies, we found significant differences in PS and MTT values between malignant lesions (clear cell RCCs, papillary RCCs, and chromophobe RCCs) and the normal renal cortex ($P < 0.001$ and $P = 0.029$, resp.); however in our study BF and BV values were not significant; moreover, none of the CTp parameters evaluated in oncocytomas demonstrated significant differences from those of a normal renal cortex [10, 23, 24]. We also report significant lower values, in PS, MTT, and BF values ($P < 0.001$, $P = 0.01$, and $P = 0.02$, resp.) in malignant lesions in comparison with oncocytomas, and these results were confirmed for PS and MTT values considering only the hypervascular subgroups (those with a necrotic core versus those homogeneously hypervascular). These results could be explained by alterations of microvessel architecture in RCC, whereas oncocytomas, instead, appear to exhibit normal architecture, very close to the normal renal cortex. In fact, by evaluating a possible correlation of perfusion parameters with histological findings, particularly with microvessel density (MVD), a prognostic marker of RCC, we found a significant correlation between BF and BV and MVD ($P < 0.01$), suggesting that these CTp parameters may reflect blood vessels and then neoangiogenesis of RCCs, as also suggested by previous studies [10, 24]. At ROC curve analysis, the difference between normal cortex and tumoural PS values yielded the best result with a cutoff greater than 2.5 mL/100 g/min with a sensitivity, specificity, and accuracy of 100%, 66.67%, and 95.92%, respectively, to predict RCCs. No increased accuracy rate was obtained by considering both multiphase CT and CTp analysis. Previous studies tried to describe and differentiate the renal lesions according to the morphological criteria alone, which is often possible in large lesions, but which can be difficult for small lesions, or according to different multiphasic enhancement patterns upon CT

examination, or using CTp parameters alone [10, 16–20]. One of the unique elements of our study is that it is the first which considers two different CT techniques in the evaluation of the same series of renal tumours; however it has some limitations. Firstly, the number of renal lesions is low (49 lesions), and the subgroup of benign lesions included is relatively small (6 lesions, 12%). This could explain the low sensitivity and specificity rates obtained by ROC analysis in both multiphasic CT and CTp analyses, respectively. Increasing the case history could strengthen the results. Furthermore some common renal lesions, like angiomyolipoma with minimal fat, are not represented in our case population. Secondly, only 49% of the lesions are small renal lesions (<40 mm), which are those with uncertain management: some authors, in fact, claimed that a followup with an active surveillance instead of surgical excision should be considered in these cases, in particular if old age, decreased life expectancy, or extensive comorbidities are associated [25]. Furthermore papillary RCCs are significantly smaller than other tumours and this could influence the vascularisation patterns, even if several studies reported similar enhancement patterns for both small and large papillary RCCs [26]. Finally the CTp showed some limitations. Patients compliance is needed; in our experience 8 patients were excluded because of respiratory artifacts; moreover, it is not standardised yet, depending on several factors including the hardware platform and software algorithm [11, 27].

5. Conclusion

This study, even with the limitations just considered, showed the feasibility of CTp in discriminating between renal cell carcinoma and oncocytoma, which can be an aid in management of renal lesions. In particular we would like to state not only a standard cutoff for CTp analysis, but also a significant difference between renal cortex and tumour CTp parameter values that may suggest a malignant lesion. In an era with increased interest in active surveillance, future studies will determine whether adding CTp measurements could further refine our predictive ability in the characterisation of renal masses.

Conflict of Interests

The authors declare that there is no conflict of interests.

Acknowledgments

The authors thank Ms. Julia Hassall for reviewing the English language of the paper. The paper was printed through an educational grant by General Electric Healthcare.

References

[1] R. Siegel, D. Naishadham, and A. Jemal, "Cancer statistics, 2013," *CA Cancer Journal for Clinicians*, vol. 63, no. 1, pp. 11–30, 2013.

[2] G. Kovacs, M. Akhtar, B. J. Beckwith et al., "The Heidelberg classification of renal cell tumours," *The Journal of Pathology*, vol. 183, no. 2, pp. 131–133, 1997.

[3] N. Kuroda and A. Tanaka, "Recent classification of renal epithelial tumors," *Medical Molecular Morphology*, vol. 47, no. 2, pp. 68–75, 2014.

[4] A. Jemal, F. Bray, M. M. Center, J. Ferlay, E. Ward, and D. Forman, "Global cancer statistics," *CA: A Cancer Journal for Clinicians*, vol. 61, no. 2, pp. 69–90, 2011.

[5] I. S. Gill, M. Aron, D. A. Gervais, and M. A. Jewett, "Clinical practice: small renal mass," *The New England Journal of Medicine*, vol. 362, pp. 624–634, 2010.

[6] C. B. Dechet, H. Zincke, T. J. Sebo et al., "Prospective analysis of computerized tomography and needle biopsy with permanent sectioning to determine the nature of solid renal masses in adults," *Journal of Urology*, vol. 169, no. 1, pp. 71–74, 2003.

[7] S. Choudhary, A. Rajesh, N. J. Mayer, K. A. Mulcahy, and A. Haroon, "Renal oncocytoma: CT features cannot reliably distinguish oncocytoma from other renal neoplasms," *Clinical Radiology*, vol. 64, no. 5, pp. 517–522, 2009.

[8] K. E. Maturen, H. V. Nghiem, E. M. Caoili, E. G. Higgins, J. S. Wolf Jr., and D. P. Wood Jr., "Renal mass core biopsy: accuracy and impact on clinical management," *The American Journal of Roentgenology*, vol. 188, no. 2, pp. 563–570, 2007.

[9] V. A. Sahni and S. G. Silverman, "Biopsy of renal masses: when and why," *Cancer Imaging*, vol. 9, pp. 44–55, 2009.

[10] C. Chen, Q. Liu, Q. Hao et al., "Study of 320-slice dynamic volume CT perfusion in different pathologic types of kidney tumor: preliminary results," *PLoS ONE*, vol. 9, no. 1, Article ID e85522, 2014.

[11] M. A. Mazzei, N. C. Squitieri, E. Sani et al., "Differences in perfusion CT parameter values with commercial software upgrades: a preliminary report about algorithm consistency and stability," *Acta Radiologica*, vol. 54, pp. 805–811, 2013.

[12] M. Scialpi, A. di Maggio, M. Midiri, A. Loperfido, G. Angelelli, and A. Rotondo, "Small renal masses: assessment of lesion characterization and vascularity on dynamic contrast-enhanced MR imaging with fat suppression," *The American Journal of Roentgenology*, vol. 175, no. 3, pp. 751–757, 2000.

[13] N. Weidner, J. P. Semple, W. R. Welch, and J. Folkman, "Tumor angiogenesis and metastasis—correlation in invasive breast carcinoma," *The New England Journal of Medicine*, vol. 324, no. 1, pp. 1–8, 1991.

[14] N. Weidner, J. Folkman, F. Pozza et al., "Tumor angiogenesis: a new significant and independent prognostic indicator in early-stage breast carcinoma," *Journal of the National Cancer Institute*, vol. 84, no. 24, pp. 1875–1887, 1992.

[15] S. R. Prasad, P. A. Humphrey, J. R. Catena et al., "Common and uncommon histologic subtypes of renal cell carcinoma: imaging spectrum with pathologic correlation," *Radiographics*, vol. 26, pp. 1795–1806, 2006.

[16] J. Zhang, R. A. Lefkowitz, N. M. Ishill et al., "Solid renal cortical tumors: differentiation with CT," *Radiology*, vol. 244, no. 2, pp. 494–504, 2007.

[17] J. R. Young, D. Margolis, S. Sauk, A. J. Pantuck, J. Sayre, and S. S. Raman, "Clear cell renal cell carcinoma: discrimination from other renal cell carcinoma subtypes and oncocytoma at multiphasic multidetector CT," *Radiology*, vol. 267, no. 2, pp. 444–453, 2013.

[18] P. M. Pierorazio, E. S. Hyams, S. Tsai et al., "Multiphasic enhancement patterns of small renal masses (≤4 cm) on preoperative computed tomography: Utility for distinguishing subtypes of renal cell carcinoma, angiomyolipoma, and oncocytoma," *Urology*, vol. 81, no. 6, pp. 1265–1271, 2013.

[19] G. Gakis, U. Kramer, D. Schilling, S. Kruck, A. Stenzl, and H. Schlemmer, "Small renal Oncocytomas: differentiation with multiphase CT," *European Journal of Radiology*, vol. 80, no. 2, pp. 274–278, 2011.

[20] V. G. Bird, P. Kanagarajah, G. Morillo et al., "Differentiation of oncocytoma and renal cell carcinoma in small renal masses (< 4 cm): The role of 4-phase computerized tomography," *World Journal of Urology*, vol. 29, no. 6, pp. 787–792, 2011.

[21] F. G. Mazzei, L. Volterrani, S. Guerrini et al., "Reduced time CT perfusion acquisitions are sufficient to measure the permeability surface area product with a deconvolution method," *BioMed Research International*, vol. 2014, Article ID 573268, 6 pages, 2014.

[22] C. S. Reiner, R. Goetti, D. Eberli et al., "CT perfusion of renal cell carcinoma: Impact of volume coverage on quantitative analysis," *Investigative Radiology*, vol. 47, no. 1, pp. 33–40, 2012.

[23] Y. Chen, J. Zhang, J. Dai, X. Feng, H. Lu, and C. Zhou, "Angiogenesis of renal cell carcinoma: perfusion CT findings," *Abdominal Imaging*, vol. 35, no. 5, pp. 622–628, 2010.

[24] C. S. Reiner, M. Roessle, T. Thiesler et al., "Computed tomography perfusion imaging of renal cell carcinoma: systematic comparison with histopathological angiogenic and prognostic markers," *Investigative Radiology*, vol. 48, no. 4, pp. 183–191, 2013.

[25] E. C. Hwang, H. S. Yu, and D. D. Kwon, "Small renal masses: surgery or surveillance," *Korean Journal of Urology*, vol. 54, no. 5, pp. 283–288, 2013.

[26] R. Vikram, C. S. Ng, P. Tamboli et al., "Papillary renal cell carcinoma: radiologic-pathologic correlation and spectrum of disease," *Radiographics*, vol. 29, no. 3, pp. 741–754, 2009.

[27] L. Volterrani, M. A. Mazzei, M. Fedi, and M. Scialpi, "Computed tomography perfusion using first pass methods for lung nodule characterization: limits and implications in radiologic practice," *Investigative Radiology*, vol. 44, no. 2, p. 124, 2009.

Hindawi Publishing Corporation
BioMed Research International
Volume 2014, Article ID 573268, 6 pages
http://dx.doi.org/10.1155/2014/573268

Research Article

Reduced Time CT Perfusion Acquisitions Are Sufficient to Measure the Permeability Surface Area Product with a Deconvolution Method

Francesco Giuseppe Mazzei,[1] Luca Volterrani,[2] Susanna Guerrini,[2] Nevada Cioffi Squitieri,[2] Eleonora Sani,[3] Gloria Bettini,[2] Chiara Pozzessere,[2] and Maria Antonietta Mazzei[2]

[1] *Department of Diagnostic Imaging, Azienda Ospedaliera Universitaria Senese, Viale Bracci 10, 53100 Siena, Italy*
[2] *Department of Medical, Surgical and Neuro Sciences, Diagnostic Imaging, University of Siena, Viale Bracci 10, 53100 Siena, Italy*
[3] *Department of Physics, Osservatorio Astrofisico di Arcetri, Largo Enrico Fermi 5, 50125 Florence, Italy*

Correspondence should be addressed to Susanna Guerrini; guerrinisus@gmail.com

Received 25 April 2014; Accepted 22 June 2014; Published 12 August 2014

Academic Editor: Lorenzo Preda

Objective. To reduce the radiation dose, reduced time CT perfusion (CTp) acquisitions are tested to measure permeability surface (PS) with a deconvolution method. *Methods and Materials*. PS was calculated with repeated measurements ($n = 305$) while truncating the time density curve (TDC) at different time values in 14 CTp studies using CTp 4D software (GE Healthcare, Milwaukee, WI, US). The median acquisition time of CTp studies was 59.35 sec (range 49–92 seconds). To verify the accuracy of the deconvolution algorithm, a variation of the truncated PS within the error measurements was searched, that is, within 3 standard deviations from the mean nominal error provided by the software. The test was also performed for all the remaining CTp parameters measured. *Results*. PS maximum variability happened within 25 seconds. The PS became constant after 40 seconds for the majority of the active tumors (10/11), while for necrotic tissues it was consistent within 1% after 50 seconds. A consistent result lasted for all the observed CTp parameters, as expected from their analytical dependance. *Conclusion*. 40-second acquisition time could be an optimal compromise to obtain an accurate measurement of the PS and a reasonable dose exposure with a deconvolution method.

1. Introduction

CT perfusion (CTp) is a form of functional imaging, the use of which has increased in the past few years, thanks to the diffusion of commercial software packages that allow the analysis of dynamic data sets [1–3].

CTp requires dynamic contrast material-enhanced imaging involving intravenous injection of a contrast material bolus and sequential imaging to simultaneously monitor changes in the iodinated tracer concentration as a function of time both in the tissue of interest and in a vessel that is used as an input function to determine perfusion parameters of a given tissue, such as the blood flow (BF), the blood volume (BV), the mean transit time (MTT), and the capillary permeability surface (PS). The latter is considered a functional CT surrogate marker of tumoural angiogenesis and in this sense it can be used as an aid to carefully evaluate the response to therapy in oncologic patients, especially with the new therapies [4]. Calculation of these parameters is strictly dependent on the arterial time-density curves (TDCs) obtained by positioning a region of interest (ROI) on the input function vessel [5]. Software packages for CTp analysis typically extract the TDC and subsequently derive the perfusion parameters of given tissue by using computational models, such as a graphic analysis of a two-compartment model, "the so-called Patlak plot," or a deconvolution technique based on the time invariant linear compartmental model, which liken the relationship between the arterial, tissue, and

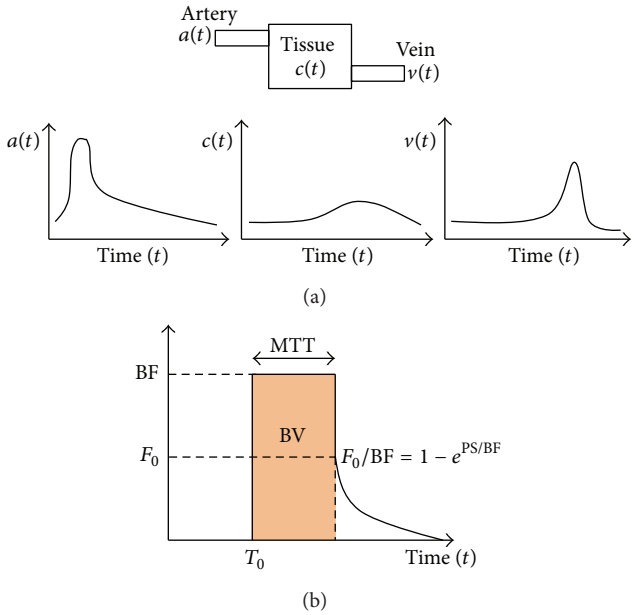

Figure 1: (a) Schematic representation of the time-density curves (TDCs), after the injection of a bolus of contrast material, in the three compartments (artery, tissue or compartment, and vein): $a(t), c(t)$, and $v(t)$. The arterial $a(t)$ and tissue $c(t)$ density curves are related to each other through a convolution (see (2)) of the artery curve with the impulse response function (IRF) shown in (b). (b) Scheme of the residual impulse response function (IRF) and perfusion parameters obtained through the deconvolution method (GE Medical Systems. User Guide. Milwaukee, WI: GE Medical Systems, 2002; 240-255). A measure of the IRF can be obtained by deconvolving the density curve $a(t)$ from $c(t)$ measured with the CTp. The CTp parameter values thus fully characterised the IRF shape as shown. In more detail, the PS is related to the diffusion coefficient of the contrast agent through the pores of the capillary endothelium into the interstitial space. In the tissue IRF, the contrast agent diffusion is related to the extraction fraction F_0/BF (or the fraction of contrast agent), which remains in the intravascular space after the initial IRF response and which then diffuses exponentially into the interstitial space. The extraction fraction is thus related to the PS in the following way: $F_0/\mathrm{BF} = 1 - \exp(\mathrm{PS}/\mathrm{BF})$, where the parameter F_0 is the blood flux measured after one mean transit time, MTT (i.e., when the contrast bolus is passed).

possibly the venous enhancement, to a mixing compartment (Figure 1) [6, 7]. The Patlak plot quantifies the PS parameter by relating the amount of tracer accumulated in the tissue ($C(t)$) to its concentration in the blood ($a(t)$):

$$c(t) = \mathrm{BV}a(t) + \mathrm{PS}\int_0^t a\left(t'\right)dt', \tag{1}$$

where the BV and PS are free parameters (intercept and slope, resp.) of a linear regression for $c(t)/a(t)$ against $\int_0^t a(t')/dt'/a(t)$. The deconvolution model (DM) computes the residual impulse response function (IRF) that relates the arterial and tissue TDCs:

$$c(t) = (a \otimes \mathrm{IRF})(t). \tag{2}$$

Once $a(t)$ and the IRF are deconvolved the perfusion parameters are defined as in Figure 2. The PS is related to the diffusion coefficient of the contrast agent through the capillary endothelium into the interstitial space. In the tissue IRF, the contrast agent diffusion is related to the extraction fraction F_0/BF, or the fraction of contrast agent, which remains in the intravascular space after the initial IRF response and which then diffuses exponentially into the interstitial space. The extraction fraction is thus related to the PS according to Figure 1(b) and (3):

$$\frac{F_0}{\mathrm{BF}} = 1 - e^{\mathrm{PS}/\mathrm{BF}}, \tag{3}$$

where the parameter F_0 is the blood flow measured after one mean transit time (i.e., when the contrast bolus is passed), $F_0 = \mathrm{IRF}(T_0 + \mathrm{MTT})$.

In both methods (1) and (2) the PS is therefore a derived quantity that requires first measuring other primary parameters. With the Patlak plot it is necessary to first measure and model the arterial and tissue TDCs and finally to perform a linear regression [8]. In order to obtain an accurate linear regression, and thus PS, it is necessary that the contrast not leave the tissue during the measurements and long radiation exposures for sufficient data for fitting [8]. The DM does not require to model $a(t)$ and $c(t)$ but only to measure their temporal trend and the tissue perfusion parameters are directly computed as a function of the height of the BF [9]. Beyond this computational advantage, the DM should be able to measure the PS with a short duration acquisition, avoiding unnecessary dose exposure to the patient [10]. In particular the method for obtaining PS involves separating contribution of the delivery of contrast medium via the supply artery from the enhancement of the extracellular compartment of the tissue of interest by performing a deconvolution of the tissue TDC with respect to that of the supply artery. It is common practice to acquire TDCs over a period of a minute or more, in part based on a reasoning that the additional data in a time-series that covers a longer interval should provide a more stable and accurate estimate of PS. During the first passage of contrast media, the large concentration gradient between blood and tissue maximises the attenuation changes mediated by a relative PS. As the blood and tissue concentrations gradually approach equilibration, the PS becomes irrelevant, and later, as excretion further lowers the blood concentration, a small reverse (tissue to blood gradient) will lead to clearance of the contrast medium from the tissue, but with little change seen between the individual timepoints. Thus, the question exists as to whether time-points beyond the first passage of contrast media contribute significantly to producing an accurate estimate of PS. Furthermore it would clearly be convenient to apply the shortest acquisition durations, anyhow without compromising the CTp parameter measurements. However the deconvolution algorithm, and thus the accuracy in the CTp estimates, depends on the number of experimental points derived for $a(t)$ and $c(t)$ curves. In other words, a given number of points are necessary to reach the algorithm convergence, and this, in turn, is a function of both the CTp acquisition duration and its temporal resolution.

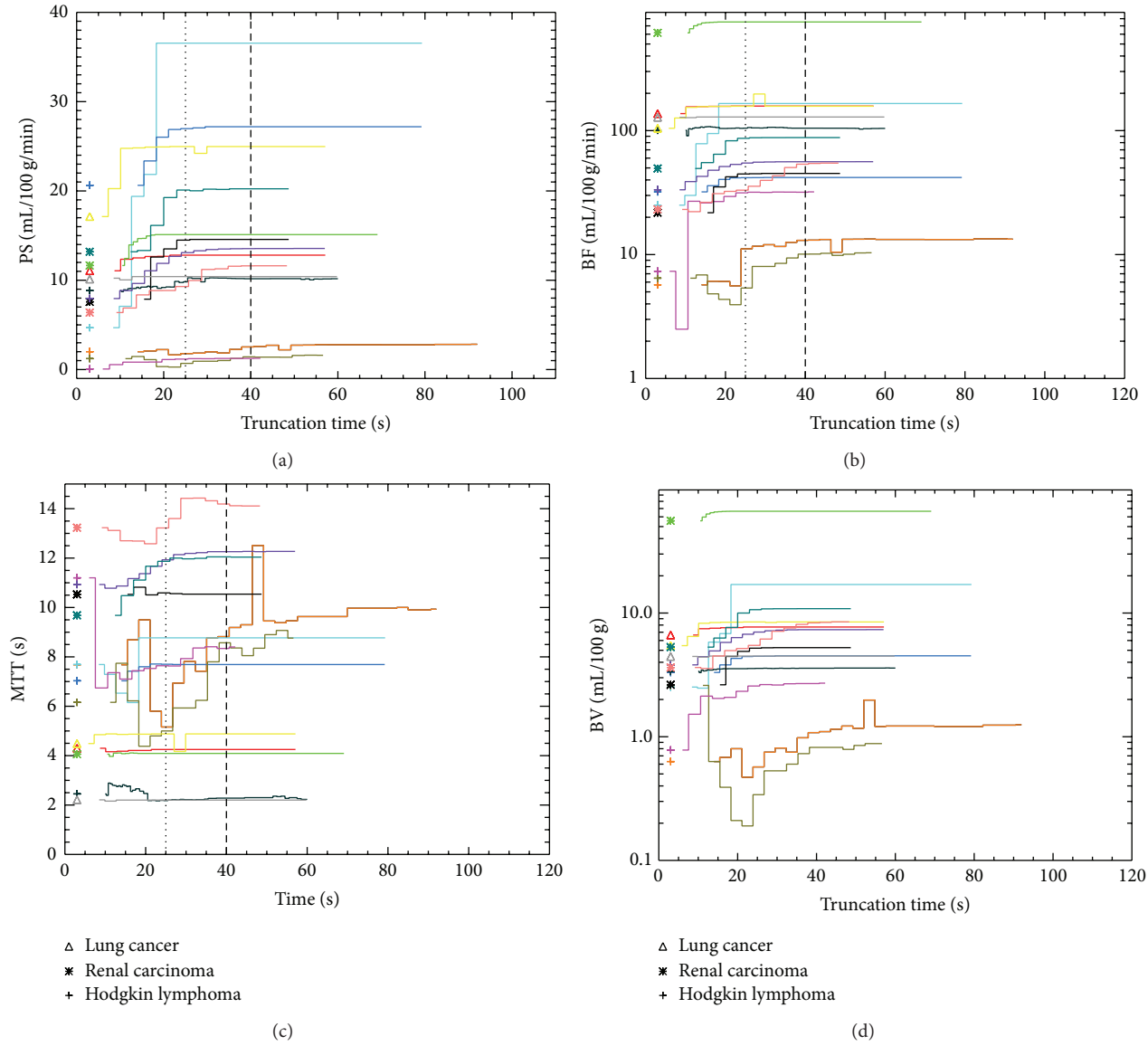

Figure 2: The trend of all the perfusion parameters measured using CT Perfusion 4D platform against the truncation time for the 14 CTp studies: the dotted vertical lines at 25 seconds and 40 seconds identify the three temporal intervals where the data are collected; variation of the truncated PS (a), BF (b), MTT (c), and BV (d) measurements.

Examining the previous consideration, in the present study we investigate this hypothesis for an unbiased sample of pathologies, in order to determine the feasibility of a short duration tumour perfusion acquisition protocol that would limit the dose exposure to the patient.

2. Materials and Methods

2.1. Patients and CTp Examination. Our study had institutional review board approval and a written informed consent was obtained from all patients. To realise our work, fourteen consecutive CTp studies, conducted in 11 patients (mean age 52.5 years; range 30–75 years; 7 males and 4 females) for lung cancer during chemotherapic treatment (LC1, LC2, and LC3), Hodgkin lymphoma (HL2, HL3, HL5, and HL7 active, i.e., at staging time with a positive PET imaging, and HL1, HL4, and HL6 inactive, i.e., in complete response [CR] after therapy according to the revised Cheson criteria, inactive residual mass with a negative PET imaging), and renal cell carcinoma (RCC1, RCC2, RCC3, and RCC4), were randomly selected from a cohort of 100 CTp studies performed in our department from January 2013 to April 2013. The CTp studies were performed with a 64-section MDCT scanner (VCT, GE Healthcare, Milwaukee, WI, USA). A supervising radiologist (9 years of experience in CTp) identified the tumour and then placed the predefined scan volume (80 mm for shuttle axial technique and 40 mm for cine technique) in the z-axis to cover the lesion for the CTp study. Cine technique was used when the lesion was smaller than 20 mm. The dynamic cine acquisition consisted of 8 contiguous sections, collimated

Table 1: Main features of the 14 CT perfusion studies selected to realise our work.

Patient	Perfusion technique	Time of acquisition (s) (mean 59.35 s)	Temporal resolution (s)	Number of measurements
HL 1 (inactive)	Shuttle	92	2.8	22
HL 2 (active)	Shuttle	56	2.8	23
HL 3 (active)	Shuttle	72	2.8	21
HL 4 (inactive)	Shuttle	57	2.8	17
HL 5 (active)	Cine	59	0.5	48
HL 6 (inactive)	Shuttle	49	2.8	13
HL 7 (active)	Shuttle	57	2.8	17
LC 1	Shuttle	57	2.8	18
LC 2	Shuttle	57	2.8	19
LC 3	Shuttle	60	2.8	19
RCC 1	Shuttle	49	2.8	12
RCC 2	Shuttle	49	2.8	13
RCC 3	Cine	69	0.5	49
RCC 4	Shuttle	48	2.8	14

CTp studies conducted for Hodgkin lymphoma (HL, $n = 7$; 3 of which were after treatment), lung cancer (LC, $n = 3$), and renal cell carcinoma (RCC, $n = 4$).

to 5 mm, with temporal resolution of 1 second by using a cine-mode acquisition without table movement and with the following parameters: 100 Kv, 80 mAs, rotation time 0.5 s, and scan field of view of 50 cm, whereas it consisted of 8 contiguous sections, collimated to 5 mm, with temporal resolution of 2.8 seconds by using a shuttle-mode acquisition with table movement (17 to 33 passes) and with the following parameters: 100 Kv, 80 mAs, rotation time 0.4 s, and scan field of view of 50 cm. The median acquisition time of CTp studies was 59.35 seconds (range 49–92 seconds). For the CTp study, 100 mL of Iomeprolo (Iomeron 400; Bracco, Milan, Italy) was administered intravenously at a flow rate of 5 mL/s followed by 40 mL of saline solution at the same flow rate. Scan acquisition commenced 5 to 10 seconds after the start of the contrast material injection, according to the lesion location, in order to ensure the acquisition of a little nonenhanced baseline images at the tumour level to allow the software to plot the enhancement change over time. Patients were allowed to breathe gently during the dynamic scan acquisition. In all patients, restraining bands were placed around the abdomen or thorax to limit respiratory movements. In Table 1, the main features of the 14 CTp studies selected to realise our work are summarised.

2.2. CTp Measurements. Image analysis was performed in consensus by 2 radiologists, who were experienced in the analysis of CTp studies (with 9 and 2 years of experience in CTp, resp.). All 14 CTp studies were analyzed by using the current version of commercial software (Body Tumour CT Perfusion software version 4D; GE Healthcare Technologies). A processing threshold between 0 and 120 Hounsfield units (HU) was utilised. The arterial input was determined by placing a circular ROI of no more than half the arterial diameter, within the aorta. A TDC for the entire acquisition time of each study was generated automatically. Tumour BF, BV, MTT, and PS were calculated with repeated measurements ($n = 305$), while truncating the TDCs at different time values in the 14 CTp studies selected. In particular perfusion parameters of the selected tissue were measured on a circular or oval ROI, larger than 70% of the minimum diameter of the tumour, which was chosen to incorporate the solid-appearing part of the target lesion. For each patient the arterial and tissue ROI as well as the start of the TDCs (taken as the last timepoint before the start of the upslope of the arterial TDC) were maintained fixed. A series of BF, BV, MTT, and PS measurements were then obtained by changing the truncation time of the TDCs, positioning the first cursor by the last preenhancement image and the second cursor at any time indicating the temporal resolution (i.e., at any 0.5 or 2.8 seconds for cine and shuttle acquisition, resp.) from that, to allow the processing of the data to the end of the TDC. In the following, we refer to the temporal position of the second cursor as the "truncation time" (Tt). This allows, for each patient, elaborating modified CTp data sets varying the duration of the dynamic phase.

2.3. Statistical Analysis. To verify the accuracy of the deconvolution algorithm, we investigated the variation of the truncated PS value against the truncation time. Since large relative errors affect any single measurement, we limited the

analysis to a direct comparison of the PS values without considering the standard deviation provided by the software across the tumour ROI for each truncation time. Then, for each patient we have collected the truncated data in three temporal intervals, chosen in order to maximise the gap in the standard deviations between an interval and its next. The analysis was also performed for all the parameters obtained (BF, MTT, and BV) using CTp 4D platform.

To evaluate whether the CTp metrics were able to distinguish between active and inactive tumours even with relatively short scanning, we performed a Kolmogorov-Smirnov (K-S) test limited to the Hodgkin lymphoma where we have 4 active (i.e., at staging time with a positive PET imaging) and 3 inactive tissues (i.e., in complete response [CR] after therapy according to the revised Cheson criteria, inactive residual mass with a negative PET imaging) (i.e., 109 versus 52 measurements, resp.).

3. Results

The mean and variation in the tumour PS, BF, MTT, and BV values obtained with DM processing for different choices of truncation time (Tt) are shown in Figure 2. The CTp 4D was able to process the data in all cases. The collection of the truncated measurements in three temporal intervals (i.e., those Tt values that maximise the gap in the standard deviations between an interval and its next) yields the cuts at 25 s and 40 s for active tumours (HL2, HL3, HL5, HL7, LC1, LC2, LC3, RCC1 RCC2, RCC3, and RCC4), while for necrotic tissues (HL1, HL4, and HL6) they are 25 s and 50 s. The relative (with respect to the mean PS, in a given interval) standard deviations are listed in Table 2. A relative error of 0.00 means that the PS remained constant within the truncation interval. Regarding the analysis of standard deviation in truncated PS, a visual inspection of Figure 2 reveals that, in the majority of the cases, the PS values rise up for 25 s with a later flattening of the trend. This suggests that the algorithm needs about 25 s to have sufficient coverage of the TDCs to perform a reliable deconvolution, after which the results remain stable. Comparing the values listed in Table 2, in most of the cases (13/14), the largest variability happens within 25 s; in 45% of the patients (HL2, LC1, LC3, RCC1, and RCC3), the PS value becomes constant, truncating the data after 25 s. The same happens in 91% (10/11) of the active tumours, after 40 s, the only exception being HL5 but with a relative error smaller than 1%. Necrotic tissues (HL1, HL4, and HL6) are characterised by noisier data and required at least 50 s to obtain a standard deviation lower than 1%. This reflects the low enhancement in their images (i.e., a poorly determined TDC $c(t)$), which is due to limited penetration of the contrast in the necrotic tissues. Comparing the 7 HL (crosses in Figure 2), the trends of active and inactive pathologies are clearly separated, as confirmed by the K-S (test probability, 1.5×10^{-32}).

Table 2: Relative PS error (%).

Patient	Tt > 0 s	Tt < 25 s	25 s ≤ Tt < 40 s	Tt > 40 s
HL 1	17.00	13.00	16.00	6.40 (1.3)
HL 2	29.00	65.00	0.00	0.00
HL 3	6.10	12.00	0.34	0.00
HL 4	36.00	61.00	24.00	7.70 (0.96)
HL 5	36.00	49.00	1.20	0.78
HL 6	5.40	3.10	1.60	1.10 (0.38)
HL 7	15.00	18.00	1.30	0.00
LC 1	3.30	5.20	0.00	0.00
LC 2	8.40	14.00	1.20	0.00
LC 3	18.00	1.50	0.00	0.00
RCC 1	14.00	24.00	0.00	0.00
RCC 2	14.00	20.00	0.45	0.00
RCC 3	4.30	73.00	0.00	0.00
RCC 4	19.00	15.00	6.00	0.00

For each patient (column 1), the standard deviation of PS over the tumour ROI/the truncation interval (expressed as a % of the PS mean) is given for each of the truncation intervals (column 2) and in subsequent truncation time (Tt) intervals (columns 3, 4, and 5). For necrotic lymphomas (i.e., HL1, HL4, and HL6) we also list in parenthesis the value shifting the last Tt cut at 50 sec.
HL: Hodgkin lymphoma; LC: lung cancer; RCC: renal cell carcinoma.

4. Discussion

A major limitation of CTp studies is the significant dose of radiation to the patient, mainly due to the long exposure times (>60 s) [10–12]. Tognolini et al. have recently demonstrated that CTp using the deconvolution method does not require a scanning time of more than 20–30 s for the BF computation in a rat tumour model [13]. To our knowledge, no studies have demonstrated the same possibility in computing CTp parameters in humans. PS parameter is a derived quantity that requires one to first measure primary parameters of CTp, such as BF, BV, and MTT. With the Patlak plot a long acquisition time seems to be necessary to achieve an accurate representation of the first pass of the injected contrast material bolus or vascular phase [$a(t)$] and a second phase, or interstitial phase [$c(t)$], to depict the dynamic characteristics of lesion enhancement and to obtain an accurate linear regression and thus a reliable PS. The DM does not require one to model $a(t)$ and $c(t)$ but only to measure their temporal trend. Beyond this computational advantage, the DM allows one to measure the PS with a short acquisition time. In fact, it is sufficient to have enough observed points in the TDCs to stabilise the deconvolution algorithm and measure primary parameters. Once the algorithm is stable, increasing the acquisition time adds little or no information about PS or for the other parameters. In our work, ~40 seconds of acquisition time was found to be sufficient to obtain a reliable IRF deconvolution and accurate PS value in the absence of those regarding necrotic tissues (e.g., checked after chemotherapy), for which slightly longer exposures (50 seconds) yield more consistent results (relative error <1%). The main limitation of this study is the absence of a direct comparison with other computation models, as the Patlak plot, which could be the subject of a further study.

Conflict of Interests

The authors declare that there is no conflict of interests regarding the publication of this paper.

Acknowledgments

The authors thank Ms. Julia Hassall for reviewing the English language. This paper was printed through an educational grant by General Electric Healthcare.

References

[1] A. R. Kambadakone and D. V. Sahani, "Body perfusion CT: technique, clinical applications, and advances," *Radiologic Clinics of North America*, vol. 47, no. 1, pp. 161–178, 2009.

[2] K. A. Miles, "Perfusion imaging with computed tomography: brain and beyond," *European Radiology*, vol. 16, supplement 7, pp. M37–M43, 2006.

[3] M. A. Mazzei, N. C. Squitieri, E. Sani et al., "Differences in perfusion CT parameter values with commercial software upgrades: a preliminary report about algorithm consistency and stability," *Acta Radiologica*, vol. 54, no. 7, pp. 805–811, 2013.

[4] K. A. Miles, "Tumour angiogenesis and its relation to contrast enhancement on computed tomography: a review," *European Journal of Radiology*, vol. 30, no. 3, pp. 198–205, 1999.

[5] M. Wintermark, W. S. Smith, N. U. Ko, M. Quist, P. Schnyder, and W. P. Dillon, "Dynamic perfusion CT: optimizing the temporal resolution and contrast volume for calculation of perfusion CT parameters in stroke patients," *American Journal of Neuroradiology*, vol. 25, no. 5, pp. 720–729, 2004.

[6] C. S. Patlak, R. G. Blasberg, and J. D. Fenstermacher, "Graphical evaluation of blood-to-brain transfer constants from multiple-time uptake data," *Journal of Cerebral Blood Flow and Metabolism*, vol. 3, no. 1, pp. 1–7, 1983.

[7] K. Godfrey, *Compartmental Models and Their Application*, Academic Press, New York, NY. USA, 1983.

[8] N. Hackstein, J. Bauer, E. W. Hauck, M. Ludwig, H. Krämer, and W. S. Rau, "Measuring single-kidney glomerular filtration rate on single-detector helical CT using a two-point Patlak plot technique in patients with increased interstitial space," *American Journal of Roentgenology*, vol. 181, no. 1, pp. 147–156, 2003.

[9] GE Medical Systems, *User Guide*, GE Medical Systems, Milwaukee, Wis, USA, 2002.

[10] M. A. Mazzei, E. Sani, S. Guerrini et al., "Reduced time CT perfusion acquisitions are sufficient to measure the permeability surface area product with a deconvolution method," *Insights into Imaging*, vol. 3, supplement 1, pp. S135–S363, 2012.

[11] M. A. Mazzei, N. Cioffi Squitieri, S. Guerrini et al., "Quantitative CT perfusion measurements in characterization of solitary pulmonary nodules: new insights and limitations," *Recenti Progressi in Medicina*, vol. 104, pp. 430–437, 2013.

[12] L. Volterrani, M. A. Mazzei, M. Fedi, and M. Scialpi, "Computed tomography perfusion using first pass methods for lung nodule characterization: limits and implications in radiologic practice," *Investigative Radiology*, vol. 44, no. 2, article 124, 2009.

[13] A. Tognolini, R. Schor-Bardach, O. S. Pianykh, C. J. Wilcox, V. Raptopoulos, and S. N. Goldberg, "Body tumor CT perfusion protocols: Optimization of acquisition scan parameters in a rat tumor model," *Radiology*, vol. 251, no. 3, pp. 712–720, 2009.

Hindawi Publishing Corporation
BioMed Research International
Volume 2014, Article ID 917150, 8 pages
http://dx.doi.org/10.1155/2014/917150

Review Article

Role of CT Perfusion in Monitoring and Prediction of Response to Therapy of Head and Neck Squamous Cell Carcinoma

Lorenzo Preda,[1] Sonia Francesca Calloni,[1,2] Marco Elvio Manlio Moscatelli,[1,2] Maria Cossu Rocca,[3] and Massimo Bellomi[1,2]

[1] *Division of Radiology, European Institute of Oncology, University of Milan, Via Ripamonti 435, 20141 Milan, Italy*
[2] *University of Milan, Via Festa del Perdono 7, 20122 Milan, Italy*
[3] *Division of Medical Oncology, European Institute of Oncology, Via Ripamonti 435, 20141 Milan, Italy*

Correspondence should be addressed to Lorenzo Preda; lorenzo.preda@ieo.it

Received 20 May 2014; Accepted 5 July 2014; Published 21 July 2014

Academic Editor: Mazzei Maria Antonietta

This review aims to summarize the technique and clinical applications of CT perfusion (CTp) of head and neck cancer. The most common pathologic type (90%) of head and neck cancer is squamous cell carcinoma (HNSCC): its diagnostic workup relies on CT and MRI, as they provide an accurate staging for the disease by determining tumour volume, assessing its extension, and detecting of lymph node metastases. Compared with conventional CT and MRI, CTp allows for obtaining measures of tumour vascular physiology and functional behaviour, and it has been demonstrated to be a feasible and useful tool in predicting local outcomes in patients undergoing radiation therapy and chemotherapy and may help monitor both treatments.

1. Introduction

Head and neck cancers represent about 5% of all malignancies newly diagnosed each year. Squamous cell carcinoma is the most common histology, accounting for about 90% of these tumours. Head and neck squamous cell carcinomas (HNSCC) arise from the mucosa of the upper aerodigestive tract and are linked by common characteristics including a male-predominant presentation and a multifactorial etiopathogenesis. Historically tobacco and alcohol assumption are the most important risk factors while human papilloma virus (HPV) exposure is an emerging cause, particularly common in the oropharynx subsite and with a better clinical outcome [1].

Most head and neck patients present in a locally advanced stage with a poor prognosis. In this setting various strategies have been tried to improve outcomes of the two main standard treatments (surgery and radiotherapy). Concomitant chemoradiation treatment has become the standard of care in the unresectable locally advanced disease and as organ preservation strategy [2]. Induction polychemotherapy (given before radiotherapy with or without concomitant chemotherapy) has been extensively investigated on the effort of improving overall survival by reducing the incidence of distant metastasis [3–5]. Despite the wide literature on this topic, this approach cannot be considered a standard of care yet and needs further data. Finally the overexpression of epidermal growth factor receptor in HNSCC is more than 90% and a correlation between this feature and a worse prognosis was found. Cetuximab, a monoclonal antibody against epidermal growth factor receptor, showed significant efficacy in locoregional control of disease and in overall survival either in the curative setting [6] or in the recurrent/metastatic HNSCC [7].

Given all these new therapeutic approaches, there remains the fact that a subset of patients obtain a major or complete response, especially from induction chemotherapy and target therapy, and we do not have predictive markers to anticipate this and to personalize the therapeutic strategy in order to improve outcomes or reduce toxicity.

In the clinical practice cross-sectional imaging integrates endoscopic evaluation of HNSCC providing information about the local invasion of the tumour into the surrounding

structures as well as the regional spread of the disease, as both have an impact on treatment and prognosis.

The traditional evaluation of response to treatment is based on modification of tumour dimensions which is unidimensional for the universally recognized Response Evaluation Criteria in Solid Tumour (RECIST) [17].

The assessment of tumour volume changes after treatment by CT may be used as an objective and reproducible technique for therapy monitoring, with good correlation with histology [18].

Furthermore CT-determined tumor volume is a strong predictor of local and locoregional outcome of laryngeal carcinoma [19].

However cross-sectional imaging techniques provide only morphologic assessment and do not tell us anything about the tumour biology.

The knowledge about the cellularity or the perfusion of a tumour may help in the differentiation of the biological behaviour during and after treatment of lesions having the same histologic type [20].

CT perfusion (CTp) has recently been used to obtain measures of tumour vascular physiology and hemodynamic. In contrast to the logarithmic relation between signal intensity and concentration of paramagnetic contrast medium of dynamic contrast enhancement MRI (DCE-MRI), the main advantage of CTp is the linear relationship between contrast concentration and attenuation in CT, which facilitates quantitative measurement of perfusion parameters [21]. Also, CTp advantages include high spatial resolution and wide availability, having the use of ionizing radiation, need of iodinated contrast medium injection, and relatively limited coverage as its major limitations.

2. CTp Technique

CTp is a theoretical tool able to quantify, through mathematical models and dedicated software, the "real" perfusion of tissues. The first technical requirement is the execution of repeated CT scans of the volume being analysed during and after intravenous administration of a fast bolus of iodinated contrast medium, to allow the study of the density variations over time [22]. The density measured by CT in the unit of volume (voxel), expressed in Hounsfield units (HU), reflects the contrast agent within the blood vessels and the contrast agent which has moved to the interstitial space due to passive diffusion [23].

The selection of the arterial input through the placement of a region of interest (ROI) on an artery allows obtaining a time-density curve of the artery, expressed in HU. This is then compared with the time-density curve of the tissue being analysed in order to distinguish between the quantity of contrast agent within the blood vessels (vascular compartment) and the quantity present in the interstitium (extra vascular/extra cellular compartment) [23].

Some studies demonstrated that the use of internal carotid artery (ICA) or external carotid artery (ECA) ipsilateral or contralateral to the tumour as the arterial input has no significant effect on CTp calculation of HNSCC [24, 25]. Tawfik et al. recommend the use of ICA because of the lower risk of partial volume effects correlated with its larger caliber and its course, almost perpendicular to the axial plane [24].

Various kinetic models can be used to calculate the distribution of contrast agent in the different compartments through the estimation of the perfusion parameters. In some of these models the analysis is performed using the single-compartment or double-compartment method which respectively describes the vascular and extravascular compartments as single or separate compartments [26].

The deconvolution method uses arterial and tissue time-density curves to calculate the impulse residue function (IRF), a theoretic tissue curve obtained assuming that the contrast agent is not diffusible and its concentration in the tissue is linearly dependent on the input arterial concentration when the blood flow is constant [26].

Most papers published about CTp in the study of HNSCC used the deconvolution based software which generates the following perfusion parameters [23, 27].

(i) *Blood flow* (BF), expressed in mL/min/100 g of tissue, is the flow rate of blood through the vasculature in tissue region. BF includes flow information from large vessels, arterioles, capillaries, and venules as well as arteriovenous shunts, which are more common in neoplastic tissue than in healthy tissue.

(ii) *Blood volume* (BV), expressed in mL/100 g of tissue, represents the volume of blood that flows within vasculature in a tissue region.

(iii) *Mean transit time* (MTT), expressed in seconds, represents the mean time the blood takes to pass through the microvasculature from the arterial to the venous end. MTT is inversely correlated to BF.

(iv) *Permeability-surface products* (PS), expressed in mL/min/100 g of tissue, measure the product between the permeability and the total surface area of capillary endothelium in a unit mass of tissue (usually 100 g of tissue). It is considered as a surrogate marker of immature leaky vessels which are more common in neoplastic tissue.

Clinical interpretation of CTp is based on a qualitative analysis and a quantitative analysis. Qualitative analysis involves the analysis of the colour maps generated by the software for each perfusion parameter. Each pixel of the CT images is attributed a colour which represents the numerical value of perfusion parameter calculated for that pixel and the colour scale is chosen by the operator in order to maximize the differences between areas having different perfusion.

Quantitative analysis involves the interpretation of numerical values of perfusion, which the software calculates for the area bounded by the ROI placed over the tumour representing the mean of the numerical values of each voxel included in the ROI [23].

Similar to CTp studies of other tumour sites [28], Petralia et al. found a good inter- and intraobserver agreement when CTp data were analysed by differently experienced readers, especially for BF, BV, and MTT [25]. The lower and more variable agreement observed for PS probably depends on

Table 1: CTp parameters obtained during and after radiotherapy and induction chemotherapy showing as valid predictions in monitoring the treatment.

Author	Cancer	Treatment	Number of patients	Predictive parameters	*P* value	Type of study
Truong et al. [8]	Primary HNSCC	Radiotherapy	15	BF	0.046	Prospective
				BV	0.053	
Petralia et al. [9]	SCCA of the upper aerodigestive tract	Induction chemotherapy	25	BF	<0.003	Prospective
				BV	<0.01	
Gandhi et al. [10]	SCCA of the upper aerodigestive tract	Induction chemotherapy	9	BV	—	Prospective
Šurlan-Popovič et al. [11]	Advanced SCCA of oral cavity, oropharynx, hypopharynx	Chemoradiotherapy	20	BV	0.01	Prospective

Notes: SCCA: squamous cell carcinoma; HNSCC: head and neck squamous cell carcinoma; BF: blood flow; and BV: blood volume.

the fact that its calculation, being reliant on prolonged scanning, is likely more affected by the cumulative effects of small motions than the other parameters which derive from first-pass scanning [25].

Over the past decade several studies investigated the role of CTp both in monitoring and predicting short-term and long-term response to organ-preserving treatments in HNSCC, though different end points were considered: disease-free survival in some case [16] and tumour volume reduction in others [9, 13, 14].

3. Monitoring during and after Treatment

In the clinical routine endoscopic examination integrated by biopsy and cross-sectional imaging represents the gold standard for therapy monitoring of HNSCC.

Few studies (Table 1) investigated the value of CT-determined tumour perfusion in this specific clinical setting in a similar way to what demonstrated for tumours located in other body regions. This is based on the theory that changes produced by radiotherapy and chemotherapeutic agents on tumour vascularity can be identified by changes in CTp measured tumour perfusion. Treatment, specifically, induced reduction of microvessels inside the tumour could be identified as a decrease of BV values while a decrease of BF could indicate a reduction of low resistance flow arteriovenous shunts in the microvasculature. The reduction of hyperpermeable capillary bed could be expressed with a decrease of PS values [29] (Figure 1).

In a small group of 9 patients treated with induction chemotherapy Gandhi et al. [10] found a positive correlation between BV pretreatment lesion values and the tumour response assessed by endoscopy. They also found that a decrease ≥ than 20% in BV values after 3 weeks of therapy is able to predict a reduction of cancer volume greater than 50%.

Petralia et al. [9] confirmed the relevance of CTp parameters in monitoring the response to the therapy. They found a significant correlation between the percent change in BV and BF values and the percent reduction of tumour volume after 3 cycles of induction chemotherapy. Their results appear to be more reliable since they use, as response quantification, tumour volume assessed by CT instead of the endoscopy standard which is an operator-dependent technique.

Serial fluctuations in perfusion parameters of HNSCC during a course or radiotherapy were prospectively evaluated by Truong et al. [8], by using CTp to provide information about the periodical changes in tumour oxygenation produced by radiotherapy. Pretreatment tumour BF was higher in patients who achieved locoregional control (LRC) compared with those with locoregional failure (LRF) (P = 0.004), consistent with the findings of Hermans et al. [12]. Furthermore, authors demonstrated that an increase in BF during the first two weeks of radiotherapy is able to predict LRC, with a decrease in both groups after 6 weeks of radiotherapy compared with the values at the baseline scanning, suggesting that a higher BF in tumour tissue at the baseline and during the early course or radiotherapy predicts a better tumour control.

Interestingly Šurlan-Popovič et al. [11], in a series of 24 patients with locally advanced HNSCC, demonstrated that the modifications of CTp parameters during the course of treatment might predict tumour response to cisplatin-based chemoradiotherapy.

In particular responders presented a significant reduction of BF values (p 0,04) after 40 Gy which was more pronounced after 70 Gy (p 0,01) and a significant reduction of BV values after 40 Gy with a plateau after 70 Gy (p 0,04). MTT and PS values showed nonsignificant modifications.

On the contrary in nonresponders BF, BV, and PS values showed a nonsignificant increase after 40 Gy.

The possible explanation given by the authors to these findings is that the dynamics in CTp parameters are mainly related to the cytotoxic effects of radiotherapy to the vascular endothelium which is more effective than the little antivascular action of cisplatin-based chemotherapy [11].

In an attempt to explain the increase of perfusion parameters values observed in nonresponders, authors hypothesized that ionizing radiation therapy may produce the upregulation of VEGF which promotes survival of endothelial cells in

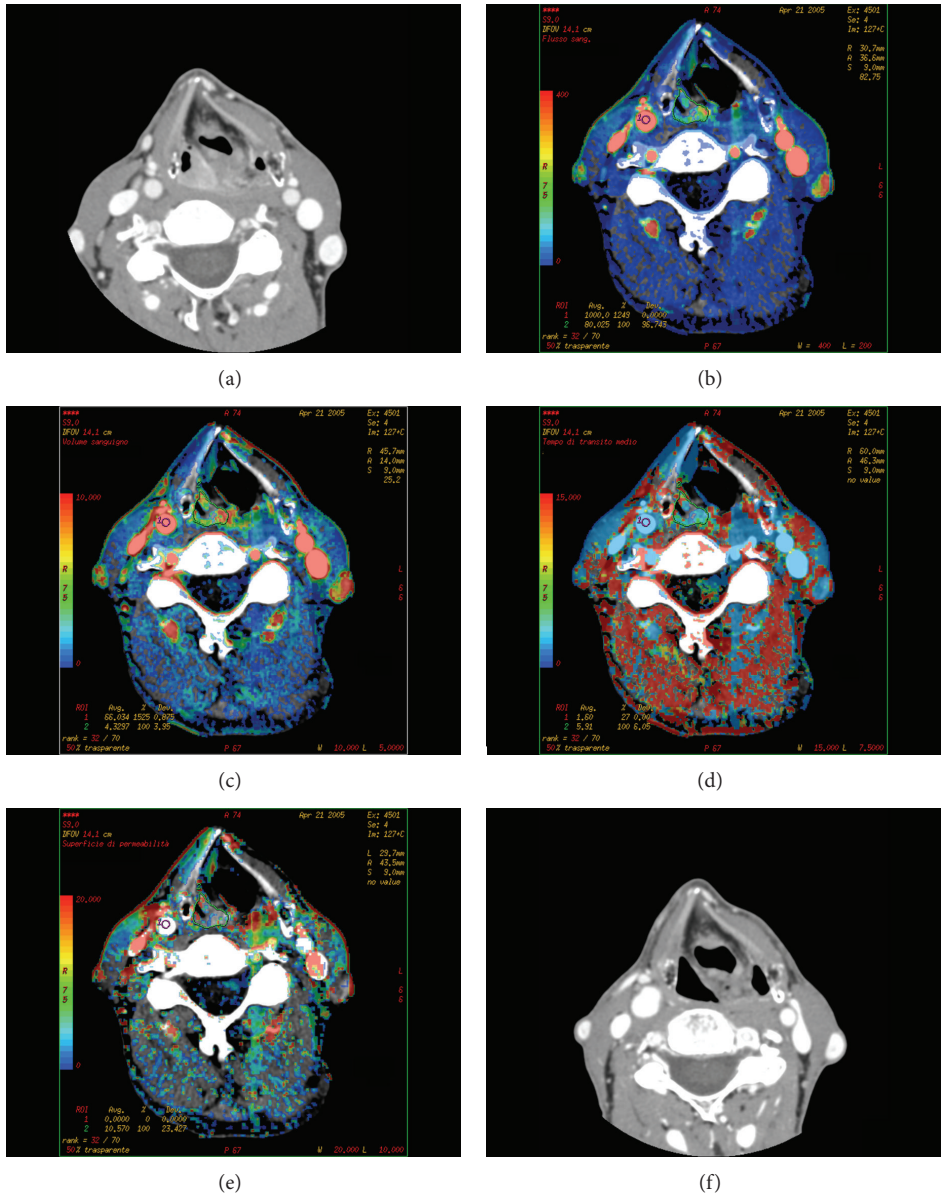

(a) (b) (c) (d) (e) (f)

Figure 1: Squamous cell carcinoma of hypopharynx in a responder patient: CT scan (a) obtained before chemotherapy shows the lesion involving the right piriform sinus. On the same section, functional maps of BF (b), BV (c), MTT (d), and PS (e) are automatically generated by the software, showing the values calculated in each pixel of the image in a color scale. CT scan obtained in the same patient after chemotherapy and radiotherapy showing a complete disappearance of the tumour (f).

residual tumour tissue and consequently radiation resistance [30].

4. Prediction of Response to Radiotherapy and Chemotherapy

The rationale of the potential role of CTp in predicting response to nonsurgical therapies is that it is substantially influenced by tissue perfusion and local oxygen delivery. The oxygen supply to a tissue is governed by its perfusion and the arterial oxygen concentration. It is conceivable that higher levels of BF and BV may correlate with better oxygen/drug delivery and therefore may predict the response to radiation therapy or chemotherapy.

Theoretically, a CTp study performed prior to the beginning of therapy could identify patients with poorly perfused tumours likely to demonstrate a bad response to chemoradiotherapy, thus allowing them to be directed to alternative treatments [29].

Thus, in recent years, some studies appeared in the literature dealing with this topic (Table 2).

In a series of 105 patients with HNSCC treated with definitive radiotherapy, some associated with adjuvant chemotherapy, Hermans et al. [12] found that CTp parameters

Table 2: Results for the prediction of response to radiotherapy and chemotherapy based on the pretreatment tumour volume and the perfusion-associated parameters.

Author	Cancer	Number of patients	Predictive parameters	P value	Type of study
Hermans et al. [12]	Primary HNSCC	105	Median perfusion value	0.01	Prospective
Zima et al. [13]	SCCA of the upper aerodigestive tract	17	BF BV	<0.03 <0.004	Prospective
Bisdas et al. [14]	Advanced oropharynx SCCA	19	BF, BV, PS, MTT	<0.001	Prospective
Petralia et al. [9]	SCCA of the upper aerodigestive tract	25	BV	0.015	
Bisdas et al. [15]	Primary SCCA of oral cavity, oropharynx, hypopharynx	21	BF, BV, MTT, PS BF_{max}, BV_{max}	<0.004 <0.001	Prospective
Bisdas et al. [16]	SCCA of the upper aerodigestive tract	84	BF, PS BF-BV mismatch	<0.000 0.01	Prospective

Notes: SCCA: squamous cell carcinoma; HNSCC: head and neck squamous cell carcinoma; BF: blood flow; BV: blood volume; PS: permeability surface area product; MTT: mean transit time; and CP: capillary permeability surface area product.

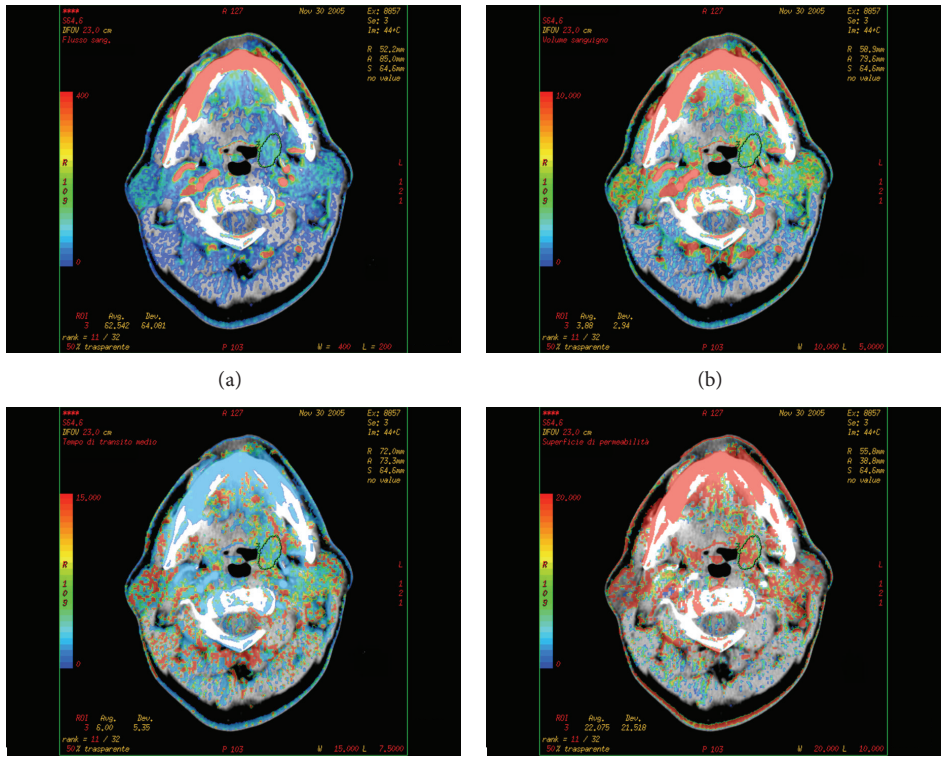

Figure 2: Squamous cell carcinoma of the oropharynx in a nonresponder patient. The functional maps of BF (a), BV (b), MTT (c), and PS (d) are automatically generated by the software, showing low BF and BV values within the lesion.

are independent predictors of local control together with T stage. In particular patients with a low perfusion pretreatment value showed a statistically significantly higher local failure rate than those with a high perfusion value ($P < 0.05$), presumably due to a more extensive degree of hypoxia in low-perfused tumour and therefore characterized by low radiosensitivity (Figure 2).

Similarly, in a study of 17 patients, Zima et al. [13] demonstrated that elevated pretreatment values of BF ($P < 0.03$) and BV ($P < 0.004$) CTp parameters showed a significant correlation with response to induction chemotherapy evaluated endoscopically.

Bisdas et al. [14] confirmed these results showing correlation between radiological response after induction

chemotherapy and CTp parameters at baseline while just a weak correlation with pretreatment tumour volume was found. With these findings CTp perfusion parameters seemed to outperform the morphologic characteristics, being significantly different ($P \leq 0.002$) between responders and nonresponders with high BF, BV, and PS and low MTT correlated with a better tumour response, presumably reflecting better tumour oxygenation. The authors concluded their paper highlighting the role of CTp as a noninvasive, inexpensive, and widely accessible diagnostic tool, able to improve the choice of organ preservation treatment regimens in order to maximize the therapeutic efficacy [14].

In the paper by Petralia et al. [9] only baseline tumour BV was significantly lower (p 0, 015) in nonresponder compared to responders to induction chemotherapy. They found a trend to correlation between baseline tumour BV and high tumor volume reduction assessed by CT [21].

Bisdas et al. [15] assessed whether CTp may predict outcome in 21 chemoradiated patient with oral cavity, oropharynx, and hypopharynx SCC after surgical excision: they applied a new analysis on the region of interest-derived CTp values, namely, the maximum BF, BV, and PS, as well as the minimum MTT values, trying to avoid the considerable intratumoral variation covered with mean values. Both mean perfusion values and BF_{max}, BV_{max}, and BS_{max} were significantly different between patients with and without tumour recurrence ($P < 0.04$). Also, the authors underline the predictive value of PS and MTT. In particular they found a relative risk of recurrence about 14 time higher in patients with lower than the median BS_{mean} values, which is apparently in contrast with the results of other studies demonstrating a significantly shorter disease-free survival in patients with high intratumoral microvessel density [31]. According to the authors these findings confirm the absence of any clear relationship between microvascular density and PS values [32]. On the other hand the predictive role of MTT values may be attributed in part to leaky tumour vessels, which lead to improved oxygenation [15].

The same authors [16], in a large series of 84 patients with advanced HNSCC who underwent CTp prior to concomitant chemoradiotherapy, found that BF and PS values were significantly higher in patients who had local failure ($P \leq 0.02$).

Furthermore a simultaneous visual evaluation of the BF and the BV parametric maps showed that the presence of a mismatch (>30% of the examined lesion extent) between the colour-encoded maps correlates with shorter life expectance ($P = 0.01$) and smaller recurrence-free survival ($P = 0.03$).

This approach is based on the rational that a considerable mismatch, more evident in locally advanced tumours, may indicate a heterogeneous pattern of vascularisation, which may lead to a cascade that influences cellular phenotypes and presents with therapy resistance [33].

5. Conclusions

All the preliminary results of previous studies show that elevated CT perfusion parameters are statistically correlated to a better response to radiotherapy and chemotherapy and prove that tissue oxygenation may also influence the spread of chemotherapy agents and a higher radiosensitivity.

BV and BF have clearly emerged as the most significative CTp parameters as they may predict response to radiation therapy and chemotherapy and may help monitor both treatments.

PS and MTT parameters are insufficiently predictive of the response compared with BV and BF: only one paper highlighted their achievable effectiveness [15].

It must be also considered that published studies considered different end points and most of them correlated their findings with short-term follow-up.

Large-scale studies examining the long-term predictive value of baseline CTp studies in patient treated both with neoadjuvant chemoradiation or chemoradiation with curative intent might help in tailoring the therapy regimen on individual basis. As an instance, the possibility to identify earlier a failed response to induction chemotherapy may help avoid this step during the therapeutic treatment plan.

Therefore, a more standardized technique is hopeful in order to achieve reproducible and comparable method across different institutions.

Future integrated applications with PET-CT findings or dual-energy CT may enable more understanding of the biologic behaviour of the tumour in vivo, making the CTp one of the potential cornerstone of biologic imaging of HNSCC.

Conflict of Interests

The authors certify that they have no affiliations with or involvement in any organization or entity with any financial interest (such as honoraria; educational grants; participation in speakers' bureaus; membership, employment, consultancies, stock ownership, or any other equity interest; and expert testimony or patent-licensing arrangements) or nonfinancial interest (such as personal or professional relationships, affiliations, knowledge, or beliefs) in the subject matter or materials discussed in this paper.

References

[1] H. S. van Monsjou, A. J. M. Balm, M. M. van den Brekel, and V. B. Wreesmann, "Oropharyngeal squamous cell carcinoma: a unique disease on the rise?" *Oral Oncology*, vol. 46, no. 11, pp. 780–785, 2010.

[2] A. A. Forastiere, H. Goepfert, and M. Maor, "Concurrent chemotherapy and radiotherapy for organ preservation in advanced laryngeal cancer," *The New England Journal of Medicine*, vol. 349, pp. 2091–2098, 2003.

[3] J. Ma, Y. Liu, X. Huang et al., "Induction chemotherapy decreases the rate of distant metastasis in patients with head and neck squamous cell carcinoma but does not improve survival or locoregional control: a meta-analysis," *Oral Oncology*, vol. 48, no. 11, pp. 1076–1084, 2012.

[4] L. J. Wirth and M. R. Posner, "Recent advances in combined modality therapy for locally advanced head and neck cancer," *Current Cancer Drug Targets*, vol. 7, no. 7, pp. 674–680, 2007.

[5] J. B. Vermorken, R. S. Herbst, X. Leon, N. Amellal, and J. Baselga, "Overview of the efficacy of cetuximab in recurrent

and/or metastatic squamous cell carcinoma of the head and neck in patients who previously failed platinum-based therapies," *Cancer*, vol. 112, no. 12, pp. 2710–2719, 2008.

[6] J. A. Bonner, P. M. Harari, J. Giralt et al., "Radiotherapy plus cetuximab for squamous-cell carcinoma of the head and neck," *The New England Journal of Medicine*, vol. 354, no. 6, pp. 567–578, 2006.

[7] J. B. Vermorken, E. Remenar, C. van Herpen et al., "Cisplatin, fluorouracil, and docetaxel in unresectable head and neck cancer," *The New England Journal of Medicine*, vol. 357, pp. 1695–1704, 2007.

[8] M. T. Truong, N. Saito, A. Ozonoff et al., "Prediction of locoregional control in head and neck squamous cell carcinoma with serial CT perfusion during radiotherapy," *The American Journal of Neuroradiology*, vol. 32, no. 7, pp. 1195–1201, 2011.

[9] G. Petralia, L. Preda, G. Giugliano et al., "Perfusion computed tomography for monitoring induction chemotherapy in patients with squamous cell carcinoma of the upper aerodigestive tract: Correlation between changes in tumor perfusion and tumor volume," *Journal of Computer Assisted Tomography*, vol. 33, no. 4, pp. 552–559, 2009.

[10] D. Gandhi, D. B. Chepeha, T. Miller et al., "Correlation between initial and early follow-up CT perfusion parameters with endoscopic tumor response in patients with advanced squamous cell carcinomas of the oropharynx treated with organ-preservation therapy," *American Journal of Neuroradiology*, vol. 27, no. 1, pp. 101–106, 2006.

[11] K. Š. Šurlan-Popovič, S. Bisdas, Z. Rumboldt, T. S. Koh, and P. Strojan, "Changes in perfusion CT of advanced squamous cell carcinoma of the head and neck treated during the course of concomitant chemoradiotherapy," *American Journal of Neuroradiology*, vol. 31, no. 3, pp. 570–575, 2010.

[12] R. Hermans, M. Meijerink, W. van den Bogaert, A. Rijnders, C. Weltens, and P. Lambin, "Tumor perfusion rate determined noninvasively by dynamic computed tomography predicts outcome in head-and-neck cancer after radiotherapy," *International Journal of Radiation Oncology Biology Physics*, vol. 57, no. 5, pp. 1351–1356, 2003.

[13] A. Zima, R. Carlos, D. Gandhi, I. Case, T. Teknos, and S. K. Mukherji, "Can pretreatment CT perfusion predict response of advanced squamous cell carcinoma of the upper aerodigestive tract treated with induction chemotherapy?," *American Journal of Neuroradiology*, vol. 28, no. 2, pp. 328–334, 2007.

[14] S. Bisdas, Z. Rumboldt, J. Wagenblast et al., "Response and progression-free survival in oropharynx squamous cell carcinoma assessed by pretreatment perfusion CT: comparison with tumor volume measurements," *The American Journal of Neuroradiology*, vol. 30, no. 4, pp. 793–799, 2009.

[15] S. Bisdas, S. A. Nguyen, S. K. Anand, G. Glavina, T. Day, and Z. Rumboldt, "Outcome prediction chemoradiation of in the oral cavity, oropharynx, and hypopharynx: use of baseline perfusion CT microcirculatory parameters vs. tumor volume," *International Journal of Radiation Oncology∗ Biology∗ Physics*, vol. 73, no. 5, pp. 1313–1318, 2009.

[16] S. Bisdas, Z. Rumboldt, K. Surlan-Popovic et al., "Perfusion CT in squamous cell carcinoma of the upper aerodigestive tract: long-term predictive value of baseline perfusion CT measurements," *American Journal of Neuroradiology*, vol. 31, no. 3, pp. 576–581, 2010.

[17] P. Therasse, S. G. Arbuck, E. A. Eisenhauer et al., "New guidelines to evaluate the response to treatment in solid tumors. European Organization for Research and Treatment of Cancer, National Cancer Institute of the United States, National Cancer Institute of Canada," *Journal of the National Cancer Institute*, vol. 92, no. 3, pp. 205–216, 2000.

[18] L. Preda, E. Lovati, F. Chiesa et al., "Measurement by multidetector CT scan of the volume of hypopharyngeal and laryngeal tumours: accuracy and reproducibility," *European Radiology*, vol. 17, no. 8, pp. 2096–2102, 2007.

[19] R. Hermans, K. Op de Beeck, W. van den Bogaert et al., "The relation of CT-determined tumor parameters and local and regional outcome of tonsillar cancer after definitive radiation treatment," *International Journal of Radiation Oncology, Biology, Physics*, vol. 50, no. 1, pp. 37–45, 2001.

[20] A. Srinivasan, S. Mohan, and S. K. Mukherji, "Biologic imaging of head and neck cancer: the present and the future," *American Journal of Neuroradiology*, vol. 33, no. 4, pp. 586–594, 2012.

[21] A. M. Tawfik, A. A. Razek, L. G. Elsorogy et al., "Perfusion CT of head and neck cancer," *European Journal of Radiology*, vol. 83, no. 3, pp. 537–544, 2014.

[22] G. Petralia, L. Preda, G. D'Andrea et al., "CT perfusion in solid-body tumours. Part I: technical issues," *Radiologia Medica*, vol. 115, no. 6, pp. 843–857, 2010.

[23] G. Petralia, L. Bonello, S. Viotti, L. Preda, G. D'Andrea, and M. Bellomi, "CT perfusion in oncology: how to do it," *Cancer Imaging*, vol. 10, no. 1, pp. 8–19, 2010.

[24] A. M. Tawfik, A. A. Abdel Razek, L. G. Elsorogy et al., "Perfusion CT of head and neck cancer: effect of arterial input selection," *American Journal of Roentgenology*, vol. 196, no. 6, pp. 1374–1380, 2011.

[25] G. Petralia, L. Preda, S. Raimondi et al., "Intra and interobserver agreement and impact of arterial input selection in perfusion CT measurements performed in squamous cell carcinoma of the upper aerodigestive tract," *The American Journal of Neuroradiology*, vol. 30, no. 6, pp. 1107–1115, 2009.

[26] K. A. Miles, "Perfusion CT for the assessment of tumour vascularity: which protocol?" *British Journal of Radiology*, vol. 76, no. 1, pp. S36–S42, 2003.

[27] A. R. Kambadakone and D. V. Sahani, "Body perfusion CT: technique, clinical applications, and advances," *Radiologic Clinics of North America*, vol. 47, no. 1, pp. 161–178, 2009.

[28] V. Goh, S. Halligan, A. Gharpuray, D. Wellsted, J. Sundin, and C. I. Bartram, "Quantitative assessment of colorectal cancer tumor vascular parameters by using perfusion CT: influence of tumor region of interest," *Radiology*, vol. 247, no. 3, pp. 726–732, 2008.

[29] M. Bellomi, S. Viotti, L. Preda, G. D'Andrea, L. Bonello, and G. Petralia, "Perfusion CT in solid body-tumours. Part II: clinical applications and future development," *La Radiologia Medica*, vol. 115, no. 6, pp. 858–874, 2010.

[30] V. K. Gupta, N. T. Jaskowiak, M. A. Beckett et al., "Vascular endothelial growth factor enhances endothelial cell survival and tumor radioresistance," *Cancer Journal*, vol. 8, no. 1, pp. 47–54, 2002.

[31] T. Martone, P. Rosso, R. Albera et al., "Prognostic relevance of CD105+ microvessel density in HNSCC patient outcome," *Oral Oncology*, vol. 41, no. 2, pp. 147–155, 2005.

[32] K. P. Claffey, L. F. Brown, L. F. Del Aguila et al., "Expression of vascular permeability factor/vascular endothelial growth factor by melanoma cells increases tumor growth, angiogenesis, and experimental metastasis," *Cancer Research*, vol. 56, no. 1, pp. 172–181, 1996.

[33] H. Axelson, E. Fredlund, M. Ovenberger, G. Landberg, and S. Påhlman, "Hypoxia-induced dedifferentiation of tumor cells–a mechanism behind heterogeneity and aggressiveness of solid tumors," *Seminars in Cell and Developmental Biology*, vol. 16, no. 4-5, pp. 554–563, 2005.

Hindawi Publishing Corporation
BioMed Research International
Volume 2014, Article ID 603173, 6 pages
http://dx.doi.org/10.1155/2014/603173

Research Article

Total Bolus Extraction Method Improves Arterial Image Quality in Dynamic CTAs Derived from Whole-Brain CTP Data

Elyas Ghariq,[1] Adriënne M. Mendrik,[2] Peter W. A. Willems,[1] Raoul M. S. Joemai,[1] Eidrees Ghariq,[3] Evert-jan Vonken,[4] Matthias J. P. van Osch,[1,3] and Marianne A. A. van Walderveen[1]

[1] *Department of Radiology, Leiden University Medical Center, Albinusdreef 2, 2333 ZA Leiden, The Netherlands*
[2] *Image Sciences Institute, University Medical Center Utrecht, Heidelberglaan 100, 3584 CX Utrecht, The Netherlands*
[3] *Department of Radiology, C.J. Gorter Center for High Field MRI, Leiden University Medical Center, Albinusdreef 2, 2333 ZA Leiden, The Netherlands*
[4] *Department of Radiology, University Medical Center Utrecht, Heidelberglaan 100, 3584 CX Utrecht, The Netherlands*

Correspondence should be addressed to Adriënne M. Mendrik; a.m.mendrik@umcutrecht.nl

Received 25 April 2014; Revised 17 June 2014; Accepted 26 June 2014; Published 16 July 2014

Academic Editor: Alessandro Cianfoni

Background and Purposes. The 320-detector row CT scanner enables visualization of whole-brain hemodynamic information (dynamic CT angiography (CTA) derived from CT perfusion scans). However, arterial image quality in dynamic CTA (dCTA) is inferior to arterial image quality in standard CTA. This study evaluates whether the arterial image quality can be improved by using a total bolus extraction (ToBE) method. *Materials and Methods*. DCTAs of 15 patients, who presented with signs of acute cerebral ischemia, were derived from 320-slice CT perfusion scans using both the standard subtraction method and the proposed ToBE method. Two neurointerventionalists blinded to the scan type scored the arterial image quality on a 5-point scale in the 4D dCTAs in consensus. Arteries were divided into four categories: (I) large extradural, (II) intradural (large, medium, and small), (III) communicating arteries, and (IV) cerebellar and ophthalmic arteries. *Results*. Quality of extradural and intradural arteries was significantly higher in the ToBE dCTAs than in the standard dCTAs (extradural $P = 0.001$, large intradural $P < 0.001$, medium intradural $P < 0.001$, and small intradural $P < 0.001$). *Conclusion*. The 4D dCTAs derived with the total bolus extraction (ToBE) method provide hemodynamic information combined with improved arterial image quality as compared to standard 4D dCTAs.

1. Introduction

Cerebral computed tomography perfusion (CTP) scans are acquired in patients with acute stroke [1] or subarachnoid hemorrhage [2]. Although there is some debate [2–5] about the prognostic value of CT perfusion, many studies [1, 2, 6–9] have shown that it provides valuable information about the cerebral hemodynamics, especially with the introduction of 320-slice CT scanners (16 cm coverage) that enable the acquisition of whole-brain CTP scans and provide an option to derive 4D dynamic CT angiography (dCTA) images from the CTP scans [9–12]. These 4D dCTA images show great potential for the assessment of collaterals [13], the measurement of cerebral circulation times [14], and arteriovenous shunting lesion assessment [15]. However, it has been shown that the 4D dCTAs have inferior quality compared to standard 3D CTA scans [16]. Therefore, cerebral arteries, and in particular arteries with a small diameter, are more difficult to assess. Several methods have been proposed to derive vascular information from CTP scans [17–19] of which some are with a quality comparable to standard 3D CTA [19, 20]. However, these methods do not provide full 4D dynamic CTA images but instead provide a 3D image showing the vasculature. Therefore, even though the arterial image quality is good, the hemodynamic information available in the 4D dCTA images is lost. In this paper, we propose a total bolus extraction (ToBE) method to derive 4D dCTAs from CTP scans in which the hemodynamic information is preserved. We performed an observer study in which two neurointerventionalists scored the image quality of the intracranial arteries in 30

anonymized and randomized dCTAs (15 standard and 15 ToBE dCTAs). The observers were blind to the type of dCTA that was presented to them. Our hypothesis is that the ToBE method will improve the arterial image quality in the 4D dCTAs derived from the 4D CTP scans compared to the standard method to derive 4D dCTAs.

2. Materials and Methods

2.1. Patients. Fifteen patients (4 males, 11 females; average age of 70.2 years, range 53–88 years) were included from a large prospective multicenter observational cohort study. This cohort study evaluates the predictive value of CTP and CTA on the clinical and radiological outcome measures of patients presenting with symptoms of acute ischemic stroke. On admission, all patients underwent an unenhanced CT and a CTP study of the brain using Toshiba Aquilion ONE 320-slice CT scanner (Toshiba Medical Systems, Otawara, Japan). Inclusion criteria were age >18 years, onset of stroke symptoms <9 hours, National Institutes of Health Stroke Scale (NIHSS) ≥2, and informed consent from patient or family. Exclusion criteria were known renal failure and contrast allergy.

2.2. CTP Scan Acquisition Protocol. CTP studies were acquired during injection of 50 mL of contrast agent (IOMERON 400, BRACCO Imaging Europe) with a flow rate of 5 mL/s followed by 40 mL saline solution with a flow rate of 4 mL/s using an antecubital placed intravenous line. A total of 24 volume scans were acquired (slice thickness: 0.5 mm, slice interval: 0.5 mm) with a total scan time of around three and a half minutes. The CTP acquisition procedure consisted of a mask volume (5 seconds after start of contrast agent administration), followed by a 10-second delay, 4 early arterial volumes (80 mA, 80 kV), 6 full dose arterial volumes (300 mA, 80 kV), and 3 late arterial volumes with an interscan delay (ISD) of 2 seconds (160 mA, 80 kV). Next, 4 venous volumes (ISD of 5 seconds) and 6 delayed volumes starting at 90 seconds (ISD of 30 seconds) were obtained (130 mA, 80 kV).

2.3. Postprocessing

2.3.1. Standard 4D Dynamic CTA. The standard 4D dCTAs were derived from the 320-slice CTPs on a postprocessing workstation (Vitrea fX, Vital Images, Minnetonka, USA). This software subtracts the first unenhanced volume of the CTP study from the subsequent contrast enhanced volumes to ensure that only vessels remain visible. From the resulting dCTA, the volume with the highest arterial contrast (arterial phase) was selected for quality analysis of the arteries.

2.3.2. ToBE 4D Dynamic CTA. ToBE dCTAs were derived from the 320-slice CTPs by employing the total bolus extraction method developed in the UMC Utrecht, The Netherlands. This method is based on a method proposed by Mendrik et al. [18, 20] that derives 3D angiograms from CTP data. These 3D angiograms (vessel enhanced volumes) were derived from the CTP data by quantifying the total change in Hounsfield units (HU) over all temporal volumes (total bolus), using the absolute area under the first temporal derivative curve as described in [18]. For this study, dynamic information extracted from the original CTP data was added to the 3D angiograms, to create the ToBE dCTAs, as follows: a Gaussian temporal filter (σ = 1 sec) was applied to the original CTP data to reduce noise. Subsequently, the time-intensity curves in the filtered CTP data were normalized to values between zero and one, by detecting the baseline and maximum, and multiplied by the 3D angiogram. An automatically generated skull mask was used to mask possible registration artifacts. From the resulting ToBE dCTA, the volume with the highest arterial contrast (arterial phase) was chosen for quality analysis of the arteries.

2.4. Quality Analysis. A total of 30 (15 standard dCTAs, 15 ToBE dCTAs) maximum intensity projections (MIPs) were created, anonymized, and randomized. Quality analysis of the arteries on these MIP-CTAs was done by two neurointerventionalists in consensus. Arteries were divided into four subcategories: (I) large extradural arteries (internal carotid arteries (ICAs) and vertebral arteries (VAs)); (II) intradural arteries: large intradural arteries (basilar artery (BA), first segments of anterior cerebral artery (A1), middle cerebral artery (M1), and posterior cerebral artery (P1)), medium sized intradural arteries (A2, P2, and P3), and small sized intradural arteries (A3, A4, M2, M3, M4, and P4); (III) communicating arteries (anterior communicating (Acom) and posterior communicating (Pcom) arteries); and (IV) cerebellar (superior cerebellar artery (SCA) and anterior inferior cerebellar artery (AICA)) and ophthalmic arteries. A 5-point analogue scoring system (5 = good quality, 1 = poor quality) was used for evaluation of image quality of the following arteries: VA, ICA, BA, SCA, AICA, ophthalmic artery, A1, Acom, A2, M1, P1, P2, Pcom, and P3. The following image quality characteristics were evaluated: arterial contrast, arterial contour sharpness, and regularity and impression of contrast to background noise ratio. Since segments of small intradural arteries (A3, A4, M3, M4, and P4) contain several peripheral branches, it is nearly impossible to provide an overall quality score for each individual vessel segment. Therefore the observers had to indicate whether 3 or more peripheral branches in each vessel segment were visible or not, with respect to the aforementioned image quality characteristics. This binary (>3 branches visible yes/no) scoring system is also used for the M2 segment of MCA, since this segment also divides into several branches directly after its division from the M1 segment; for this reason, the M2 segment is defined and scored as a small intradural artery in this study (although in terms of vessel diameter the M2 segment would be categorized in the group of medium sized intradural arteries). The cerebellar and ophthalmic arteries were scored as a separate group on the 5-point scale and no distinction between small and medium sized arteries was made. The reason for this is that the ramifications of the cerebellar and ophthalmic arteries are less well defined and balanced as compared to the small sized intradural arteries,

Table 1: Results of the observer study on arterial image quality in standard dynamic CTAs (dCTAs) and the proposed ToBE dynamic CTAs derived from 15 4D CT perfusion scans. The scores are presented as mean (standard deviation) over all 15 images and were scored on a 5-point scale (5 = good quality, 1 = poor quality) for all arteries, except the small intradural arteries. The small intradural arteries are presented as the number of scans with >3 visible small artery branches/total number of small arteries assessed (ratio in percentage; standard error).

Category	Standard dCTAs	ToBE dCTAs	Test results
Large extradural arteries	4.5 (0.7)	4.9 (0.4)	$P = \mathbf{0.001}^{*}$
Intradural arteries			
Large	4.4 (1.0)	4.7 (0.7)	$P < \mathbf{0.001}^{*}$
Medium	3.7 (1.1)	4.4 (0.8)	$P < \mathbf{0.001}^{*}$
Small	104/180 (57.8%; 3.7%)	159/180 (88.3%; 2.4%)	$P < \mathbf{0.001}^{**}$
Cerebellar and ophthalmic arteries	2.5 (1.6)	2.9 (1.7)	$P = 0.007$
Communicating arteries	2.7 (1.8)	2.9 (1.9)	$P = 0.10$

*Significant, Wilcoxon Signed Rank statistical test.
**Significant, McNemar statistical test.

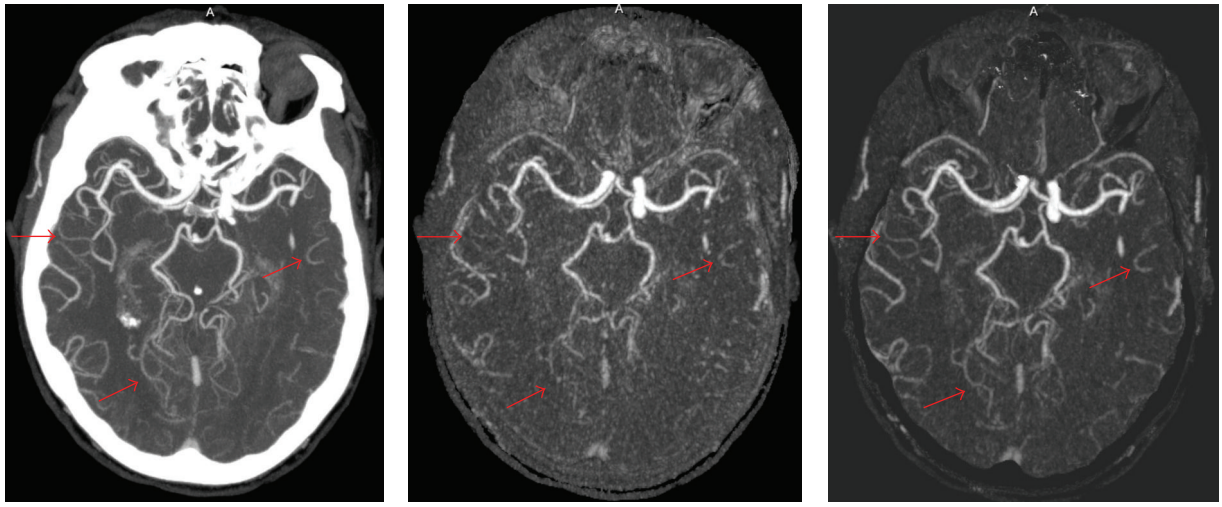

3D CTA | Arterial phase standard 4D dCTA | Arterial phase ToBE 4D dCTA

Figure 1: Illustration (maximum intensity projections over a 15 mm axial slab) of the image quality of the arteries in the dynamic 4D CTAs compared to the 3D CTA. The arrows indicate the arteries that show improved arterial image quality in the ToBE 4D dCTA compared to the standard 4D dCTA. The 3D CTA can be used as a reference.

and the arteries lack proximal divisions (e.g., the ophthalmic artery branches only when it crosses over the optic nerve). The communicating arteries were scored separately on the 5-point scale as well, because they can vary considerably in presence and size, due to, for example, aplasia, hypoplasia, or fetal continuation of the posterior cerebral artery, which complicates the classification of these arteries as medium or small.

2.5. Statistical Analysis. To compare the arterial image quality in the standard dCTAs and the ToBE dCTAs, paired nonparametric statistical tests were used. For the small intracerebral arteries, the McNemar test was used and the Wilcoxon Signed Rank test was used for the remaining arteries. The statistical analysis was performed using the SPSS 18 software package (IBM SPSS Inc., Chicago, IL, USA). A significance level of $\alpha = 0.002$ was chosen after Bonferroni correction for multiple comparisons.

3. Results

The results of the observer study are presented in Table 1. Some arteries were excluded from the statistical evaluation due to the following findings: ICA occlusion (2), BA occlusion (1), A1 occlusion (1), AICA occlusion (3), ophthalmic artery occlusion (3), and Pcom aplasia (4). The final clinical diagnoses included transient ischemic attack (4) and cerebral ischemia (7). In 4 patients, the definite diagnosis remained uncertain. The results show that the arterial image quality in the ToBE dCTAs was scored significantly higher than arterial image quality in the standard dCTAs for the large extradural and the large and medium intradural arteries. The number of visible artery branches of the small intradural arteries also improved significantly in the ToBE dCTAs compared to the standard dCTAs. Although the mean scores for the communicating arteries and cerebellar and ophthalmic arteries were slightly higher in the ToBE dCTAs compared to the standard dCTAs, this difference was not significant. Figure 1 illustrates

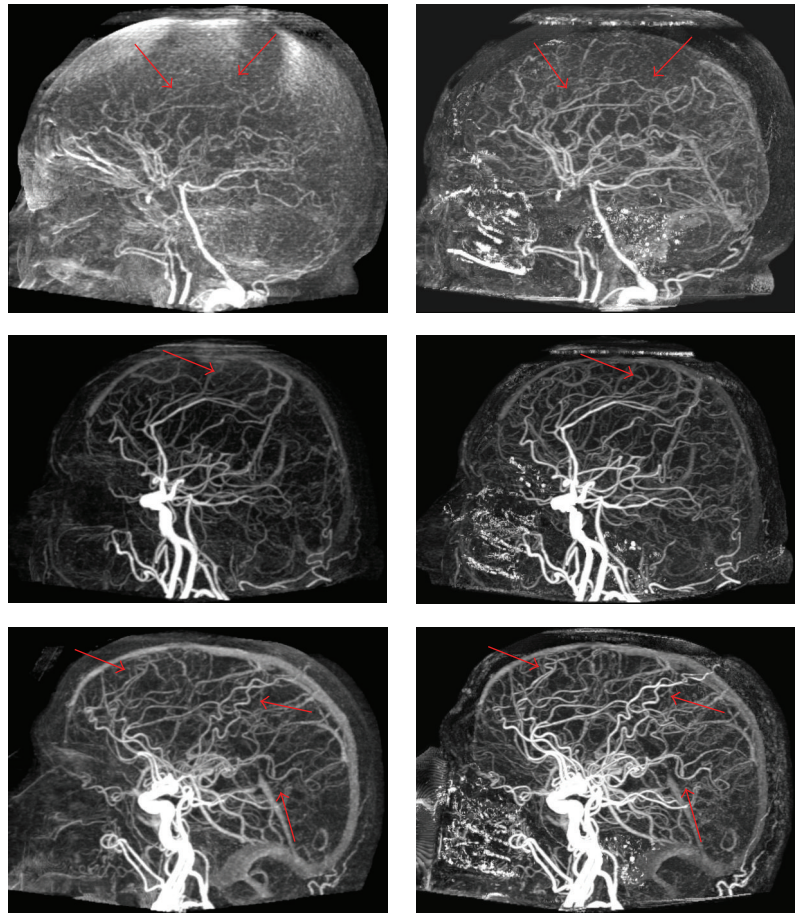

Figure 2: Illustration of the arterial phase in the dynamic CTAs derived from the CTP data. The arterial phase (whole-brain maximum intensity projection) is shown of both the standard and ToBE dCTAs of three of the evaluated 15 subjects. The arrows indicate locations where the ToBE dCTAs show improved visualization of the arteries.

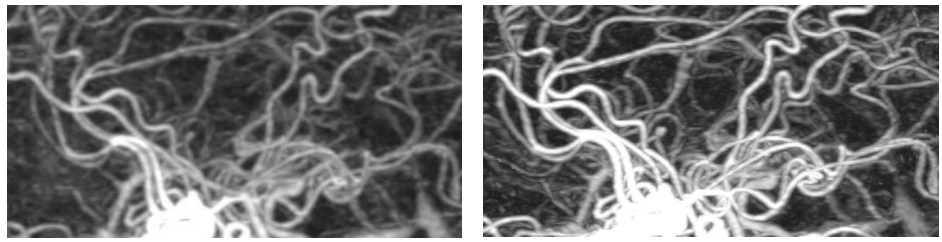

Figure 3: Zoomed in subimages of the arterial phase in one of the evaluated subjects in both the standard 4D dynamic CTA (dCTA) and the proposed ToBE 4D dCTA.

the quality of the evaluated arterial phase in the 4D dCTAs compared to the 3D CT angiography (CTA) scan.

Figure 2 shows three examples of the improved arterial image quality in the arterial phase of the ToBE dCTA as compared to the standard dCTA. Figure 3 shows a zoomed in subimage to illustrate the enhancement of the small arteries.

4. Discussion

The 320-slice CT scanner has introduced whole head coverage in a single rotation enabling acquisition of whole-brain CT perfusion (CTP) scans at a high temporal resolution. Consequently, whole-brain 4D dynamic CTAs (dCTAs) can

be derived from these CTP scans that provide information on the cerebral hemodynamics. Unfortunately, the arterial image quality of these 4D dCTAs has been shown to be inferior to 3D CTA [14]. In this paper, we proposed the total bolus extraction (ToBE) method as an alternative to the standard subtraction-based method to derive 4D dCTAs from CTP scans. The standard method subtracts the first unenhanced volume of the CTP scan from each of the subsequent volumes to derive the dCTA image, which increases noise and could decrease the arterial image quality. The ToBE method uses all volumes available in the CTP scan to retrieve the total amount of available contrast for each vessel (total bolus), after which the hemodynamic information from the CTP scan is added by showing the corresponding percentage of the total bolus at each point in time. Our hypothesis was that the ToBE method would improve the arterial image quality in 4D dCTAs compared to the standard method. Our observer study confirmed this hypothesis for the large extradural arteries and the intradural arteries. In these arteries, the image quality improved significantly. The quality of the communicating arteries and cerebellar and ophthalmic arteries showed slight improvements as well, but these were not significant. The improved arterial image quality in the ToBE dCTAs was especially prominent for the small intracranial arteries. Therefore, ToBE dCTAs could have the potential to improve detection of small-artery pathologies, for example, vasculitis, small distal aneurysms, and small shunting lesions, as compared to standard dCTAs, since Siebert et al. [16] reported that the evaluation of the medium and small intracranial arteries in standard dCTAs is limited, due to the inferior quality compared to 3D CTA.

Although the results of our study are promising, there are some limitations. First, in this study we did not compare the arterial image quality of the ToBE 4D dCTA with the arterial image quality of standard 3D CTA. We cannot therefore be certain that the ToBE 4D CTA would have the potential to replace the 3D CTA in the diagnostic work-up of ischemic stroke patients and thus may limit radiation exposure to patients. This comparison will be the subject of future studies. Second, we did not include patients with pathology of small arteries; we cannot therefore be sure that improvement of image quality of small cerebral arteries by applying the ToBE method is sufficient for detecting pathologies in these arteries. The arterial image quality improved, but further research in patients with pathologies of small arteries should assess whether the small arteries are indeed diagnostic. Third, a relatively small number of patients were used to evaluate the ToBE method. Finally, the skull mask that was used for the ToBE method introduced some artifacts in the arteries near the cranial base, that were not present in the standard dCTAs, since this method does not use skull masking. A solution to this problem would be to use the ToBE method without bone masking, since bone is automatically suppressed [18, 20]. However, in this study we used the bone mask to suppress high intensities that could result from small misalignments of the sequential CTP volumes and might reduce depiction of arteries. Improving the registration method could resolve this limitation, which is a subject for further research.

Despite these limitations, the ToBE dCTAs showed improved image quality of especially the small intracranial arteries as compared to the standard dCTAs. The clinical significance of the improved image quality of the small intracranial arteries needs to be validated in patients with small vessel pathology, for example, compared to digital subtraction angiography as a reference standard.

5. Conclusion

In conclusion, this study showed that 4D dynamic CTAs derived from 320-slice CTP scans using the total bolus extraction (ToBE) method show improved image quality of the large extradural and all intradural arteries as compared to standard 4D dynamic CTAs derived using the subtraction method. Arterial image quality improvements were especially prominent in the small intradural arteries. The 4D ToBE dynamic CTAs derived from the CTP scans combine valuable hemodynamic information with improved arterial image quality.

Abbreviations

ToBE: Total bolus extraction method
Acom: Anterior communicating artery
Pcom: Posterior communicating arteries
AICA: Anterior inferior cerebellar artery
SCA: Superior cerebellar artery
dCTA: Dynamic 4D whole-brain CT angiograms derived from CTP scans.

Conflict of Interests

The authors declare that there is no conflict of interests regarding the publication of this paper.

References

[1] G. Zhu, P. Michel, A. Aghaebrahim et al., "Computed tomography workup of patients suspected of acute ischemic stroke: perfusion computed tomography adds value compared with clinical evaluation, noncontrast computed tomography, and computed tomography angiogram in terms of predicting outcome," *Stroke*, vol. 44, no. 4, pp. 1049–1055, 2013.

[2] C. H. P. Cremers, I. C. van der Schaaf, E. Wensink et al., "CT perfusion and delayed cerebral ischemia in aneurysmal subarachnoid hemorrhage: a systematic review and meta-analysis," *Journal of Cerebral Blood Flow & Metabolism*, vol. 34, no. 2, pp. 200–207, 2013.

[3] M. Goyal, B. K. Menon, and C. P. Derdeyn, "Perfusion imaging in acute ischemic stroke: let us improve the science before changing clinical practice," *Radiology*, vol. 266, no. 1, pp. 16–21, 2013.

[4] M. Sharma and D. M. Pelz, "CT perfusion in acute stroke: added value or waste of time?" *Stroke*, vol. 44, no. 9, article e115, 2013.

[5] M. Wintermark, G. Zhu, J. T. Patrie, and P. Michel, "Response to letter regarding article, 'CT perfusion in acute stroke: added value or waste of time?'," *Stroke*, vol. 44, p. e116, 2013.

[6] A. P.-H. Huang, J.-C. Tsai, L.-T. Kuo et al., "Clinical application of perfusion computed tomography in neurosurgery," *Journal of Neurosurgery*, vol. 120, no. 2, pp. 473–488, 2014.

[7] P. Kan, K. V. Snyder, M. J. Binning, A. H. Siddiqui, L. N. Hopkins, and E. I. Levy, "Computed tomography (CT) perfusion in the treatment of acute stroke.," *World Neurosurgery*, vol. 74, no. 6, pp. 550–551, 2010.

[8] R. E. Latchaw, M. J. Alberts, M. H. Lev et al., "Recommendations for imaging of acute ischemic stroke: a scientific statement from the american heart association," *Stroke*, vol. 40, no. 11, pp. 3646–3678, 2009.

[9] K. V. Snyder, M. Mokin, and V. E. Bates, "Neurologic applications of whole-brain volumetric multidetector computed tomography," *Neurologic Clinics*, vol. 32, no. 1, pp. 237–251, 2014.

[10] R. Klingebiel, E. Siebert, S. Diekmann et al., "4-D imaging in cerebrovascular disorders by using 320-Slice CT. Feasibility and preliminary clinical experience," *Academic Radiology*, vol. 16, no. 2, pp. 123–129, 2009.

[11] W. W. Orrison Jr., K. V. Snyder, L. N. Hopkins et al., "Whole-brain dynamic CT angiography and perfusion imaging," *Clinical Radiology*, vol. 66, no. 6, pp. 566–574, 2011.

[12] E. J. Salomon, J. Barfett, P. W. A. Willems, S. Geibprasert, S. Bacigaluppi, and T. Krings, "Dynamic CT angiography and CT perfusion employing a 320-detector row CT: protocol and current clinical applications," *Clinical Neuroradiology*, vol. 19, no. 3, pp. 187–196, 2009.

[13] B. K. Menon, B. O'Brien, A. Bivard et al., "Assessment of leptomeningeal collaterals using dynamic CT angiography in patients with acute ischemic stroke," *Journal of Cerebral Blood Flow and Metabolism*, vol. 33, no. 3, pp. 365–371, 2013.

[14] E. Siebert, S. Diekmann, F. Masuhr et al., "Measurement of cerebral circulation times using dynamic whole-brain CT-angiography: feasibility and initial experience," *Neurological Sciences*, vol. 33, no. 4, pp. 741–747, 2012.

[15] P. A. Brouwer, T. Bosman, M. A. A. Van Walderveen, T. Krings, A. A. Leroux, and P. W. A. Willems, "Dynamic 320-section CT angiography in cranial arteriovenous shunting lesions," *American Journal of Neuroradiology*, vol. 31, no. 4, pp. 767–770, 2010.

[16] E. Siebert, G. Bohner, M. Dewey et al., "320-Slice CT neuroimaging: initial clinical experience and image quality evaluation," *British Journal of Radiology*, vol. 82, no. 979, pp. 561–570, 2009.

[17] H. A. F. Gratama van Andel, H. W. Venema, C. B. Majoie, G. J. Den Heeten, C. A. Grimbergen, and G. J. Streekstra, "Intracranial CT angiography obtained from a cerebral CT perfusion examination," *Medical Physics*, vol. 36, no. 4, pp. 1074–1085, 2009.

[18] A. Mendrik, E. Vonken, B. Van Ginneken et al., "Automatic segmentation of intracranial arteries and veins in four-dimensional cerebral CT perfusion scans," *Medical Physics*, vol. 37, no. 6, pp. 2956–2966, 2010.

[19] E. J. Smit, E. Vonken, I. C. van der Schaaf et al., "Timing-invariant reconstruction for deriving high-quality CT angiographic data from cerebral CT perfusion data," *Radiology*, vol. 263, no. 1, pp. 216–225, 2012.

[20] A. M. Mendrik, E. P. A. Vonken, G. A. P. De Kort et al., "Improved arterial visualization in cerebral CT perfusion-derived arteriograms compared with standard CT angiography: a visual assessment study," *The American Journal of Neuroradiology*, vol. 33, no. 11, pp. 2171–2177, 2012.